UNIVERSITY OF CALIFORNIA
SANTA CRUZ

METHYLAMMONIUM LEAD BROMIDE PEROVSKITES FOR OPTOELECTRONIC DEVICES

A dissertation submitted in partial
satisfaction of the requirements for the
degree of

DOCTOR OF PHILOSOPHY

in

ELECTRICAL AND COMPUTER
ENGINEERING

by

Emily Enlow

June 2022

The Dissertation of Emily Enlow is
approved:

_____
Professor Marco Rolandi

_____
Professor Nobuhiko Kobayashi

_____
Professor Sue Carter

_____
Peter Biehl
Vice Provost and Dean of Graduate Studies

Table of Contents

List of Figures

List of Tables

Abstract

Methylammonium Lead Bromide Perovskites for Optoelectronic Devices

by

Emily Enlow

Perovskite materials have seen increasing interest in the field of optoelectronics over the past decade. The unique crystal structure allows for facile tuning of the bandgap via stoichiometry, and the low formation energy allows for the use of low temperature and low-cost fabrication of films. Perovskites synthesized for this work will consist of both one-step polycrystalline thin films and quantum dots synthesized via a ligand assisted reprecipitation method. Films will be fabricated using spin coating techniques. The optical properties, such as the absorbance and the photoluminescence, were used to characterize the films. Surface morphology was investigated using atomic force microscopy and scanning electron microscopy. Single carrier devices and light emitting diodes were fabricated to explore the electrical properties of the perovskite films. An antisolvent wash study was performed on polycrystalline bulk thin films of methylammonium lead bromide to find the optimum antisolvent wash for surface morphology and photoluminescence. Out of 6 antisolvents investigated, n-Butanol was found to have the lowest and most consistent surface roughness, while maintaining photoluminescence. For quantum dot perovskites, a comparison between insulating organic ligands oleylamine and oleic acid (OLA-OA) and conductive organic ligands 3,3-diphenylpropylamine and trans-

cinnamic acid (DPPA-TCA) was completed. The DPPA-TCA ligands had better surface passivation, which lead to higher photoluminescence quantum yield. The surface morphology of the DPPA-TCA ligands was also improved compared to the OLA-OA ligands. DPPA-TCA ligands also had a lower turn-on voltage and increased current density in light emitting diodes. Oxide and polymer additives were incorporated into the DPPA-TCA quantum dot solutions to attempt to improve the surface morphology and consistency of the perovskite films. These additives did not offer an improvement to the film quality. Lastly, the ligand quantity of the precursor solution of the quantum dot synthesis was varied to shift the photoluminescence from green (526 nm) to blue (470 nm).

Acknowledgements

This journey has been long and hard, but also so rewarding. I am so thankful to everyone who helped me achieve these goals. First, thank you Sue for allowing me to come into your lab and work with materials that excited me so much. I don't think that I would have enjoyed my time at Santa Cruz as much without the work I was doing and your always helpful advice. To my lab mates, Eli, Roy, and Katie, thank you so much for always listening to my ideas, even when they were bad, and giving me advice and encouragement the entire time. You made working in the lab enjoyable and I will really miss working with you every day. Thank you to my parents, who never stopped asking when I would be done. Even when I was frustrated about it, I know you always had my best interests in mind and your belief in me helped me achieve all that I have done. To Enzo, you were not here when I started this journey, but you have made my life so much fuller by being in it and I am glad that you are my son. While there were challenges to having and infant and doing research, I am forever grateful that you were so easy going your entire life! Lastly, to my husband Drew, thank you so much for going along with this crazy idea. It was hard for me to come back to school, but I could not have done it without you. You have always been there to listen and help whenever I needed it and I am truly thankful for everything that you have done to get me here.

Chapter 1 Introduction

Hybrid organic-inorganic perovskites have become a material of high interest for optoelectronics due to their unique crystal structure and low formation energy. The bandgap energy of the perovskite can be changed to cover the entire visible spectrum by stoichiometric modifications while the crystal lattice is relatively tolerant to defects [1]. The low formation energy also means that these perovskite films can be deposited using techniques developed for organic semiconductors, but the perovskite films also have electrical properties which are more closely aligned to inorganic semiconductors [2,3].

Beyond the benefits of the bulk polycrystalline films that can be formed at room temperature with low-cost, facile methods, perovskite quantum dots (PeQDs) can also be formed in ambient conditions with typical lab equipment. This work uses the ligand assisted reprecipitation (LARP) method to synthesize quantum dots in a low-cost method [4]. These dots are encapsulated with organic ligands which can offer additional enhancements to the PeQD system, such as increased stability and higher photoluminescence. PeQDs also maintain the high color purity of the bulk perovskites at the reduced spacial dimension, which is advantageous over similar quantum dots made from organic or inorganic semiconductors [5].

Characterizing the perovskites is an important part of working with the perovskite materials. Since these materials are predominately used for optoelectronic devices, it is important to investigate the optical and electrical properties of the

perovskite films to work towards an improved device. Thin film devices are also highly dependent on interfaces, so characterizing the surface of the film is also an important step in improving perovskite devices.

There are many methods to produce thin film perovskite films. One method is called a one-step deposition, where the perovskite precursors are dissolved in a polar solvent, then spun to create a thin, polycrystalline film of perovskite on the surface of the desired substrate. This technique requires the use of an antisolvent wash to improve the density of the perovskite film and reduce the likelihood of pinholes. This antisolvent can affect the surface dramatically and will be investigated to find a preferred antisolvent for the creation of methylammonium lead bromine ($MAPbBr_3$).

PeQDs synthesized using different types of organic ligands are compared to explore the optical and electrical effects of the surface ligands on quantum dot films. Insulating ligands oleic acid (OA) and oleylamine (OLA) are compared to conductive ligands trans-cinnamic acid (TCA) and 3,3-diphenylpropylamine (DPPA). The role of each ligand is explored, and the resulting films are compared to examine the effect of each ligand set on the optical and electrical properties of the quantum dots.

Quantum dot solutions made using the LARP method tend to have inconsistent films and poor surface interfaces with layers in a device. This work incorporates different oxides and polymers to the quantum dot solution to improve to the film consistency and roughness while not losing electrical characteristics important for device performance.

By increasing the quantity of the ligands present in the precursor solution during the LARP synthesis of the PeQDs, the PL emission wavelength of the quantum dots can be tuned. This work will incorporate additional DPPA-TCA ligands when synthesizing $MAPbBr_3$ quantum dots to shift the PL emission from green to blue.

1.1 References

[1] R. Comin, G. Walters, E. Sol Thibau, O. Voznyy, Z.-H. Lu, E. H. Sargent, J. Mater. Chem. C (2015) https://doi.org/10.1039/C5TC01718A

[2] Z.-K. Tan, R. S. Moghaddam, M. L. Lai, P. Docampo, R. Higler, F. Deschler, M. Price, A. Sadhanala, L. M. Pazos, D. Credgington, F. Hanusch, T. Bein, H. J. Snaith, R. H. Friend, Nat. Nanotechnol. (2014) https://doi.org/10.1038/nnano.2014.149

[3] Y. Wang, Y. Zhang, P. Zhang, W. Zhang, Phys. Chem. Chem. Phys. (2015) https://doi.org/10.1039/C5CP00448A

[4] F. Zhang, H. Zhong, C. Chen, X. Wu, X. Hu, H. Huang, J. Han, B. Zou, and Y. Dong, ACS Nano. (2015) https://doi.org/**10.1021/acsnano.5b01154**

[5] Kim Y-H, Cho H, Lee T-W. Metal halide perovskite light emitters. Proc Natl Acad Sci USA 2016;113:11694–702. https://doi.org/10.1073/pnas.1607471113

Chapter 2 Perovskites

Discovered in 1839, the perovskite crystal structure has been the focus of much optoelectronic materials research in the last decade. Since 2009 when the first perovskite solar cell was reported, growth in the field has been exponential [1]. The National Renewable Energy Lab (NREL) has been tracking solar cell efficiency for decades, and

Figure 2.1 shows how perovskite solar cells have increased rapidly, reaching 25.7% in 2022 which is remarkably close to single crystalline Si solar cells peak efficiency of 26.1% [2]. The rapid increase in efficiencies over such a short period of time has encouraged the growth of the perovskite field to other types of optoelectronic devices, such as light emitting diodes (LEDs) and lasers. Perovskites have a unique crystal structure that leads to promising electrical and optical properties, but also can be deposited in low cost, low temperature methods leading to an exciting inorganic and organic semiconductor replacement.

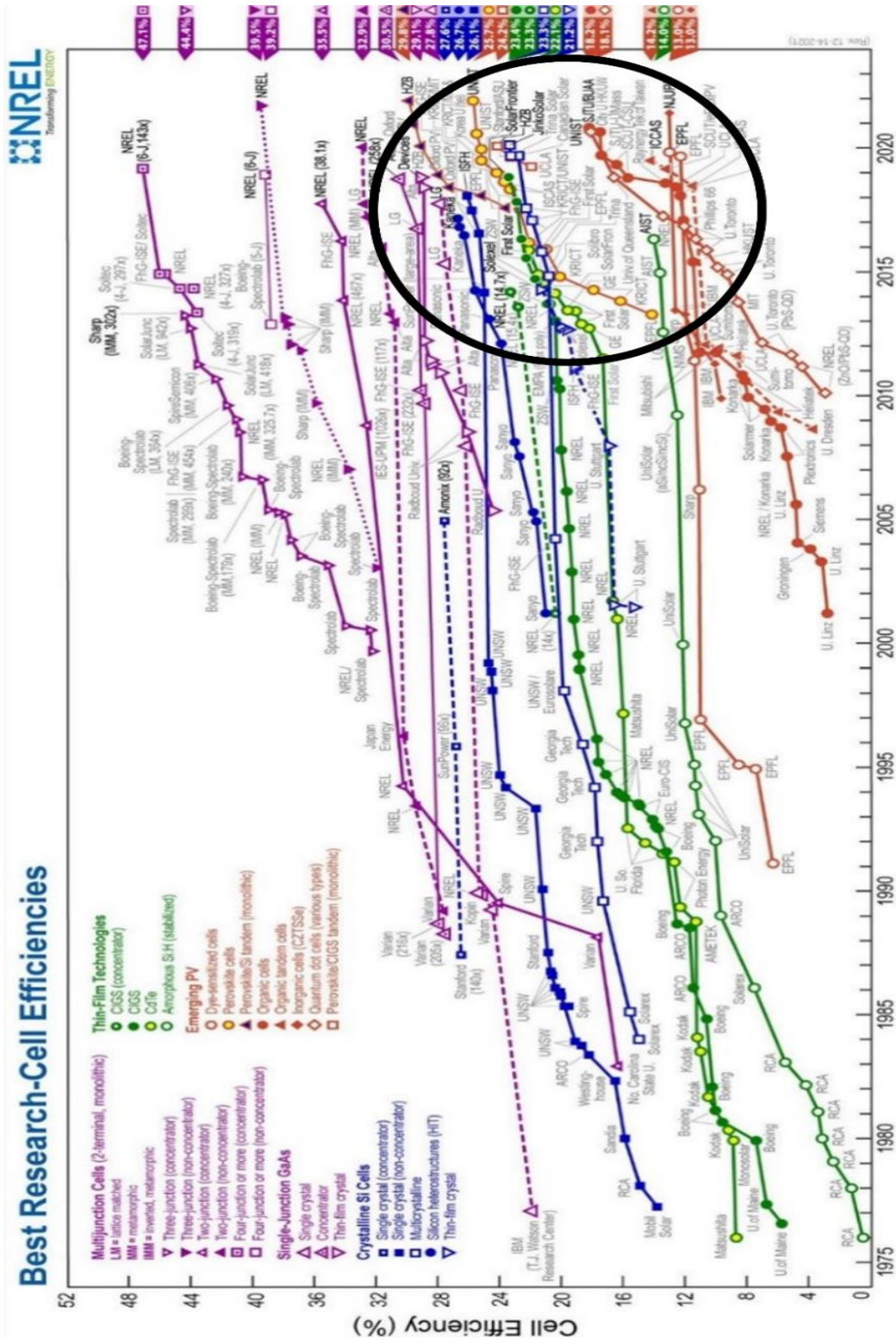

Figure 2.1: NREL solar efficiencies over the years with perovskites highlighted with the black circle [2].

2.1 Perovskite Crystal Structure

The term perovskite refers to a class of materials with a cubic, tetragonal, or orthorhombic crystal structure with the chemical formula ABX_3 shown in Figure 2.2. Figure 2.2a shows a unit cell of the perovskite crystal structure where the A ion is located at each corner of the unit cell, the B ion is located at the center, and the X ion is located on each face. When many unit cells are combined, as shown in Figure 2.2b, there is a framework of B ions surrounded by six X ions, a BX_6 block, with A ions located in the center. This is referred to as the octahedral structure of the perovskite. The size of each ion can affect the crystal parameters. If the A atom is sufficiently large, the BX_6 framework will be stretched out, possibly even broken into 2-dimensional layers rather than a 3-dimensional lattice structure. If the A atom is sufficiently small, the BX_6 framework will be compressed, and the structure will no longer be cubic [3]. These atomic structural changes can affect the macroscopic properties of the perovskite material. For this work, hybrid organic inorganic perovskites (HOIP) will be the focus. HOIPs have an organic molecule in the A ion position, a group 14 metal in the B ion position, and a halide ion in the X ion position.

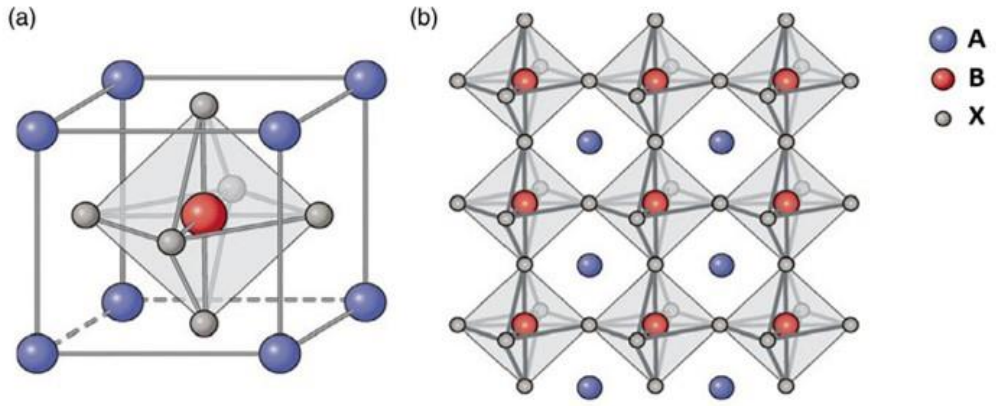

Figure 2.2: a) Unit cell of perovskite, b) octahedral structure of perovskites [3].

HOIP materials can comprise of a lot of different types of ions. To predict the crystal structure and stability a combination will have, the Goldschmidt tolerance equation can be used if the radii of the A, B, and X (r_A, r_B, r_X) ions are known:

$$t = \frac{r_A + r_B}{\sqrt{2}(r_B + r_X)} \quad (2.1$$

$$\mu = \frac{r_B}{r_X} \quad (2.2$$

Where t is the Goldschmidt tolerance and μ is the octahedral factor. Stability is defined for the Goldschmidt tolerance to be $0.81 < t < 1.11$. Cubic stability is met when $0.9 < t < 1$. When the Goldschmidt tolerance is $0.7 < t < 0.9$, the perovskite crystal structure is no longer cubic and will have a lower symmetry structure, such as tetrahedral or orthorhombic. This is usually caused by a smaller A ion, and the BX_6 framework is forced to tilt to compress the void in the center of the lattice to compensate for the smaller sized ion. The octahedral factor is considered stable for

$0.44 < \mu < 0.9$ [1,4,5]. For this work, the A ion site will be primarily methylammonium, CH_6N^+ (MA), the B ion site will be lead, Pb^{2+}; the X ion site will be bromide, Br^-. Figure 2.3 shows a plot of the A and X ion radii with respect to the Goldschmidt tolerances for Pb (red) and Sn (blue) based perovskites. From this plot the $MAPbX_3$ perovskites lie within the requirements for cubic stability.

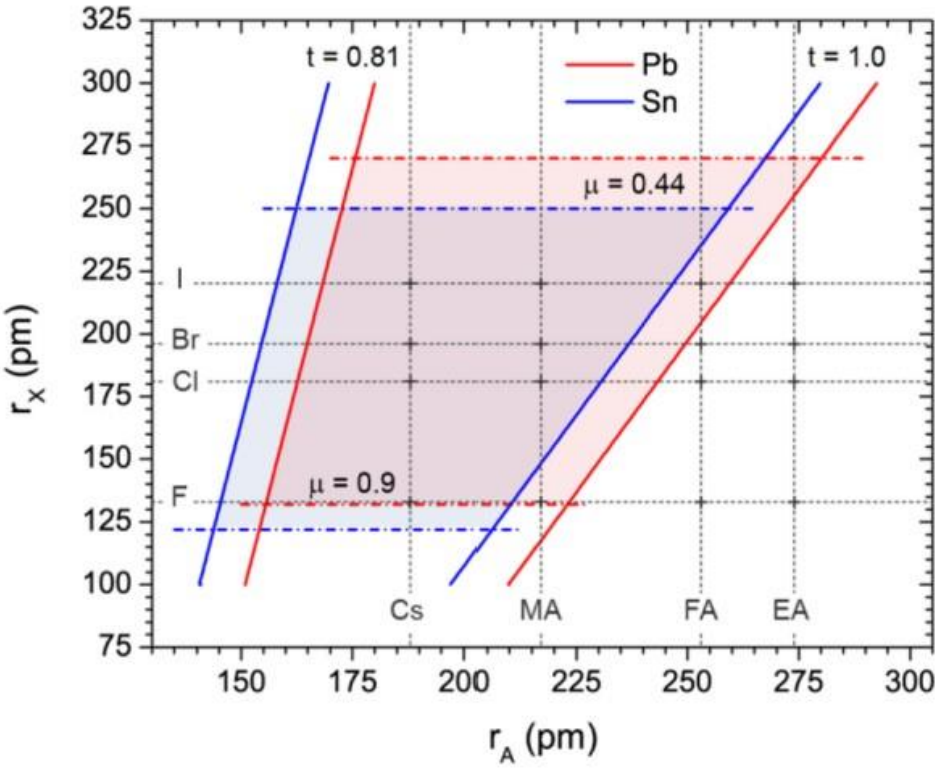

Figure 2.3: Stability chart for various perovskite compounds [1].

2.2 Material Properties

2.2.1 Band Gap

Perovskites are direct band gap semiconductor materials. The valence band maximum and the conduction band minimum occur at the same momentum space. Direct band gap semiconductors are very useful for optoelectronics because they allow for a photon emission to occur upon recombination of electrons and holes. In comparison to traditional inorganic semiconductors, like Silicon (Si) and Gallium Arsenide (GaAs), perovskites have some interesting and advantageous features of the band gap. It is important to understand how the band gap is formed in perovskites to understand these features.

The BX_6 framework dictates the electric structure of the perovskite. The A site is typically electrically inactive regarding the band structure of the material. The electronic properties of perovskite materials are directly related to the B ions, while the size of the band gap is largely dependent on the X ions. For Pb based perovskites, the Pb^{2+} ion has a stable antibonding interaction with the halide ion, this interaction forms the valence band. The orbitals involved in the valence band are the Pb 6s orbital and in the case for Bromide based perovskites, the Br 4p orbital (for I, this would be the 5p orbital and for Cl this would be the 3p orbital, thus the change in band gap size dependent on halide ion) [6].

The conduction band is primarily formed by the Pb^{2+} ion and its 6p orbital. By having the conduction band primarily comprised of a p orbital, there are a greater density of states available at the conduction band compared to GaAs, which has a

conduction band primarily comprised of delocalized s orbits. P orbitals have more positions available for electrons when compared to s orbitals. This is the reason behind the strong optical absorption of perovskites, there are more available states for electrons to occupy in the conduction band at the conduction band minimum [7,8].

As mentioned above, HOIPs also exhibit tunable band gaps by changing the halide ion. This is a large advantage over inorganic semiconductors; while inorganic semiconductors can use atomic substitutions to modify the band gap, the processing for inorganic semiconductors requires close monitoring of the lattice constant because an inorganic semiconductor is typically epitaxially grown on a semiconductor wafer, and any lattice mismatch can cause strain within the material, and that strain can cause detrimental effects to the electrical properties of the semiconductor. Perovskites are typically fabricated using low temperature techniques that do not require lattice matching to the underlying substrate. Changing any of the three ions in the perovskite will influence the band gap.

While the A ion does not directly contribute to the electronic structure of the perovskite, the size of the A ion has a direct effect on the crystal structure. A smaller A ion will decrease the band gap because the octahedral framework surrounding the A ion will compress due to a void in the center; if the A ion becomes too small the crystal structure will no longer be stable [1]. The Goldschmidt tolerance can be used to determine stability, as shown above. A larger A ion will stretch the crystal structure, thus causing an increase in band gap. It is possible for the A ion to be so large the octahedral framework breaks, and a layered perovskite forms instead. This

essentially causes quasi-quantum confinement in the material, which increases the band gap due to quantum mechanics [9,10].

The B ions directly affect the electronic structure, and the band gap will increase with increasing number on the periodic table in group 14, but the chemical stability will decrease via the same trend [11]. The X ions have the largest effect on the band gap caused by the change in orbitals from 5p for I^- ion, 4p for Br^- ion, and 3p for Cl^- ion. Band gaps for $MAPbX_3$ perovskites can range from 1.55 eV for iodide to 2.3 eV for bromide to 3.0 eV for chloride. By modifying the stoichiometry of the halide ion, the band gap (photon emission) can be changed more incrementally, as seen in Figure 2.4 [12]. Figure 2.4 demonstrates that as the perovskite halide component is changed from iodide (I) to bromide (Br) to chloride (Cl), the photon emission is shifted from IR for iodide to green for bromide to a deep blue for chloride. The halides can also be mixed to incorporate any specific wavelengths between the core iodide, bromide and chloride peaks. This is gives the perovskites a photon emission spectrum that can cover the entire visible spectrum, which is advantages for displays and light emitting diodes. This works better for I and Br mixtures and Br and Cl mixtures, rather than I and Cl mixtures due to the difference in size [13].

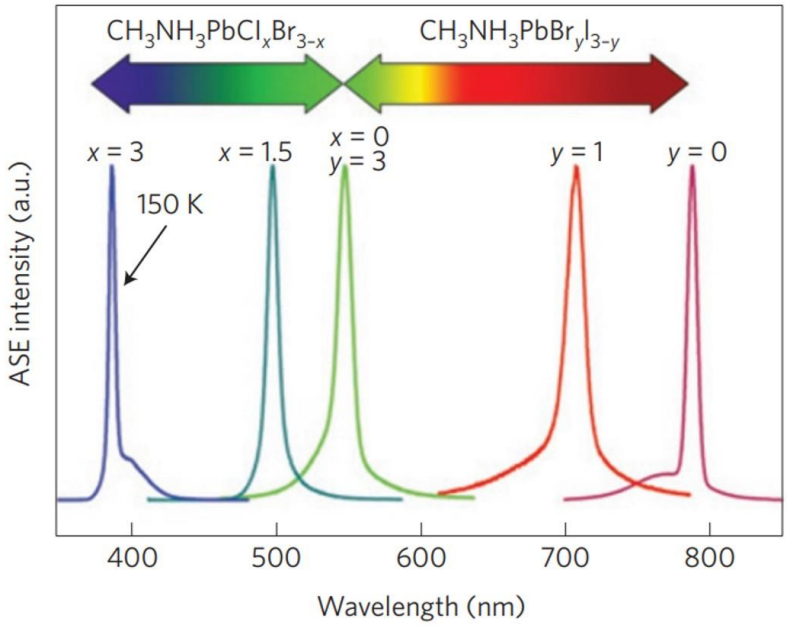

Figure 2.4: Photo emission from $MAPbX_3$ with varied ratios of I, Br, and Cl [12].

2.2.2 Recombination

As shown in Figure 2.4 above, the emission peak of the perovskite can be modified by stoichiometry. Photoluminescence (PL) is another important aspect for optoelectronics made using perovskites. Photoluminescence quantum yield (PLQY) is defined as the ratio of the number of photons emitted and the number of photons absorbed and is directly related to the radiative recombination rate divided by the total recombination rate (including both radiative and nonradiative recombination) [14]. Radiative recombination is bimolecular, and trap-assisted and Auger recombination are nonradiative. Bimolecular recombination involves both electrons and holes. Trap-assisted recombination involves a carrier getting captured by a nonradiative center, or "trap." Auger recombination occurs when an electron and hole

recombine, but the energy given off is taken by another charge carrier rather than a photon emission [15,16]. The recombination kinetics of a polycrystalline perovskites can be described using the equation:

$$-\frac{dn}{dt} = An + Bn^2 + Cn^3 \quad (2.3$$

Where n is the charge carrier density, A is the trap-assisted recombination coefficient, B is the bimolecular recombination coefficient, and C is the Auger recombination coefficient [15]. It is clear from this relationship that the recombination rate depends strongly on the charge carrier density.

Since bimolecular recombination is the primary way to emit photons, this needs to be maximized to increase the PLQY for perovskites. Perovskites generally have low exciton binding energies, which allows excitons to dissociate into free carriers easily [17,18]. Unfortunately, electron-hole recombination is a slow process, so the free carriers can be captured by traps, and partake in nonradiative recombination [1,5]. If the carrier density is low, the trap sites are all available to free carriers, which limits the number of carriers available for electron-hole recombination. At higher carrier densities, the traps will become filled and bimolecular recombination will be the dominate process [15]. To assist in enhancing the PLQY, smaller grains and thinner films can be used to spatially confine the charge carriers and speed up the bimolecular recombination rate [19].

It is also important to limit the nonradiative recombination rate by reducing the trap states. These states are usually point defects, relating to vacancies in the

halide or A ion site, Pb-halide anti-site, and metallic Pb. A common method for reducing these traps sites is to passivate the perovskite dangling bonds with ligands or other molecules. This should neutralize the charged defects in the perovskite and reduce nonradiative recombination [20,21].

Another reason HOIPs are exciting for optoelectronic devices is their narrow emission spectra, which correlates to higher purity of color. Perovskites have full-width half-maximums (FWHM) of around 20 nm and studies have shown the FWHM is independent of the perovskite dimension. When compared to organic semiconductors, which have FWHM greater than 40 nm and inorganic quantum dots which have FWHM around 30 nm but are very size dependent, perovskites have shown promise in creating the full color gamut with high purity [22]. This color purity is determined by the longitudinal optical phonons scattering and the electron-phonon coupling, not nonradiative trap-assisted recombination or impurity broadening. The crystal structure is the only aspect of the perovskite that affects the color purity, not the quality or size of the crystal [22].

2.3 Fabrication of Perovskite films

An advantage of perovskite semiconductors over traditional inorganic semiconductors is the wide variety of fabrication methods. A caveat of this is that each fabrication method influences the material properties, so the method of deposition, as well as the starting material ratios, are important factors to consider when working with perovskites. Perovskites can be fabricated using methods similar to organic semiconductors. The perovskite precursors are easily dissolved in polar

solvents and have low formation energies which means many solution process deposition methods are available for perovskite deposition and formation [23]. Common techniques include spin coating, dip coating, doctor blading, and ink-jet printing [8,24]. An advantage of these techniques is they typically can be done at room temperature with low-cost equipment. Spin coating is the primary method used in this work.

Spin coating is a useful method for creating uniform, thin films. Figure 2.5 shows the stages in the spin coating process.

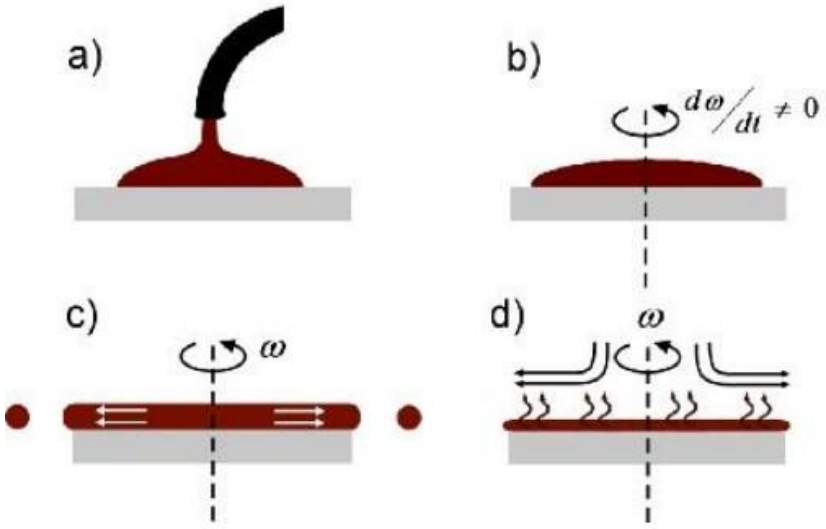

Figure 2.5: Example of the spin coating process, a) application of material, b) initial spinning ramp up, c) final spin speed reached, d) film drying [25].

Figure 2.5a shows the application of a solution to the substrate. This can either be done statically, where the solution is deposited on a stationary substrate, or

dynamically, where the solution is deposited on a slowly spinning substrate. Figure 2.5b is the initial spinning stage when the substrate is accelerating to the final spin speed. During this stage, the initial fluid thickness can cause a twisting effect where the top and bottom of the fluid are acted on at different rates as the substrate increases in speed. Eventually the shear drag and rotational acceleration become balanced. Figure 2.5c is when the substrate reaches the final spin speed and no more acceleration occurs. The centrifugal force spreads the solution evenly across the surface of the substrate. This stage is where the excess solution is spun off and a uniformly thin coating covers the substrate. The last stage, shown in Figure 2.5d, is a drying stage. The substrate is spun at a constant rate until the volatile solvent has evaporated and a dry thin film is created. The solution viscosity, concentration, and solvent will heavily influence the thickness as well as the spin speed, acceleration, and air flow during spinning [25]. The thickness of a film made via spin coating can be approximated using the equation

$$t \propto \frac{1}{\sqrt{\omega}} \qquad (2.4$$

where t is the thickness and ω is the angular velocity [25]. The films are typically spun at speeds of 1000 to 5000 rpm for 30 to 60 seconds to allow for complete drying of the film during spinning.

2.3.1 One step Perovskite Deposition

One step deposition involves dissolving the perovskite precursors, such as lead bromide ($PbBr_2$) and methylammonium bromide (MABr), in a polar solvent such

as dimethylformamide (DMF) [26–28]. The solution is then spun on a substrate in one application. The resulting film needs to be heated at 80^{o}C to assist in evaporating the solvent and forming the perovskite crystal structure. One-step films are susceptible to incomplete coverage and poor film morphology. A method to improve this is to use an antisolvent wash during spinning to pull the excess polar solvent out. This antisolvent wash works best with solvents that will not dissolve the perovskite; this reduces the solubility of the perovskite and facilitates fast crystal nucleation. When using an antisolvent wash, a mixture of polar solvents can be used to dissolve the perovskite precursors, this mixture can extend the window of time for the antisolvent drop which can help with production of the films [26–28].

2.4 Conclusion

The field of perovskites has grown over the past decade to encompass many different types of optoelectronic devices, more than just solar cells. The unique crystal structure lends itself to simple bandgap manipulation in which a perovskite material can cover the entire visible spectrum with stoichiometric changes. Since the formation energy of the perovskite crystal structure is so low, solution processing techniques, previously used for organic semiconductors, can now be used to create thin films of perovskites that over advantages over the typical organic semiconductor. Devices made from perovskites may offer low-cost solutions, while maintaining preferred electrical and optical properties in the future.

2.5 References

[1] Manser JS, Christians JA, Kamat PV. Intriguing Optoelectronic Properties of Metal Halide Perovskites. Chem Rev 2016;116:12956–3008. https://doi.org/10.1021/acs.chemrev.6b00136.

[2] Best Research-Cell Efficiency Chart | Photovoltaic Research | NREL n.d. https://www.nrel.gov/pv/cell-efficiency.html (accessed May 1, 2022).

[3] Chu Z, Chu X, Zhao Y, Ye Q, Jiang J, Zhang X, et al. Emerging Low-Dimensional Crystal Structure of Metal Halide Perovskite Optoelectronic Materials and Devices. Small Structures 2021;2:2000133. https://doi.org/10.1002/sstr.202000133.

[4] Egger DA, Rappe AM, Kronik L. Hybrid Organic–Inorganic Perovskites on the Move. Acc Chem Res 2016;49:573–81. https://doi.org/10.1021/acs.accounts.5b00540.

[5] Bhalla AS, Guo R, Roy R. The perovskite structure—a review of its role in ceramic science and technology. Materials Research Innovations 2000;4:3–26. https://doi.org/10.1007/s100190000062.

[6] Schmidt-Mende L, Dyakonov V, Olthof S, Ünlü F, Lê KMT, Mathur S, et al. Roadmap on organic–inorganic hybrid perovskite semiconductors and devices. APL Materials 2021;9:109202. https://doi.org/10.1063/5.0047616.

[7] Arul NS, Nithya VD, editors. Revolution of Perovskite: Synthesis, Properties and Applications. Singapore: Springer Singapore; 2020. https://doi.org/10.1007/978-981-15-1267-4.

[8] Kandjani SA, Mirershadi S, Nikniaz A. Inorganic–Organic Perovskite Solar Cells. IntechOpen; 2015. https://doi.org/10.5772/58970.

[9] Chen Y, Sun Y, Peng J, Tang J, Zheng K, Liang Z. 2D Ruddlesden–Popper Perovskites for Optoelectronics. Advanced Materials 2018;30:1703487. https://doi.org/10.1002/adma.201703487.

[10] Park N-G. Halide perovskite photovoltaics: History, progress, and perspectives. MRS Bull 2018;43:527–33. https://doi.org/10.1557/mrs.2018.152.

[11] Rudd PN, Huang J. Metal Ions in Halide Perovskite Materials and Devices. Trends in Chemistry 2019;1:394–409. https://doi.org/10.1016/j.trechm.2019.04.010.

[12] De Giorgi ML, Anni M. Amplified Spontaneous Emission and Lasing in Lead Halide Perovskites: State of the Art and Perspectives. Applied Sciences 2019;9:4591. https://doi.org/10.3390/app9214591.

[13] Fedeli P, Gazza F, Calestani D, Ferro P, Besagni T, Zappettini A, et al. Influence of the Synthetic Procedures on the Structural and Optical Properties of Mixed-Halide (Br, I) Perovskite Films. J Phys Chem C 2015;119:21304–13. https://doi.org/10.1021/acs.jpcc.5b03923.

[14] Stranks SD, Hoye RLZ, Di D, Friend RH, Deschler F. The Physics of Light Emission in Halide Perovskite Devices. Advanced Materials 2019;31:1803336. https://doi.org/10.1002/adma.201803336.

[15] Zhang X, Shen J-X, Van de Walle CG. First-Principles Simulation of Carrier Recombination Mechanisms in Halide Perovskites. Advanced Energy Materials 2020;10:1902830. https://doi.org/10.1002/aenm.201902830.

[16] Yang Y, Yang M, Li Z, Crisp R, Zhu K, Beard MC. Comparison of Recombination Dynamics in $CH_3NH_3PbBr_3$ and $CH_3NH_3PbI_3$ Perovskite Films: Influence of Exciton Binding Energy. J Phys Chem Lett 2015;6:4688–92. https://doi.org/10.1021/acs.jpclett.5b02290.

[17] Marongiu D, Saba M, Quochi F, Mura A, Bongiovanni G. The role of excitons in 3D and 2D lead halide perovskites. J Mater Chem C 2019;7:12006–18. https://doi.org/10.1039/C9TC04292J.

[18] Baranowski M, Plochocka P. Excitons in Metal-Halide Perovskites. Advanced Energy Materials 2020;10:1903659. https://doi.org/10.1002/aenm.201903659.

[19] Yuan Z. Defects and crystallinity control of perovskite films for light-emitting diodes. vol. 1991. Linköping: Linköping University Electronic Press; 2019. https://doi.org/10.3384/diss.diva-157713.

[20] Chen X, Cheng S, Xiao L, Sun H. Identifying, understanding and controlling defects and traps in halide perovskites for optoelectronic devices: a review. J Phys D: Appl Phys 2020;53:373001. https://doi.org/10.1088/1361-6463/ab9134.

[21] Jin H, Debroye E, Keshavarz M, Scheblykin IG, Roeffaers MBJ, Hofkens J, et al. It's a trap! On the nature of localised states and charge trapping in lead halide perovskites. Mater Horiz 2020;7:397–410. https://doi.org/10.1039/C9MH00500E.

[22] Kim Y-H, Cho H, Lee T-W. Metal halide perovskite light emitters. Proc Natl Acad Sci USA 2016;113:11694–702. https://doi.org/10.1073/pnas.1607471113.

[23] Li Z, Klein TR, Kim DH, Yang M, Berry JJ, van Hest MFAM, et al. Scalable fabrication of perovskite solar cells. Nat Rev Mater 2018;3:18017. https://doi.org/10.1038/natrevmats.2018.17.

[24] Song T-B, Chen Q, Zhou H, Jiang C, Wang H-H, (Michael) Yang Y, et al. Perovskite solar cells: film formation and properties. J Mater Chem A 2015;3:9032–50. https://doi.org/10.1039/C4TA05246C.

[25] Tyona MD. A theoritical study on spin coating technique. Advances in Materials Research 2013;2:195–208. https://doi.org/10.12989/AMR.2013.2.4.195.

[26] Jeon NJ, Noh JH, Kim YC, Yang WS, Ryu S, Seok SI. Solvent engineering for high-performance inorganic–organic hybrid perovskite solar cells. Nature Mater 2014;13:897–903. https://doi.org/10.1038/nmat4014.

[27] Ahn N, Son D-Y, Jang I-H, Kang SM, Choi M, Park N-G. Highly Reproducible Perovskite Solar Cells with Average Efficiency of 18.3% and Best Efficiency of 19.7% Fabricated via Lewis Base Adduct of Lead(II) Iodide. J Am Chem Soc 2015;137:8696–9. https://doi.org/10.1021/jacs.5b04930.

[28] Xiao M, Huang F, Huang W, Dkhissi Y, Zhu Y, Etheridge J, et al. A Fast Deposition-Crystallization Procedure for Highly Efficient Lead Iodide Perovskite Thin-Film Solar Cells. Angewandte Chemie International Edition 2014;53:9898–903. https://doi.org/10.1002/anie.201405334.

Chapter 3 Perovskite Quantum Dots

Perovskites have been shown to have very poor stability in oxygen, humidity, temperature, and UV light. These issues with stability need to be overcome before perovskites can be implemented in a large scale. One possible method for increasing stability against oxygen and moisture is to create perovskite quantum dots (PeQD) which are encapsulated in a layer of organic ligands which can act as a barrier between the perovskite and moisture. PeQDs have also show an increase photoluminescence compared to polycrystalline perovskite films due to the increase exciton binding energy and the spatial confinement of excitons. This increases the radiative recombination at lower exciton densities, which will assist in creating better perovskite-based light emitting devices.

3.1 Quantum Confinement

By limiting the dimension of the perovskite material, quantum confinement is achieved. This is due to the wave-particle duality of electrons within a material. If the dimension of the material is spatially confined to a size that is comparable to the wavelength of the electron, the electrons no longer act as free particles. This has dramatic effects on the optical and electrical properties of the material. The critical electron wavelength needed for quantum confinement is the de Broglie wavelength:

$$\lambda_{DB} = \frac{\hbar}{\sqrt{2m_e^* k_B T}} \qquad (3.1$$

where λ_{DB} is the de Broglie wavelength, $\hbar$ is Planck's constant, m_e^* is the effective electron mass, k_B is the Boltzmann constant, and T is the temperature [1]. The energy

band structure in a material of this small dimension begins to change from a band of allowable energies to discrete energies.

These new discrete energy levels can be calculated solving the Schrödinger equation and implementing boundary conditions. If a single dimension is considered, the energy levels can be calculated by:

$$E_n = \frac{n^2 h^2}{8m^* L^2} \quad (3.2$$

where E_n is the discrete energy level, n is an integer representing the quantum number, h is Planck's constant, m^* is the effective mass, and L is the dimension of the confinement [2]. This is a simplified case, but the same method can be used to calculate the 3-dimensional confinement of a quantum dot.

Quantum confinement can additionally be defined by the Bohr radii of the exciton, electron, and hole:

$$a_{B,ex} = \varepsilon_\infty \frac{m_e}{m_{ex}^*} a_o \quad (3.3$$

$$a_{B,e} = \varepsilon_\infty \frac{m_e}{m_e^*} a_o \quad (3.4$$

$$a_{B,h} = \varepsilon_\infty \frac{m_e}{m_h^*} a_o \quad (3.5$$

$$m_{ex}^* = \frac{1}{m_e^*} + \frac{1}{m_h^*} \quad (3.6$$

where $\alpha_{B,ex}$ is the exciton Bohr radius, $\alpha_{B,e}$ is the electron Bohr radius, $\alpha_{B,h}$ is the hole Bohr radius, ε_∞ is the dielectric constant at high frequency, m_e is the mass of an electron, α_o is the atomic Bohr radius, m_{ex}^* is the reduced mass of the exciton, m_e^* is the effective mass of the electron, and m_h^* is the effective mass of the hole.

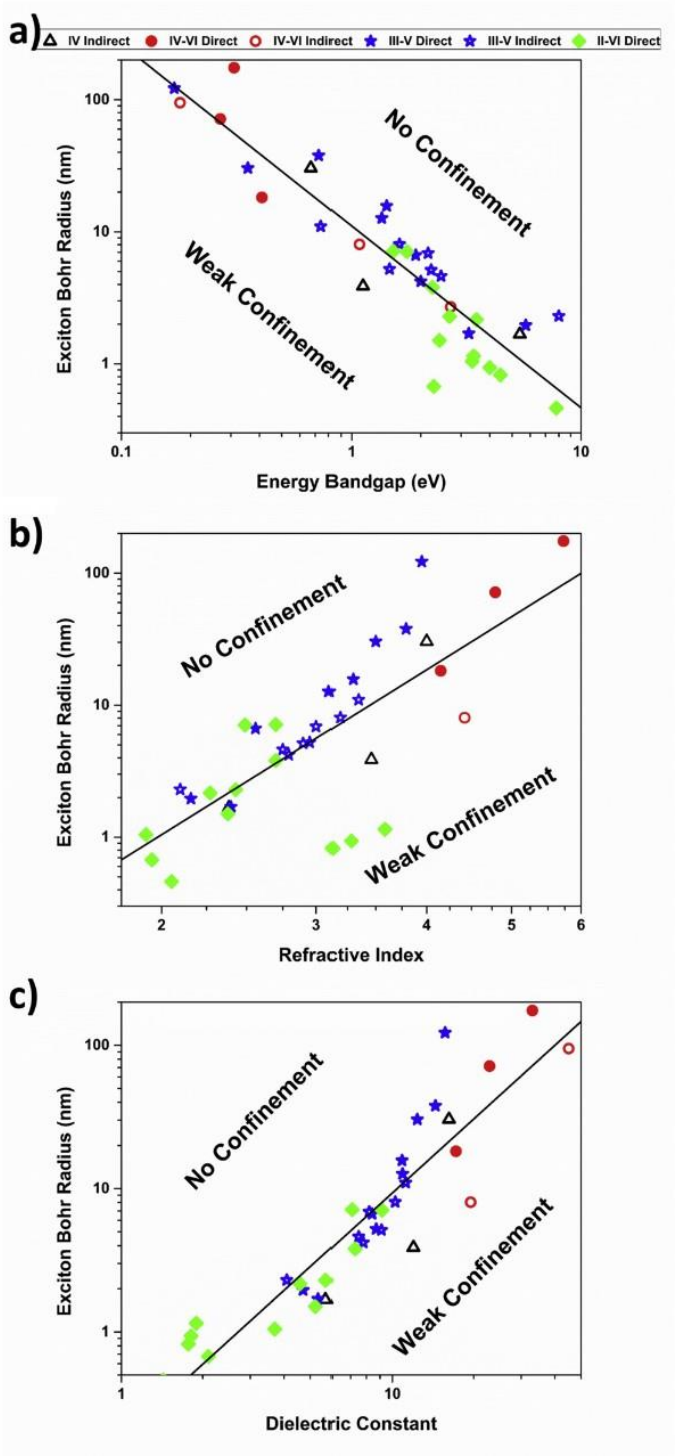

Figure 3.1: Bohr Radius as a function of a) energy bandgap, b) refractive index, c) dielectric constant. Showing the boundary of quantum confinement for a wide variety of semiconductor materials [3]

If the dimension of the material is confined to the same magnitude as the Bohr radius, quantum confinement is expected to occur. Figure 3.1 shows the quantum confinement condition based on the Bohr radius, energy bandgap, refractive index, and dielectric constant for various semiconductor materials [3].

3.2 Characteristics of Perovskite Quantum Dots

There are many interesting characteristics of quantum dots that need to be discussed to get a full picture of why these materials are so important. As stated above, the Bohr radius is a helpful measure of when quantum confinement will occur. The Bohr radius of MAPbBr3 is approximately 2 nm, which means the size of a MAPbBr3 quantum dot needs to be on the order of 4 nm to see quantum confinement occur [4]. With this small sized quantum dot, the surface to volume ratio is very high. This has an interesting effect in perovskite materials, which in general tend to have many bulk defects present. When the volume of the quantum dot is reduced, this can reduce the number of defects in the dot. While this may seem like a positive change, the defects then become localized to the surface, and cause an increase in surface energy[5,6]. These surface traps, if not passivated, will cause non-radiative recombination. It is a crucial step to passivate the surface of the quantum dot. This can be done in a wide variety of ways. This work will focus on organic ligand passivation.

The reduced dimension also increases the exciton binding energy, which means excitons are less likely to dissociate into free electrons and holes. This increased binding energy in combination with the reduction of defects in the

perovskite crystal structure can lead to an increase in photoluminescence quantum yield (PLQY) [7]. Another improvement of PeQDs over traditional semiconductor QDs is the bandgap tunability over the entire visible spectrum. As outlined in the previous chapter, perovskites have a tunable bandgap based on their stoichiometry. In combination with quantum confinement, a much finer tuning of the bandgap is possible [8].

Along with the tunable bandgap, the FWHM of the emission peak is still on the order of 20 nm, comparable to the bulk perovskite. This small FWHM is not common for most quantum dot materials where traditional quantum dot semiconductors will have a FWHM around 30 nm and organic quantum dot semiconductors will have a FWHM around 50 nm [9]. Figure 3.2 shows the FWHM as a function of the dimension of the material for different materials.

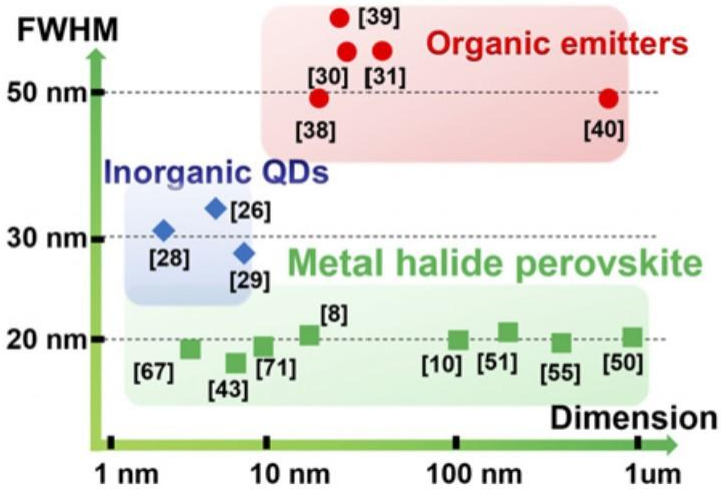

Figure 3.2: FWHM of inorganic quantum dots, organic semiconductors, and perovskites by dimension.[9]

Perovskites are prone to stability issues, especially when exposed to oxygen, moisture, and UV light. PeQDs can offer a greater amount of stability when compared to bulk perovskites. This is caused by the encapsulation of the quantum dot in different ligands. If the quantum dot is encapsulated by a hydrophobic ligand, enhance stability has been seen in the PeQD [10].

3.3 Ligand Assisted Reprecipitation Method

Synthesis via reprecipitation is a versatile and simple way to prepare colloidal nanoparticle solutions of many different types including perovskites. Zhang et al. introduced this method in 2015 by using MAPbBr3, oleic acid, and n-octylamine [11]. This method has three primary components: precursors, organic ligands, and solvents. The precursors are the material that will make up the quantum dot, in this case the precursors will form a perovskite. The organic ligands will form a monolayer on the outside of the quantum dot, and the size of the quantum dot is dependent on the ligands. The solvents will be used to create colloidal solutions as well as facilitate the creation of different saturations during the process.

Ligand assisted reprecipitation (LARP) works by introducing a precursor solution, containing perovskite precursors MX_2, AX, and organic ligands, in a polar solvent into a vigorously stirring nonpolar solvent. There are two primary stages for the PQD fabrication: nucleation and growth [12]. The kinetics behind the nucleation and growth stages is so fast that it is difficult to separate the two stages. This means that the quality of the crystal structure of the perovskite is predominantly influenced by the initial nucleation seed. When the precursor solution is introduced into the

nonpolar solvent, the precursor solution becomes supersaturated in the solvents and nucleation is induced [13].

3.4 Ligand Selection

Ligand selection is very important for quantum dots. Ligands can be classified in to three main types: X-type, L-type, and Z-type. X-type ligands will act as one electron donors, L-type ligands will act as two electron donors, and Z-type will act as two electron acceptors. Due to the ionic nature of PeQDs, X-type and L-type ligands and the most common types of ligands used with perovskites. X-type ligands with either donate one electron to the halide anion or to the Pb2+ and A cations; common x-type ligands are alkylammonium salts and alkylcarboxylic acids. L-type ligands will bond with the Pb2+ cation and are commonly alkylamines. Z-type ligands accept electrons from the halide anion; these ligand types are typically K+ or Na+ ions. Figure 3.3 shows the different bonding characteristics and types of ligands common for quantum dots [13].

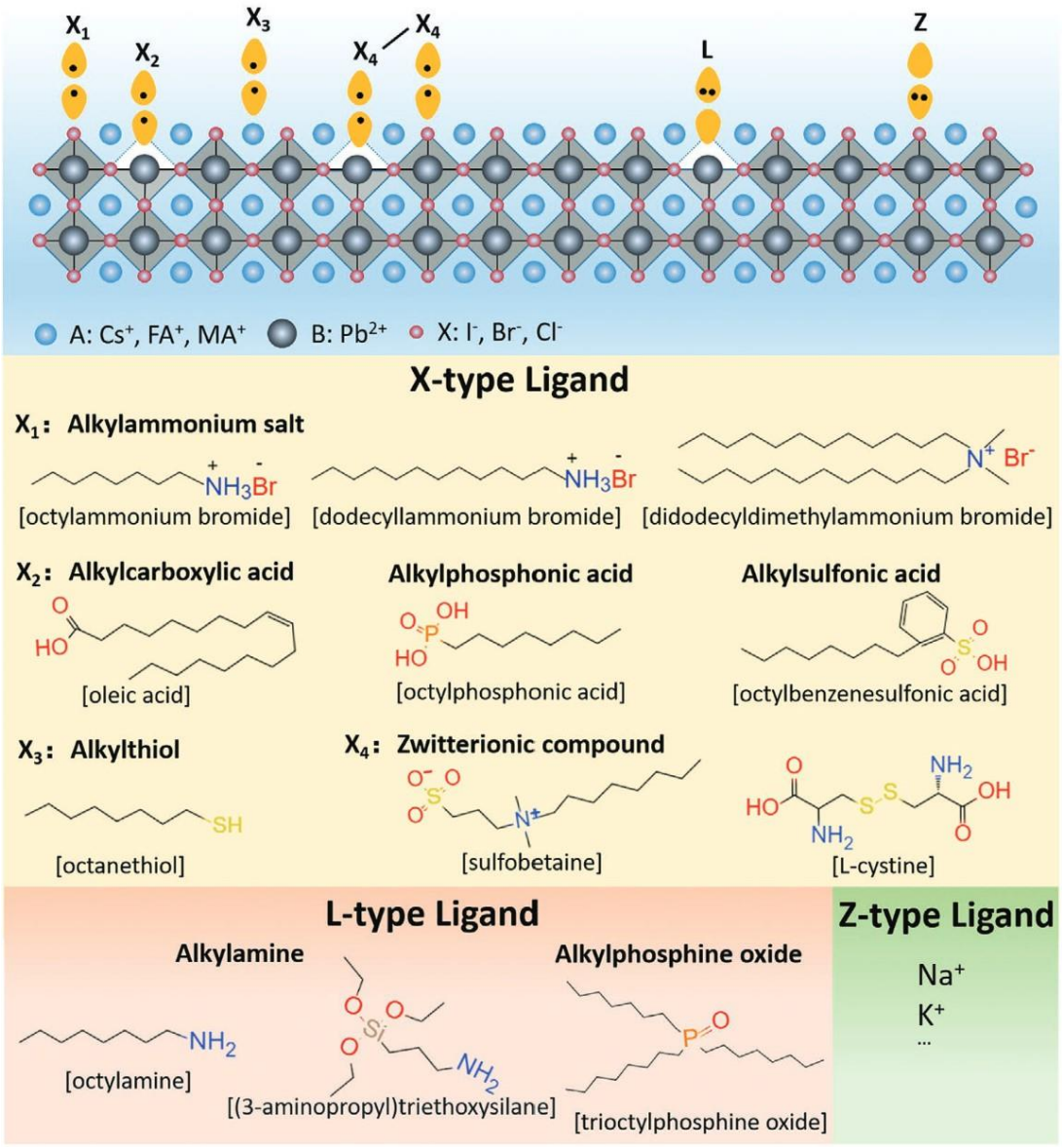

Figure 3.3: Ligand classifications and the bonding with perovskites. [13]

In addition to different bonding classifications, ligands can also be defined by carbon chain length, bulkiness, and functional groups[13]. Carbon chain length has a direct relationship to the size and shape of the PeQD. By modifying the length of the

carbon chain, $CsPbX_3$ nanocrystals have been shown to form shapes when different lengths of ligands are attached to the surface of the ligand [14, 15]. Many studies have been completed on long chain hydrocarbon ligands, such as oleylamine (OLA), oleic acid (OA), and n-octylamine, for PeQDs[11,12,14,16,17]. There are a few issues with these long chain hydrocarbon ligands for use in optoelectronic devices. The long chain hydrocarbon ligands tend to be insulating in nature, so charge transfer between the quantum dot and the ligand can be limited by the ligand. Also, since these ligands tend to consist of 10 or more carbons in a single chain, there is a large distance between quantum dots, which reduces the dot-to-dot transfer as well and is undesirable for a thin film device. Bulkiness is defined by the number of branches on the ligand, more branches correspond to a bulkier ligand. Bulkier ligands have been shown to improve the colloid stability of the PeQDs due to the branches limiting proton exchange of the ligand and thus limiting desorption of the ligand from the quantum dot surface. If a ligand had too many branches it may not be suitable for the surface of the quantum dot[13].

By incorporating different functional groups on the ligand, the properties of the ligand and the PeQD can be dramatically altered. When a conjugated alkylamine, 3-phenyl-2-propen-1-amine (PPA) molecule with an aromatic ring and a C=C functional group is used as a ligand for PeQDs, the colloidal stability and high PLQY are maintained while the conductivity and charge-carrier mobility was increased by 22 times when compared to OA/OLA ligands. This increase in conductivity and

charge-carrier mobility was caused by the delocalization of the conjugated molecular orbitals and the pi-pi stacking of the aromatic rings [18].

3.5 Conclusions

By restricting the size of the perovskite crystal, quantum confinement can occur. Perovskite quantum dots can be synthesized using the ligand assisted reprecipitation method which can be done in ambient conditions and at room temperatures, without expensive equipment. This method has many variables, and these different variables can be used to fine tune the quantum dot features. A major player in quantum dots synthesized in this way are the ligands. These molecules encapsulate the quantum dot and can affect the properties of the resultant film. Much of this work is focused on using conductive ligands to create electrical devices and experimenting with modification of the bandgap using ligand concentration.

3.6 References

[1] Mohammad NS. Understanding quantum confinement in nanowires: basics, applications and possible laws. J Phys: Condens Matter 2014;26:423202. https://doi.org/10.1088/0953-8984/26/42/423202.

[2] Nozik A. Fundamentals and applications of quantum-confined structures 2007. https://doi.org/10.1142/9781848161542_0003.

[3] Quantum confinement: Size on the grill! | Elsevier Enhanced Reader n.d. https://doi.org/10.1016/j.jpcs.2019.109320.

[4] Droseros N, Longo G, Brauer JC, Sessolo M, Bolink HJ, Banerji N. Origin of the Enhanced Photoluminescence Quantum Yield in $MAPbBr_3$ Perovskite with

Reduced Crystal Size. ACS Energy Lett 2018;3:1458–66. https://doi.org/10.1021/acsenergylett.8b00475.

[5] Zhang F, Zhong H, Chen C, Wu X, Hu X, Huang H, et al. Brightly Luminescent and Color-Tunable Colloidal CH3NH3PbX3 (X = Br, I, Cl) Quantum Dots: Potential Alternatives for Display Technology. ACS Nano 2015;9:4533–42. https://doi.org/10.1021/acsnano.5b01154.

[6] A comprehensive review of doping in perovskite nanocrystals/quantum dots: evolution of structure, electronics, optics, and light-emitting diodes | Elsevier Enhanced Reader n.d. https://doi.org/10.1016/j.mtnano.2019.100036.

[7] Polavarapu L, Nickel B, Feldmann J, Urban AS. Advances in Quantum-Confined Perovskite Nanocrystals for Optoelectronics. Advanced Energy Materials 2017;7:1700267. https://doi.org/10.1002/aenm.201700267.

[8] Huang H, Bodnarchuk MI, Kershaw SV, Kovalenko MV, Rogach AL. Lead Halide Perovskite Nanocrystals in the Research Spotlight: Stability and Defect Tolerance. ACS Energy Lett 2017;2:2071–83. https://doi.org/10.1021/acsenergylett.7b00547.

[9] Kim Y-H, Cho H, Lee T-W. Metal halide perovskite light emitters. Proc Natl Acad Sci USA 2016;113:11694–702. https://doi.org/10.1073/pnas.1607471113.

[10] Vickers ET, Graham TA, Chowdhury AH, Bahrami B, Dreskin BW, Lindley S, et al. Improving Charge Carrier Delocalization in Perovskite Quantum Dots by Surface Passivation with Conductive Aromatic Ligands. ACS Energy Lett 2018;3:2931–9. https://doi.org/10.1021/acsenergylett.8b01754.

[10] Bhalla AS, Guo R, Roy R. The perovskite structure—a review of its role in ceramic science and technology. Materials Research Innovations 2000;4:3–26. https://doi.org/10.1007/s100190000062

[12] Costa WC, Salla CAM, Ely F, Bechtold IH. Highly emissive MAPbBr $_3$ perovskite QDs by ligand-assisted reprecipitation: the antisolvent effect. Nanotechnology 2022;33:095702. https://doi.org/10.1088/1361-6528/ac3bf1.

[13] Bai Y, Hao M, Ding S, Chen P, Wang L. Surface Chemistry Engineering of Perovskite Quantum Dots: Strategies, Applications, and Perspectives. Advanced Materials 2022;34:2105958. https://doi.org/10.1002/adma.202105958.

[14] Sun S, Yuan D, Xu Y, Wang A, Deng Z. Ligand-Mediated Synthesis of Shape-Controlled Cesium Lead Halide Perovskite Nanocrystals *via* Reprecipitation Process at Room Temperature. ACS Nano 2016;10:3648–57. https://doi.org/10.1021/acsnano.5b08193.

[15] Zhu F, Men L, Guo Y, Zhu Q, Bhattacharjee U, Goodwin PM, et al. Shape Evolution and Single Particle Luminescence of Organometal Halide Perovskite Nanocrystals. ACS Nano 2015;9:2948–59. https://doi.org/10.1021/nn507020s.

[16] Levchuk I, Osvet A, Tang X, Brandl M, Perea JD, Hoegl F, et al. Brightly Luminescent and Color-Tunable Formamidinium Lead Halide Perovskite FAPbX $_3$ (X = Cl, Br, I) Colloidal Nanocrystals. Nano Lett 2017;17:2765–70. https://doi.org/10.1021/acs.nanolett.6b04781.

[17] Zhang F, Zhong H, Chen C, Wu X, Hu X, Huang H, et al. Brightly Luminescent and Color-Tunable Colloidal CH $_3$ NH $_3$ PbX $_3$ (X = Br, I, Cl) Quantum Dots: Potential Alternatives for Display Technology. ACS Nano 2015;9:4533–42. https://doi.org/10.1021/acsnano.5b01154.

[18] Dai J, Xi J, Li L, Zhao J, Shi Y, Zhang W, et al. Charge Transport between Coupling Colloidal Perovskite Quantum Dots Assisted by Functional Conjugated Ligands. Angewandte Chemie International Edition 2018;57:5754–8. https://doi.org/10.1002/anie.201801780.

Chapter 4 Characterizations Methods

An important topic for materials research is methods of characterizing the samples. For this work there are three main types of characterization: optical, surface, and electrical. Using these different methods, the properties of the perovskite films and devices can be explored.

4.1 Optical Testing

Optical testing of neat films is a very useful technique because it allows the material to be measured in a non-destructive way, while still giving information relevant to optoelectronics. Absorbance is the quantity of light a material of a given thickness absorbs at a specific wavelength. This can be found by measuring the transmittance of light through the material and then using the following equation to calculate absorbance:

$$A = 2 - \log_{10}(\%T) \qquad (4.1$$

where %T is the measured percent transmittance. This method does not consider the reflectance of the material, but these materials typically have a low reflectance, so omitting this information should not affect the measurement dramatically, but it is a consideration for possible error introduced into the measurement and calculation. The percent transmittance is measured using a spectrophotometer, in the work a Jasco V-670 was used. A baseline measurement is taken to get the total incident light at each wavelength, and then the sample is placed in the beam line and the transmitted light through the sample is measured at each wavelength. The ratio of transmitted light to total incident light multiplied by 100 is the percent transmittance used in Equation

Error! Reference source not found.. An example of a typical absorbance plot for MAPbBr3 is shown in Figure 4.1. Scattering can occur on during this measurement which can offset the absorbance as shown at the lower energies in Figure 4.1. The exciton peak shown in the figure may not be present at room temperature due to excitonic broadening at higher temperatures. This exciton peak can be used to describe the exciton binding energy of the material. The band-to-band region helps define the bandgap of the material [1].

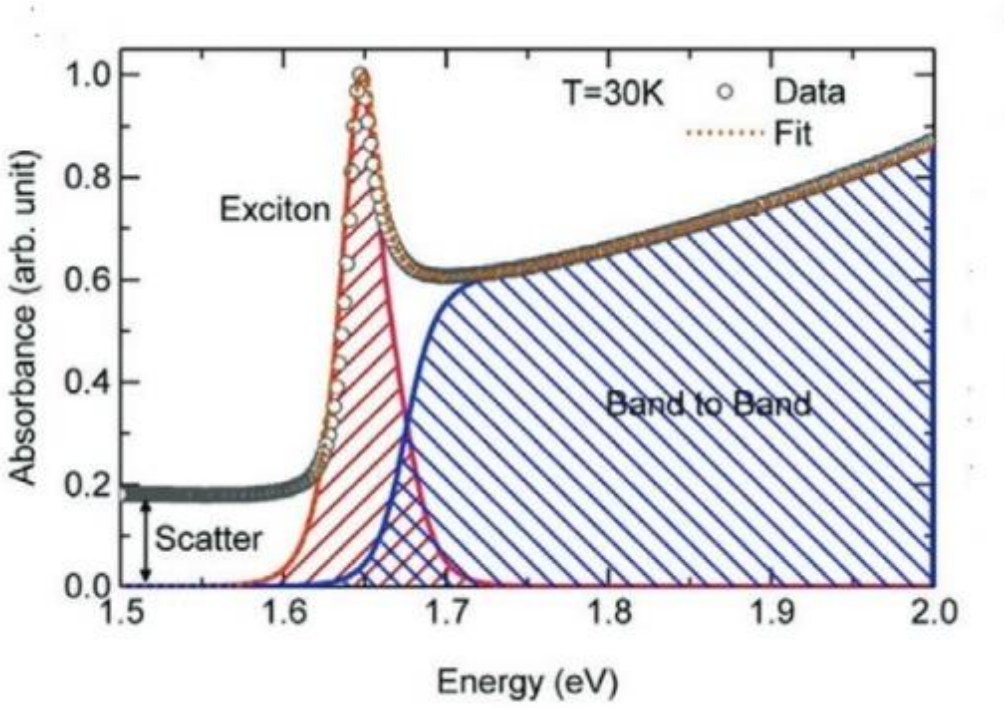

Figure 4.1: Typical absorbance plot with scattering, exciton peak, and band to band region. [1]

The absorbance is directly related to the bandgap energy of the material, and thus from this measurement, the bandgap of the material can be found by using a Tauc fit. To use a Tauc fit, $(Ah\nu)^{1/\gamma}$ is plotted on the y-axis; where A is the absorbance, h is Planck constant, ν is the photon frequency, and γ is dependent on the bandgap transition, either ½ for direct or 2 for indirect [2]. The x-axis is the photon energy, hν. An example of this plot is shown in Figure 4.2.

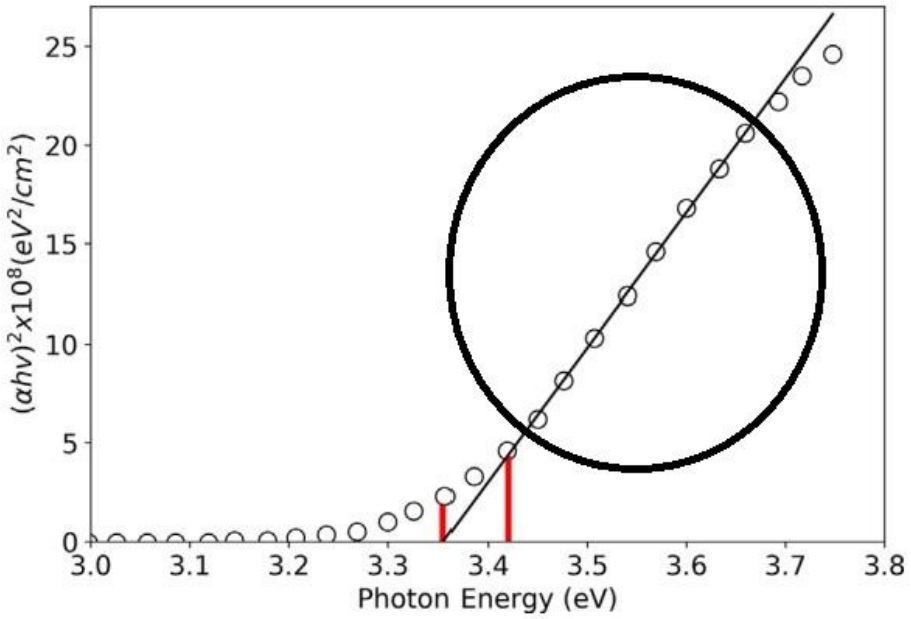

Figure 4.2: Tauc fit to find band gap energy. [2]

The fit of the region circled will result in the bandgap energy of the material by extrapolating the line to the x-axis, or by finding the x-intercept of the linear fit to the region. Since the absorbance measurements do not take the reflectance into consideration, this measurement is susceptible to error caused by scattering or

reflectance of the sample but can be used to get a generally close value to the bandgap energy. Another issue that is occurs with Tauc plots and bandgap energy calculations is seen in the case of quantum dots. Since the quantum dots produced in this work have a spread of sizes, the bandgap energies tend to also have a spread of values. This leads to a smearing of the absorbance and can make calculating the bandgap energy challenging.

Photoluminescence (PL) is an important feature of the perovskite film for optoelectronic devices. To measure PL, a beam of light with energy larger than the bandgap energy is shined on the sample. The sample absorbs this high energy light, and that absorption causes an electron to be excited into the conduction band. If this electron in the conduction band recombines with a hole in the valence band, a photon with energy equal to the bandgap energy will be released. This released photon is measured and is the PL response of the material. There typically a spreading of the PL response rather than a discrete energy emission at the bandgap energy, and this is caused by different energy defects and traps within the material that can cause a spread of photon energies. A measurement of the color purity of the PL emission peak is the full width half maximum (FWHM) of the peak. A smaller FWHM relates to a purer color and is generally more desirable for light emitting devices.

Figure 4.3 shows an example of absorbance and PL spectra for the same material on a single plot. On this plot the PL exhibits a red shift compared to the absorbance spectra. This phenomenon is called the Stokes shift. This shift is typically described in terms of energy in eV but can also be expressed in terms of wavelength.

A reduction in the Stokes shift is often seen with reducing dimension. A smaller Stokes shift means that the PL is caused by exciton recombination rather than free carrier recombination [3].

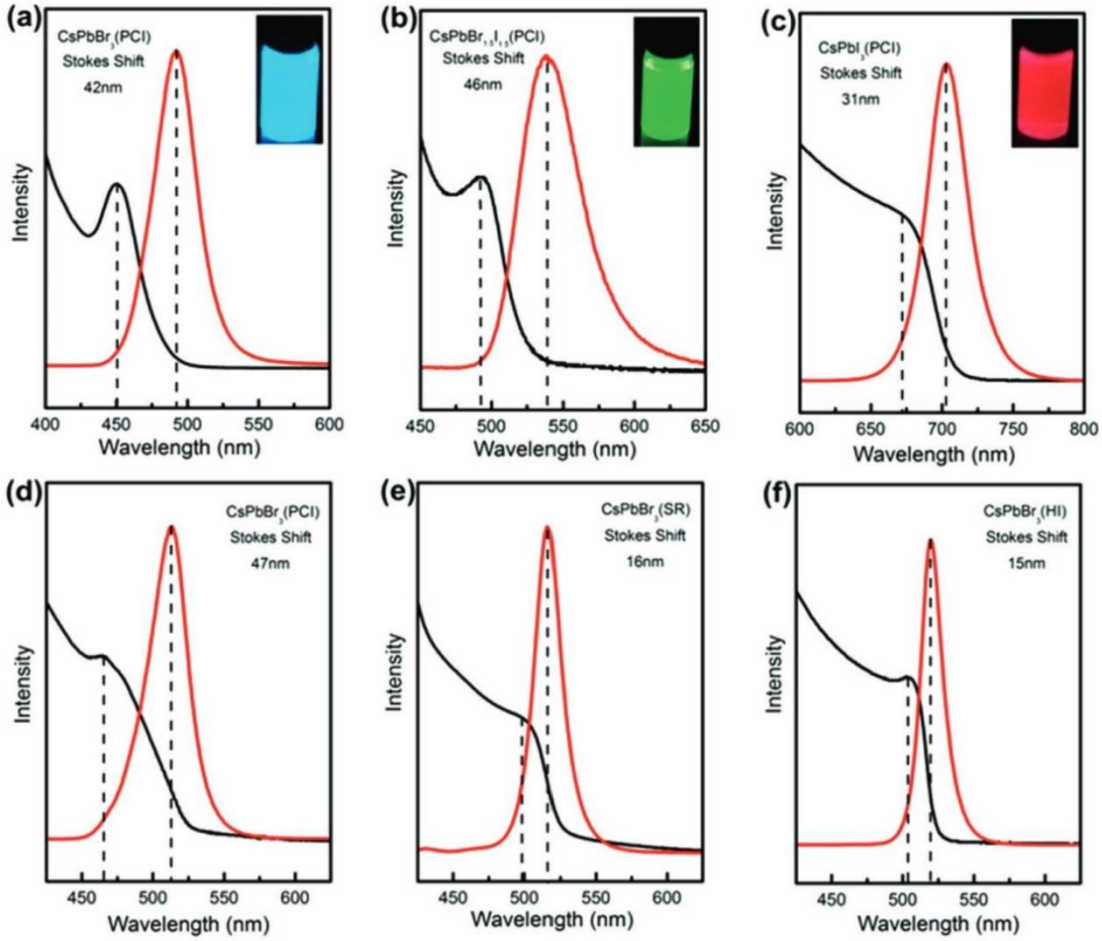

Figure 4.3: Stokes shift of different perovskite materials. [4]

Photothermal deflection spectroscopy is a measurement technique that can be used to find the bandgap, Urbach energy, and weak absorption tail of the material. Light is incident on the material, and the absorption of light causes carriers to excite. When the carriers relax, the surrounding environment is heated causing a change in the index of refraction. A probe beam which is parallel to the sample is deflected

because of the change in the index of refraction. The absorption coefficient can be calculated from the fluctuation in the laser. The absorption coefficient is calculated using the following equation

$$\alpha(\lambda) = -\frac{1}{d}\ln\left(1 - \frac{V_{sig}(\lambda)}{V_{ref}(\lambda)}C_{norm}\right) \quad (4.2$$

where d is sample thickness, V_{sig} is the voltage signal from the probe deflection, V_{ref} is the voltage signal from the reference detector, and C_{norm} is the scaling constant determined by the transmission of the sample taken from UV-Vis transmission, $V_{sig,}$ V_{ref} at a specific wavelength. The bandgap energy can then be calculated using a Tauc plot mentioned above. This method is less susceptible to reflectance and scattering errors since the measurement is caused by changes in the refractive index rather than the transmittance of the sample, and thus gives a more accurate measurement of the bandgap energy. The Urbach energy, E_U, is a valuable tool in measuring the level of disorder in a film and is found using $h\nu \sim E_U \ln(\alpha)$[5].

4.2 Film Characterization

Film quality plays a large role in device fabrication and efficiency. Perovskites are a crystalline material, and it is important to verify this structure via x-ray diffraction (XRD). Surface interfaces can introduce trap states and reduce the electrical conduction through the device or result in non-radiative recombination of generated electron-hole pairs. The thickness of each layer also needs to be optimized for improved efficiency. Characterizing and understanding the surface and thickness

of the film layers can be completed using atomic force microscopy (AFM) and scanning electron microscopy (SEM).

XRD is a technique to analyze the crystallography of a sample. This can be used to confirm the sample materials and the crystal structure. To perform XRD, a beam of x-rays is incident on a material. These x-rays will interact with the atoms of the material and depending on the spacing of the atoms resulting in diffracted x-rays. The spacing of the atoms will cause the constructive or deconstructive interference of the diffractive x-rays, and this is the premise behind XRD. The requirements for constructive interference are defined by Bragg's Law:

$$\lambda = 2dsin(\theta) \qquad (4.3$$

where λ is the wavelength of the incident x-ray, d is the separation between planes of atoms, and θ is the incident angle of the beam. When Bragg's Law is satisfied, constructive interference will occur, and a peak will be seen that can be related to the plane of the crystal structure. By comparing the peaks of a material to a known standard, the crystal structure can be confirmed [6].

AFM is a technique where a cantilever with a fine pointed tip is tapped along the surface of the sample. The tip interacts with the atomic forces of the film and the cantilever is deflected up or down based on the surface morphology. SEM uses an electron beam scanned along the sample area. The electron beam is comprised of high energy electrons that when incident on the sample will cause secondary electrons to be ejected from the top layer of the material. This technique is useful for

topographical data on conductive samples and is useful for accurate thickness measurements.

4.3 Device Testing

By integrating the perovskite films into device structures, the electrical properties can be evaluated. Light emitting diodes (LED) use both electrons and holes injected into the active layer. Upon radiative recombination, a photon is emitted. The typical device structure is shown in Figure 4.4.

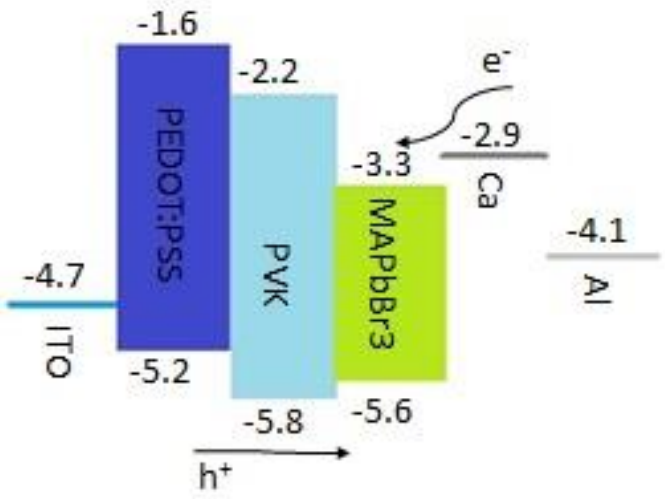

Figure 4.4: Energy band structure of LED.

The typical structure consists of a low work function metal as an anode, a hole injection layer (HIL), active layer, electron injection layer (EIL), and a high work function metal as a cathode. The HIL has a valence band edge that is aligned with the valence band edge of the active layer to facilitate injection of holes into the active

material. In some cases, these HIL layers can also act as an electron blocking layer if the conduction band edge is sufficiently high compared to the conduction band edge for the active layer. The EIL performs the same function, but electrons are injected via the conduction band edge alignment. Additional hole and electron transport layers (HTL, ETL) can also be used to help with charge transport. Blocking layers can also be introduced to limit the carrier transport from one electrode to the other electrode. There is a wide variety of materials that can be used for these layers. Figure 4.5 shows some of the possibilities for perovskite LEDs.

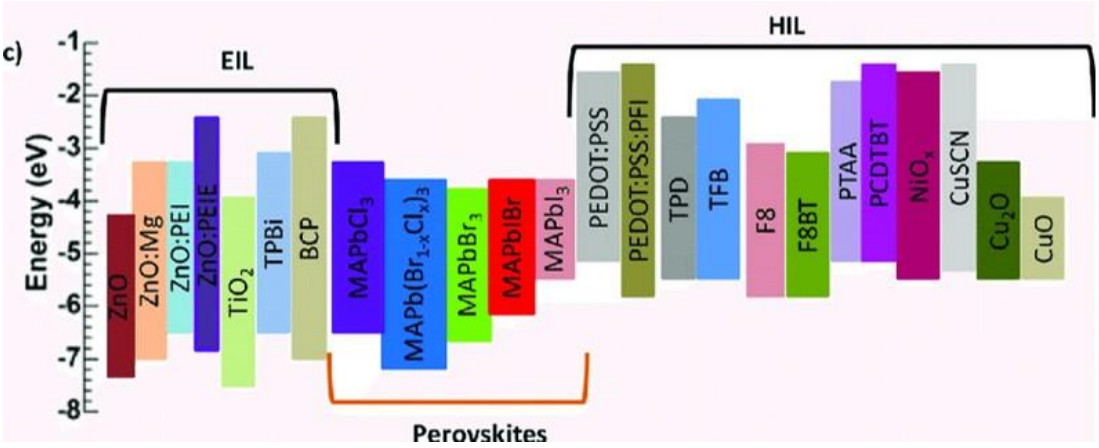

Figure 4.5:Bandgaps for various electron injection layers (EIL), perovskites, and hole injection layers (HIL). [7]

Figure 4.6a shows a basic structure for a LED device with an anode, active layer, and cathode. These devices depend on a built-in voltage, V_{bi} between the anode and the cathode of the device. The built-in voltage is defined as the difference

between the anode injection level and the cathode injection level. Figure 4.6b-c shows the band energy diagrams of the simplified device under different applied voltage.

Figure 4.6b describes the different important energy levels associated with the device: Φ_A is the work function of the anode electrode, Φ_C is the work function of the cathode electrode, φ is the ionization energy of the active layer, χ is the electron affinity, ϕ is the energy barrier for electrons, and Δ is the energy barrier for holes. When a voltage less than the built-in voltage is applied the LED as in Figure 4.6d, it is difficult to inject carriers into the active layer because the barriers between the injection layers and the active layer become large, this region is called reverse bias [8].

The current generated in this case is dependent on thermally generated intrinsic charge carriers. There are a low number of these charge carriers, so the current is low when voltage is applied in this direction. At the built-in voltage, the band bending from the reverse bias disappears and the energy band are flat band as shown in Figure 4.6c. Diodes, and LEDs by extension, will conduct large amounts of current when operated in forward bias. This is the case when the applied voltage is larger than the built-in voltage. The causes a bend in the energy bands to lower the barrier energy for injection of electrons and holes compared to the reverse bias condition, and a much higher current will be present in the material, Figure 4.6e[8]. This accumulation of electrons and holes will result in radiative recombination for the case of LEDs, and electroluminescence (EL) will occur.

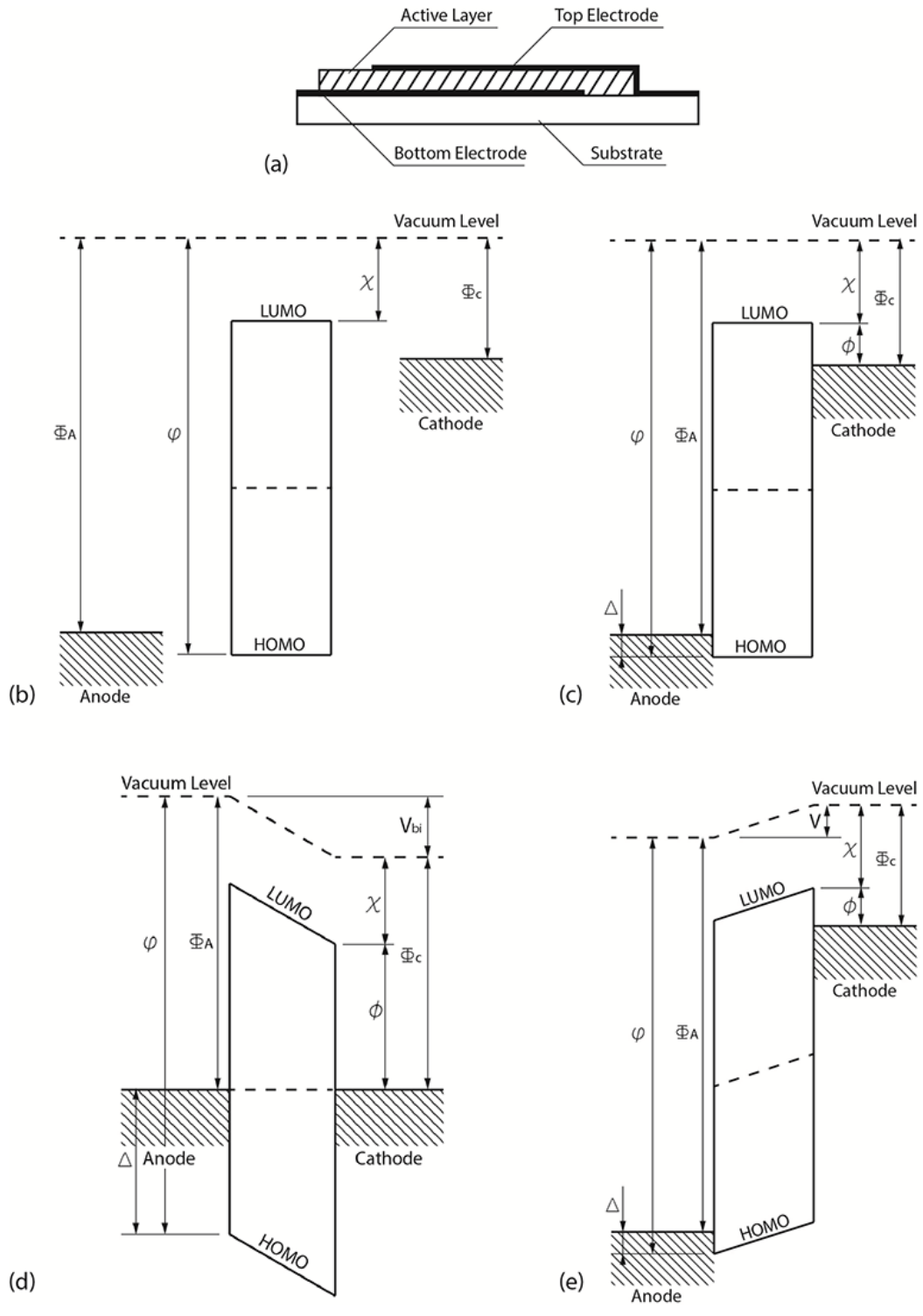

Figure 4.6: LED basics. a) LED cross section, b) Energy levels of layers, c) Voltage applied is equal to built in voltage, d) Reverse bias, e) Forward bias [8]

An example of a J-V curve of an LED is shown in Figure 4.7. Figure 4.7 also shows the radiance in W/m^2 of the LED with a turn-on voltage of 2V. This figure shows the low current in the reverse bias region, with an increase in current in the forward bias region with light emission. The turn-on voltage of the LED is defined by the bandgap of the active layer, the metal contacts, and the thickness and quality of the active layer. There are two primary current forces that are important to diode functionality: drift current and diffusion current. Diffusion current occurs when carriers are moving from a high concentration area to a low concentration area, this is the current that dominates the reverse bias region. Drift current occurs when an electric field is applied to the diode. The electric field will force electrons one direction and holes in the opposite direction. This current dominates the forward bias region[9].

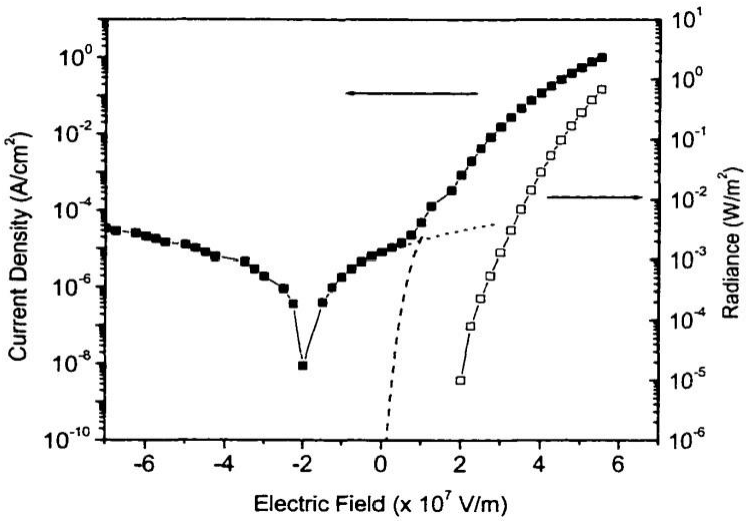

Figure 4.7: Example of an LED J-V and radiance curve. [9]

The efficiency of the LED can be quantified by external quantum efficiency (EQE) calculations which relate to the number of photons out per electrons in. The electrons into the device can be found by manipulating the current, since current is Coulombs per second, the number of electrons per second, the EQE can be found using this equation:

$$EQE = \frac{\Phi}{J/q} \qquad (4.4$$

where Φ is the photon flux [photons/cm^2/s], J is current density [A/cm^2] and q is the charge of an electron [C/electron]. The photon flux can be measured using a calibrated spectrometer that integrates the spectra of the electroluminescence for a given integration time.

4.4 Conclusions

Using the techniques discussed in this section will allow for the perovskite films and quantum dots to be optimized for optoelectronics. Optical and surface testing is typically conducted on neat films spun on glass substrates, while electrical testing typically requires a device to be fabricated with many different layers involved.

4.5 References

[1] Baranowski M, Plochocka P. Excitons in Metal-Halide Perovskites. Advanced Energy Materials 2020;10:1903659. https://doi.org/10.1002/aenm.201903659.

[2] Coulter JB, Birnie III DP. Assessing Tauc Plot Slope Quantification: ZnO Thin Films as a Model System. Physica Status Solidi (b) 2018;255:1700393. https://doi.org/10.1002/pssb.201700393.

[3] Gull S, Jamil MH, Zhang X, Kwok H, Li G. Stokes Shift in Inorganic Lead Halide Perovskites: Current Status and Perspective. ChemistryOpen 2022;11:e202100285. https://doi.org/10.1002/open.202100285.

[4] Fang F, Chen W, Li Y, Liu H, Mei M, Zhang R, Hao J, Mikita M, Cao W, Pan R, Wang K, Sun XW. Employing Polar Solvent Controlled Ionization in Precursors for Synthesis of High-Quality Inorganic Perovskite Nanocrystals at Room Temperature. Advance Functional Materials. 2018;28;10:176000. **https://doi.org/10.1002/adfm.201706000**.

[5] Hellier K. Understanding the Impact of Local Structure on Materials for Optoelectronic Applications. UC Santa Cruz, 2020.

[6] Cullity B, Stock, S. Elements of X-Ray Diffraction. Prentice Hall 2001.

[7] Kumawat NK, Gupta D, Kabra D. Recent Advances in Metal Halide-Based Perovskite Light-Emitting Diodes. Energy Technology 2017;5:1734–49. https://doi.org/10.1002/ente.201700356.

[8] Santos LF, Gozzi G. Electrical Properties of Polymer Light-Emitting Devices. IntechOpen; 2016. https://doi.org/10.5772/64358.

[9] Bozano LD. Charge and light in polymers: Steady-state and transient electroluminescence studies in organic light emitting diodes. Ph.D. University of California, Santa Cruz, n.d.

Chapter 5 Effects of various antisolvent washes on $MAPbBr_3$

Perovskite optoelectronic devices offer an advantage over traditional semiconductor devices due to their potential to be made at low-cost using solution processing while maintaining excellent electronic properties. The role of fabrication on crystal formation for bromide perovskite systems is still not fully understood. To further this understanding, this work compares the effects of different antisolvent washes when creating solvent engineered $MAPbBr_3$ films. The crystal structure of the films was confirmed via XRD. The film surface morphology was characterized using AFM showing roughness values that ranged from 43.2 nm to 4.3 nm depending on antisolvent wash. Enhanced photoluminescence was found in the antisolvent washes compared to films not treated with antisolvent, and the antisolvent wash was shown to influence the photoluminescence. Photothermal deflection spectroscopy was used to compare trap densities and general order within the films and found that the overall order of the films was high, regardless of antisolvent wash.

5.1 Introduction

Hybrid organic inorganic perovskites (HOIP) have become an area of interest for optoelectronic devices. Properties such as tunable and direct bandgaps, high color purity, high absorption coefficients, low exciton binding energies, and long charge carrier diffusion lengths have led researchers to work with perovskites for a wide array of applications [1-10]. Beyond these beneficial properties, HOIPs can also be fabricated at much lower temperatures and costs compared to traditional inorganic semiconductors. There are many ways to fabricate perovskite films. Each method

affects the morphology, which in turn affects device performance [11]. This work will be focused on one step film formation of methylammonium lead bromide ($MAPbBr_3$) using polar solvents N,N dimethyl formamide (DMF) and dimethyl sulfoxide (DMSO). Using a mixture of DMF and DMSO has been shown to have favorable effects on the perovskite crystal formation during one step fabrication [12]. One step films are created by dissolving both precursors, lead bromide ($PbBr_2$) and methylammonium bromide (MABr), into the same polar solvent, in this case a mixture of DMF and DMSO, then spin coating the film in one thin layer.

A challenge of solution processed perovskite films is the surface morphology and the development of pinholes in the films which lead to poor device performance [13-16]). With the use of an antisolvent wash during spin coating, the nucleation of perovskite crystals is assisted which creates dense, pin-hole free films [17]. Many antisolvents have been used and studied for the formation of MAPbI3 [18-24], but fewer studies have been completed on the effects of antisolvent wash on MAPbBr3 [25-28]. The antisolvent must be miscible in the polar solvent used, so that the antisolvent can help pull excess polar solvent out of the film during spinning, as this is the primary factor in assisting the crystal growth of the perovskite. This study focuses on six antisolvents: acetone, ethanol, isopropyl alcohol (IPA), methyl acetate, n-butanol, and toluene and compares the antisolvent washed films to films spun with an unwashed film.

5.2 Experimental Methods

The perovskite solution was prepared by dissolving MABr in DMF in a molar ratio of 1 to 5. This solution was used to dissolve $PbBr_2$ in a 1 to 1 molar ratio of MABr and $PbBr_2$. Additional dilution of the perovskite mixture was done using DMF and DMSO. The final molar ratio of the solution was 1:1:15:5 for MABr, PbBr2, DMF, and DMSO, respectively. This solution was mixed on a stir plate for 1 hour prior to spinning. Films were spun on glass slides that had been cleaned using alconox, acetone, and ethanol washes. Prior to spinning the glass slides were heated to 100^{o}C. Films were spun at 3000rpm for 30 seconds and 400uL of antisolvent was dripped after 6 seconds. After spinning, the films were placed on a hot plate at 100^{o}C for 10 min to remove excess antisolvent. A control sample with no antisolvent wash was made using the same method, but no antisolvent dripping at 6 seconds.

Absorbance was measured using Jasco V-670 spectrophotmeter from 400 nm to 700 nm wavelength. X-ray diffraction was used to identify the crystalline structure of films spun on glass and was measured using a Rigaku Smartlab Powder and Thin Film Diffractometer at 1.5 degrees per minute and a step size of 0.01 degrees. Atomic force microscopy (AFM) was performed using an Oxford Cypher AFM in tapping mode on neat films spun on glass slides to measure the morphology of the films. The photoluminescence (PL) of neat films on glass slides was measured using Perkin-Elmer LS 45 Luminescence Spectrometer. The excitation wavelength was 395 nm. OD 30 filters were used to ensure the PL peaks were not saturated on the instrument. Photothermal deflection spectroscopy (PDS) was performed on neat films fabricated

with each antisolvent to study the generation of defects in the bulk of the sample. The setup of the PDS system is described in detail in previous works [29, 30].[51,52] Light incident upon the sample is absorbed and causes carrier excitation; upon thermal relaxation, the surrounding media is heated and a change in index of refraction occurs. A probe beam running parallel to the sample is then deflected due to the change in index of refraction. By modulating the excitation, the fluctuation in the laser can be measured and the absorption coefficient can be calculated.

Samples were submerged in FC-72 Fluorintert (3M), selected for a high gradient of index of refraction with respect to temperature. Optical excitation of the sample was carried out by pumping the sample at 5 Hz with variable monochromatic light, provided by a quartz tungsten halogen light source (Oriel 7340 dual monochromator illuminator) paired with an Acton SpectraPro monochromator, and filtered with 400, 700, 1000, or 1500 nm longpass filters (Thorlabs). The pump beam was split before interaction with the film and sampled by a pyroelectric photodetector (Gentec) for intensity reference. A probe beam consisting of a 632 nm HeNe laser (JDSU) was focused to a point in front of and parallel to the film, then tested for deflection by the knife edge method using an aperture and a position sensitive detector (Thorlabs PDP90A) outputting the laser intensity. Both the reference detector and the position sensitive detector were coupled to lock-in amplifiers for reduction of noise in the system. A LabVIEW program automated the monochromatic sweep and data collection, with the absorption coefficient calculated by

$$\alpha(\lambda) = -\frac{1}{d}\ln\left(1 - \frac{V_{sig}(\lambda)}{V_{ref}(\lambda)}C_{norm}\right) \qquad (5.1$$

where d is the sample thickness, V_{sig} is the voltage signal from the probe deflection, V_{ref} is the voltage signal from the reference detector, and C_{norm} is a scaling constant determined by the transmission of the sample taken from UV-Vis transmission, V_{sig}, and V_{ref} all at a specific wavelength. From this, the band gap was calculated by the Tauc method using $(\alpha \cdot h\nu)^2$ for a direct gap. The Urbach energy E_U, a measure of the disorder in the system, was calculated by $h\nu \sim E_U \ln \alpha$.

5.3 Results

A diverse selection of antisolvents were selected to determine if there was an optimal choice for enhanced PL and lower roughness. Table 5.1 shows the various properties of the antisolvents used in this study. The polarity of the solvent also ranged from 5.3 for acetone to 2.4 for toluene. Polarity is expected to affect the decomposition of the perovskite film in the antisolvent, with higher polarity expected to cause more decomposition and lower polarity causing very little decomposition. Antisolvents acetone and ethanol have been shown to decompose other forms of perovskite films, such as $MAPbI_3$ [18, 31]. The dipole moment ranged from 2.88D for acetone and 0.375D for toluene. Higher dipole moments reduce the likelihood of an intermediate phase developing during antisolvent dripping which leads to direct crystallization during antisolvent application [12, 32]. Boiling points ranged from

117.7°C for n-butanol to 56°C for acetone. Higher boiling points are expected to enhance grain growth during film formation [12].

Table 5.1:Antisolvents used for study with polarity, dipole moments, and boiling points for each antisolvents. [12, 18, 22, 28, 32]

Antisolvent	Polarity	Dipole Moment (D)	Boiling Point (°C)
Acetone	5.3	2.88	56
Ethanol	4.25	1.69	78
IPA	4.25	1.58	82.6
Methyl Acetate	4.4	1.71	56.9
n-Butanol	4.0	1.66	117.7
Toluene	2.4	0.375	111

X-ray diffraction (XRD) was performed to characterize the crystal structure of the films using the different anti-solvent washes, shown in Figure 5.1.

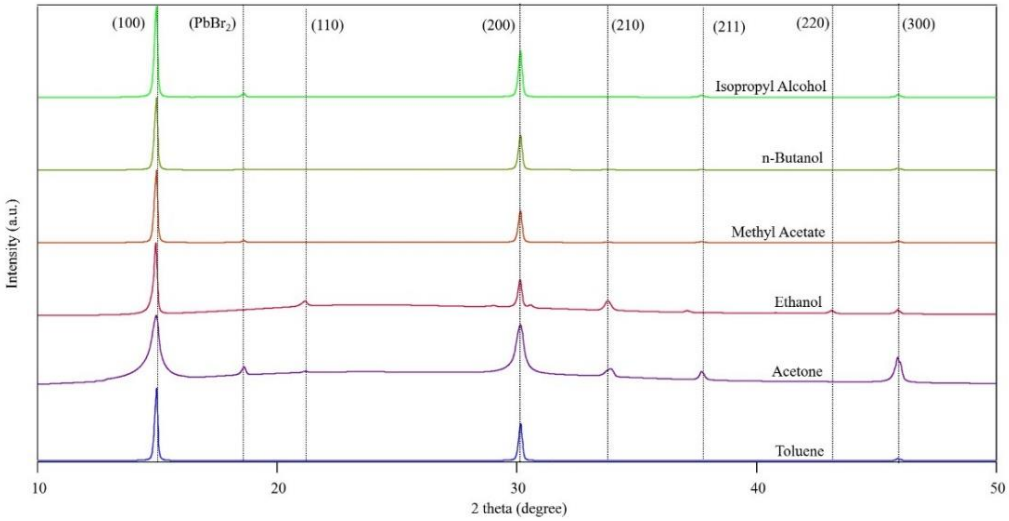

Figure 5.1:XRD of MAPbBr3 using various antisolvents.

Peaks were observed in all films at 15°, 30.12°, and 45.93° which corresponds to the (100), (200), and (300) planes in the cubic structure Pm3m. Additional peaks

can be seen in the films treated with acetone or ethanol which correspond to the (110) and (210) peaks [33]. These additional peaks in the ethanol and acetone films could be caused by the dissolution of the perovskite film, which leads to exposure of different grain orientations. The peak at 18.58° is caused by excess $PbBr_2$ [34]. The excess $PbBr_2$ is a common issue in films with a 1:1 molar ratio of MABr and $PbBr_2$ [27]. This confirms that the antisolvent wash does not affect the crystal structure of the $MAPbBr_3$.

As shown in Figure 5.2, UV-Vis absorption spectroscopy was performed on all films. All films showed a similar signature for the absorbance with differences stemming from the scattering of the surface of the films.

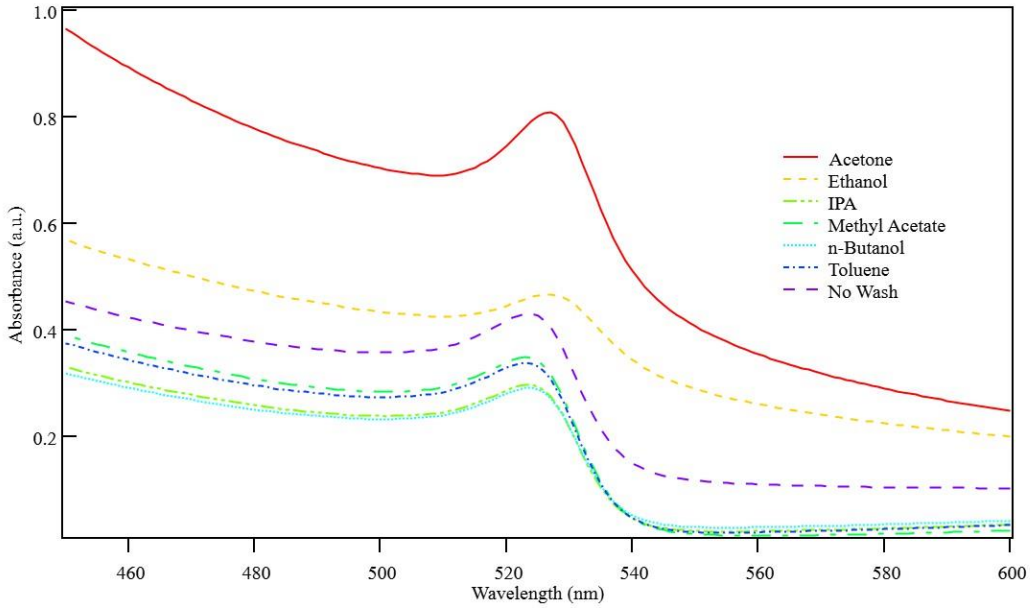

Figure 5.2:Absorbance of MAPbBr3 using various antisolvent washes.

Both the acetone and ethanol films, in general, had a more diffuse reflectance on the surface than the other antisolvent washes. This is caused by the decomposition

of the perovskite surface by the antisolvent due to their respective polarities which caused a higher surface roughness of the films.

Using PDS, the bandgap of each film was found via Tauc plot, and the values confirm the expected 2.30 eV bandgap for all films [35-37]. The scan for each of the films are shown in Figure 5.3.

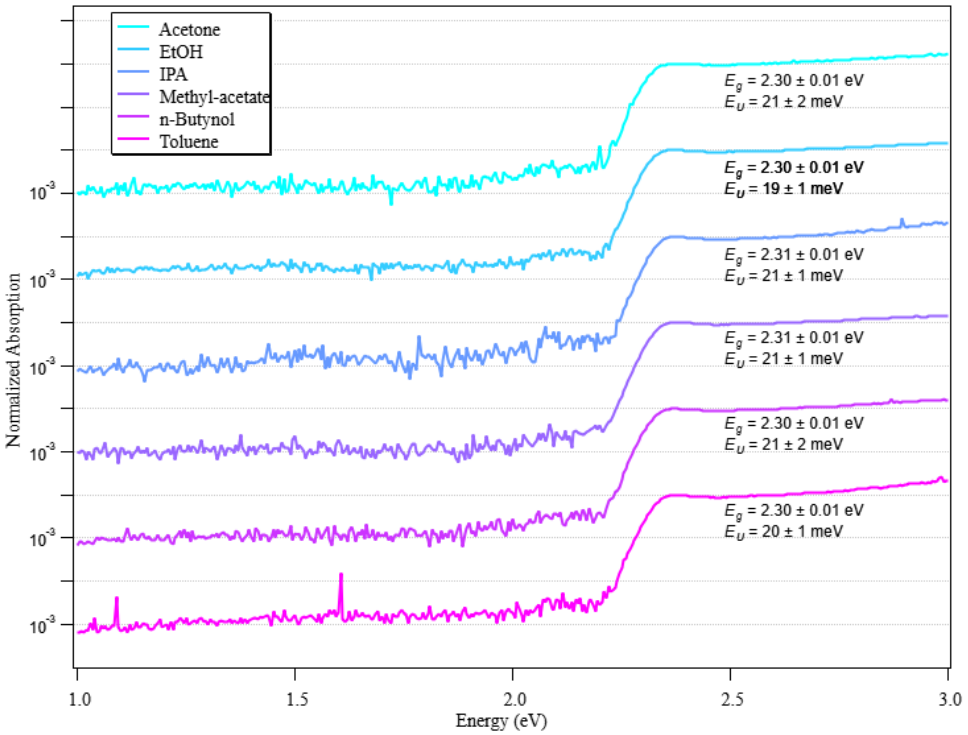

Figure 5.3: PDS of MAPbBr3 using various antisolvent washes.

The Urbach energy was also determined for each film. The Urbach energy describes transitions between band to trap states and this gives insight to the disorder present in the material. The Urbach energies for each antisolvent washed film ranged from 19 meV to 21 meV, which is very low and typical for perovskite thin films and comparable to findings in similar work [2, 38, 39]. The weak absorption tail is also

small in all films, this could be caused by the low number of deep traps in the material. The findings from PDS show films are all consistent within the bulk of the film, and the antisolvent wash does not affect the bulk of the film.

Atomic force microscopy (AFM) was used to observe the surface morphology effects of the different antisolvent washes on the films; images are shown in Figure 5.4. Use of any of the tested antisolvents affected the grain size dramatically as compared to not using an antisolvent at all. Results are shown in Table 5.2 for the average disc radius of the gains in each film. The films with no antisolvent wash had average grain sizes of 770 nm, while the average grain sizes for the anti-solvent washed films varied from 58 nm to 102 nm. This confirms the nanocrystalline pinning that is expected from the antisolvent wash [27].

Table 5.2: Grain size for MAPbBr3 using various antisolvent washes.

Antisolvent	Average Grain Size (disc radius), nm
Acetone	95 +/- 71
Ethanol	102 +/ 78
IPA	67 +/-45
Methyl Acetate	58 +/- 31
n-Butanol	59 +/- 38
Toluene	77 +/- 37
No Wash	770 +/- 662

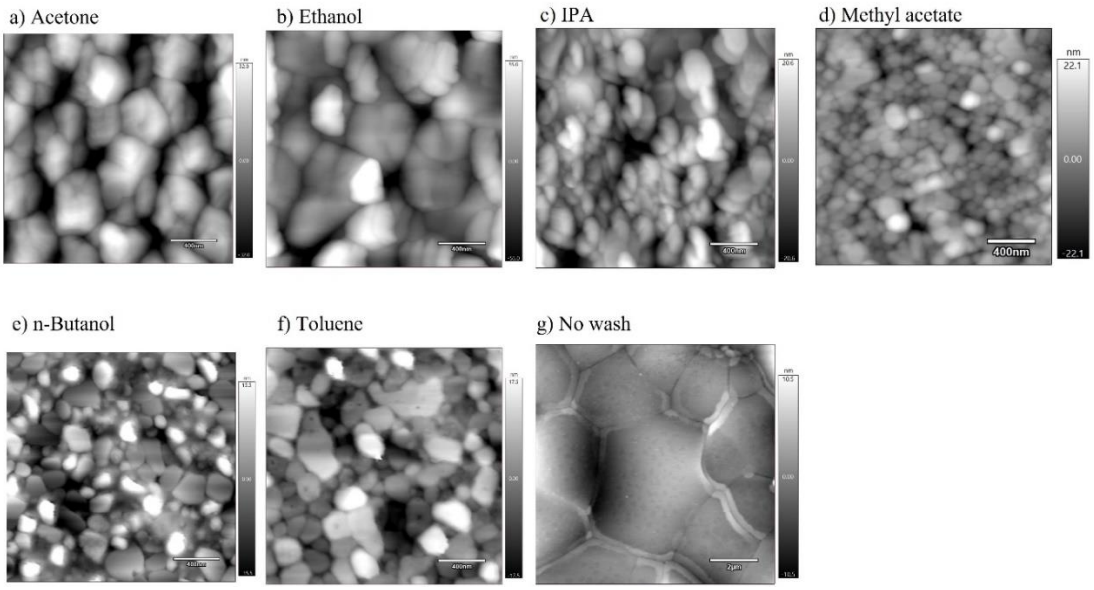

Figure 5.4: Figure 4. AFM images of grains in MAPbBr3 using various antisolvent washes. Scan area is 2 µm x 2 µm for a, b, c, d, e, and f. Because of the much larger grain size, a 10 µm x 10 µm scan area was used for g. Scale bar is 400 nm for a, b, c, d, e, and f. Scale bar is 2µm for g.

There is not a direct correlation between the antisolvent properties and the size of the grains. Previous work had shown that grain size is related to antisolvent boiling point, but that trend was not present in this work [40].

Root mean square (RMS) surface roughness was averaged for three films, and results are shown in Figure 5.5. The surface roughness and grain sizes from Table 5.1 follow a similar trend. The surface roughness varied by antisolvent with acetone and ethanol leaving a rougher film, which is likely caused by the decomposition of the perovskite film in both acetone and ethanol. Pinholes are present in the AFM images shown in Figure 5.6a,b. The other antisolvent washes had dense films, shown in Figure 5.6c-f.

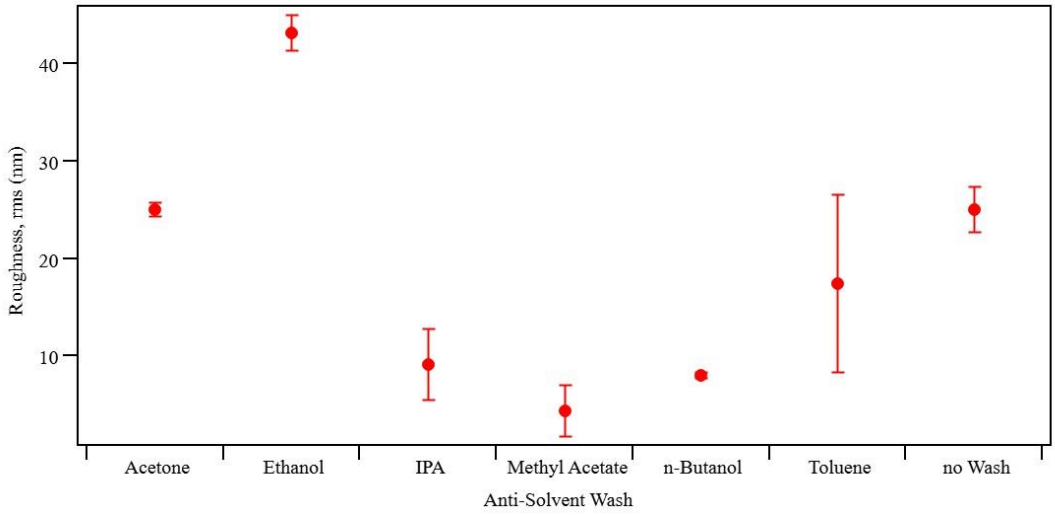

Figure 5.5: Average roughness for MAPbBr3 using various antisolvent washes on 30 µm x 30 µm AFM scans.

The films with no antisolvent wash, Figure 5.6g, had a higher rms roughness than the antisolvent washes that did not dissolve the perovskite, and a similar roughness to the acetone wash. The cause of this is due to the slower evaporation of DMF and DMSO during film formation [23].

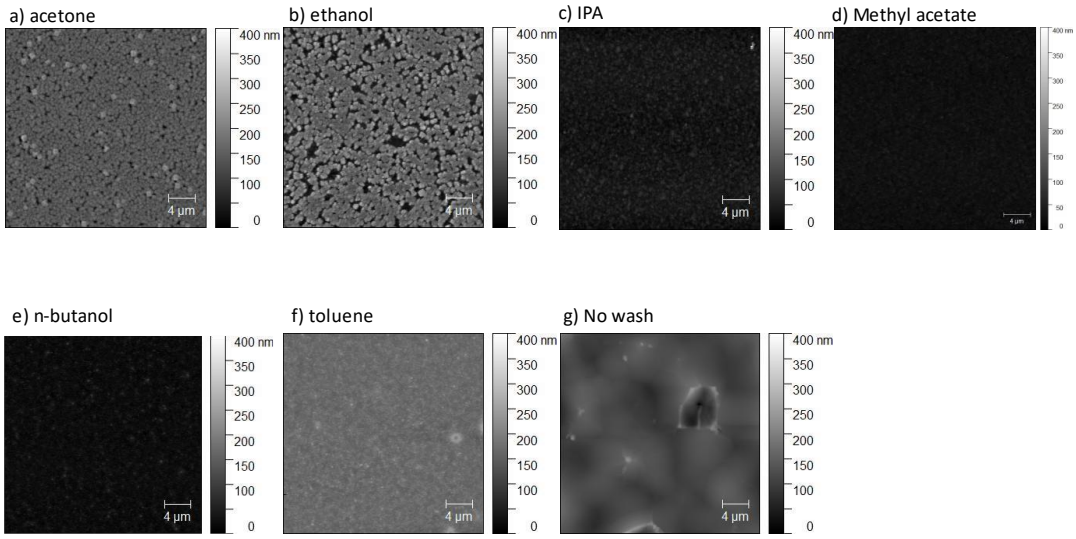

Figure 5.6: AFM images for surface roughness of MAPbBr3 using various antisolvent washes. Scan area: 30 µm x 30 µm. Scale bar is 6 µm for all figures.

The antisolvent wash was expected to increase the PL of the films due to the nanocrystalline pinning that occurs during film formation. The PL results are shown in Figure 5.7. Apart from methyl acetate, the other five antisolvent washes resulted in an increase in PL compared to the no wash sample. The methyl acetate film had very small grain sizes which could be the cause of the lowered PL; the grain boundaries can act as trap sites for the charge carriers and decrease radiative recombination [28]. The PL spectra for each film has a similar shape with the PL peak centered around 536 nm for all films. Acetone resulted in the highest average PL followed by n-butanol, ethanol, toluene, and IPA.

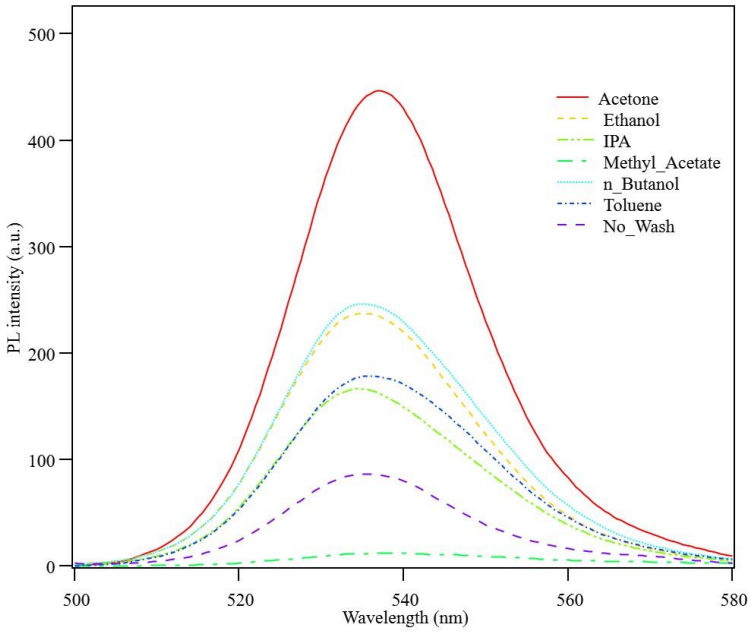

Figure 5.7: PL for MAPbBr3 using various antisolvent washes.

5.4 Conclusions

In summary, when formed using the one step process, the antisolvent wash has little effect on the crystal structure or level of disorder of the MAPbBr3. However, the antisolvent wash appears to have a larger effect on the surface of the films demonstrated by the differences in grain size and roughness in each film. The surface roughness increased when $MAPbBr_3$ was soluble in the antisolvent wash. The PL was also affected by the antisolvent wash. A possible cause of this could be the gain boundaries causing nonradiative recombination via trap states. The antisolvent washed film had, in general, lower surface roughness, smaller grains, and higher PL when compared to the films with no wash. The antisolvent n-butanol showed

promising PL and low surface roughness for the films which could lead to better quality devices.

5.5 References

1. M. R. Filip, G. E. Eperon, H. J. Snaith, F. Giustino, Nat. Commun. (2014) https://doi.org/10.1038/ncomms6757

2. R. Comin, G. Walters, E. Sol Thibau, O. Voznyy, Z.-H. Lu, E. H. Sargent, J. Mater. Chem. C (2015) https://doi.org/10.1039/C5TC01718A

3. F. Deschler, M. Price, S. Pathak, L. E. Klintberg, D.-D. Jarausch, R. Higler, S. Hüttner, T. Leijtens, S. D. Stranks, H. J. Snaith, M. Atatüre, R. T. Phillips, R. H. Friend, J. Phys. Chem. Lett. (2014) https://doi.org/10.1021/jz5005285

4. Z.-K. Tan, R. S. Moghaddam, M. L. Lai, P. Docampo, R. Higler, F. Deschler, M. Price, A. Sadhanala, L. M. Pazos, D. Credgington, F. Hanusch, T. Bein, H. J. Snaith, R. H. Friend, Nat. Nanotechnol. (2014) https://doi.org/10.1038/nnano.2014.149

5. Y. Wang, Y. Zhang, P. Zhang, W. Zhang, Phys. Chem. Chem. Phys. (2015) https://doi.org/10.1039/C5CP00448A

6. T. Miyasaka, Chem. Lett. (2015) https://doi.org/10.1246/cl.150175

7. V. D'Innocenzo, G. Grancini, M. J. P. Alcocer, A. R. S. Kandada, S. D. Stranks, M. M. Lee, G. Lanzani, H. J. Snaith, A. Petrozza, Nat. Commun. (2014) https://doi.org/10.1038/ncomms4586

8. G. Xing, N. Mathews, S. Sun, S. S. Lim, Y. M. Lam, M. Grätzel, S. Mhaisalkar, T. C. Sum, Science (2013) https://doi.org/10.1126/science.1243167

9. S. D. Stranks, G. E. Eperon, G. Grancini, C. Menelaou, M. J. P. Alcocer, T. Leijtens, L. M. Herz, A. Petrozza, H. J. Snaith, Science (2013) https://doi.org/10.1126/science.1243982

10. M. M. Lee, J. Teuscher, T. Miyasaka, T. N. Murakami, H. J. Snaith, Science (2012) https://doi.org/10.1126/science.1228604

11. L. Zheng, D. Zhang, Y. Ma, Z. Lu, Z. Chen, S. Wang, L. Xiao, Q. Gong, Dalton Trans. (2012) https://doi.org/10.1039/C4DT03869J

12. P. Zhao, B. J. Kim, X. Ren, D. G. Lee, G. J. Bang, J. B. Jeon, W. B. Kim, H. S. Jung, Adv. Mater. (2018) https://doi.org/10.1002/adma.201802763

13. W. Qiu, T. Merckx, M. Jaysankar, C. Masse de la Huerta, L. Rakocevic, W. Zhang, U. W. Paetzold, R. Gehlhaar, L. Froyen, J. Poortmans, D. Cheyns, H. J. Snaith, P. Heremans, Energy Environ. Sci. (2016) https://doi.org/10.1039/C5EE03703D

14. J. Xi, J. Yuan, X. Yan, D. Binks, J. Tian, ACS Appl. Energy Mater. (2020) https://doi.org/10.1021/acsaem.0c00778

15. D. N. Feria, C.-Y. Chang, K. P. O. Mahesh, C.-L. Hsu, Y.-C. Chao, Synth. Met. (2020) https://doi.org/10.1016/j.synthmet.2019.116283

16. J. C. Yu, D. B. Kim, E. D. Jung, B. R. Lee, M. H. Song, Nanoscale (2016) https://doi.org/10.1039/C5NR05604G

17. S. Paek, P. Schouwink, E. N. Athanasopoulou, K. T. Cho, G. Grancini, Y. Lee, Y. Zhang, F. Stellacci, M. K. Nazeeruddin, P. Gao, Chem. Mater. (2017) https://doi.org/10.1021/acs.chemmater.6b05353

18. J. Li, R. Yang, L. Que, Y. Wang, F. Wang, J. Wu, S. Li, J. Mater. Res. (2019) https://doi.org/10.1557/jmr.2019.122

19. S. Hyun Park, I. Su Jin, J. Woong Jung, Chem. Eng. J. (2021) https://doi.org/10.1016/j.cej.2021.131475

20. Y. Wang, T. Zhang, P. Zhang, D. Liu, L. Ji, H. Chen, Z. D. Chen, J. Wu, S. Li, Org. Electron. (2018) https://doi.org/10.1016/j.orgel.2018.02.043

21. Y. Wang, D. Liu, P. Zhang, T. Zhang, W. Ahmad, X. Ying, F. Wang, J. Li, L. Chen, J. Wu, Z. D. Chen, S. Li, Sci. China Mater. (2018) https://doi.org/10.1007/s40843-018-9263-7

22. J. Yi, J. Zhuang, Z. Ma, Z. Guo, W. Zhou, S. Zhao, H. Zhang, X. Luo, H. Li, Org. Electron. (2019) https://doi.org/10.1016/j.orgel.2019.03.021

23. M. Xiao, F. Huang, W. Huang, Y. Dkhissi, Y. Zhu, J. Etheridge, A. Gray-Weale, U. Bach, Y.-B. Cheng, L. Spiccia, Angew. Chem. Int. Ed. (2014) https://doi.org/10.1002/anie.201405334

24. J. Liu, N. Li, J. Jia, J. Dong, Z. Qiu, S. Iqbal, B. Cao, Sol. Energy **181**, 285 (2019) https://doi.org/10.1016/j.solener.2019.02.020

25. J.-W. Lee, Y. J. Choi, J.-M. Yang, S. Ham, S. K. Jeon, J. Y. Lee, Y.-H. Song, E. K. Ji, D.-H. Yoon, S. Seo, H. Shin, G. S. Han, H. S. Jung, D. Kim, N.-G. Park, ACS Nano (2017) https://doi.org/10.1021/acsnano.7b00608

26. S. Lee, J. H. Park, Y. S. Nam, B. R. Lee, B. Zhao, D. Di Nuzzo, E. D. Jung, H. Jeon, J.-Y. Kim, H. Y. Jeong, R. H. Friend, M. H. Song, ACS Nano (2018) https://doi.org/10.1021/acsnano.7b09148

27. H. Cho, S.-H. Jeong, M.-H. Park, Y.-H. Kim, C. Wolf, C.-L. Lee, J. H. Heo, A. Sadhanala, N. Myoung, S. Yoo, S. H. Im, R. H. Friend, T.-W. Lee, Science (2015) https://doi.org/10.1126/science.aad1818

28. L. Xu, S. Che, J. Huang, D. Xie, Y. Yao, P. Wang, P. Lin, H. Piao, H. Hu, C. Cui, F. Wu, D. Yang, X. Yu, Appl. Phys. Lett. (2019) https://doi.org/10.1063/1.5094248

29. H. R. Sully, K. Tabatabaei, K. Hellier, K. A. Newton, Z. Ju, L. Knudson, S. Zargar, M. Wang, S. M. Kauzlarich, F. Bridges, S. A. Carter, ACS Appl. Nano Mater. (2020) https://doi.org/10.1021/acsanm.0c00709

30. K. Tabatabaei, H. R. Sully, Z. Ju, K. Hellier, H. Lu, C. J. Perez, K. A. Newton, R. L. Brutchey, F. Bridges, S. A. Carter, S. M. Kauzlarich, ACS Nano (2021) https://doi.org/10.1021/acsnano.0c09352

31. T. Bu, L. Wu, X. Liu, X. Yang, P. Zhou, X. Yu, T. Qin, J. Shi, S. Wang, S. Li, Z. Ku, Y. Peng, F. Huang, Q. Meng, Y.-B. Cheng, J. Zhong, Adv. Energy Mater. (2017) https://doi.org/10.1002/aenm.201700576

32. B. J. Kim, D. H. Kim, S. L. Kwon, S. Y. Park, Z. Li, K. Zhu, H. S. Jung, Nat. Commun. (2016) https://doi.org/10.1038/ncomms11735

33. K.-H. Wang, L.-C. Li, M. Shellaiah, K. Wen Sun, Sci. Rep. (2017) https://doi.org/10.1038/s41598-017-13571-1

34. Z. Ahmad, A. Mishra, J. Mater. Sci.:Mater. Electron. (2020) https://doi.org/10.1007/s10854-020-03019-0

35. G. Mannino, I. Deretzis, E. Smecca, A. La Magna, A. Alberti, D. Ceratti, D. Cahen, J. Phys. Chem. Lett. (2020) https://doi.org/10.1021/acs.jpclett.0c00295

36. I. E. Castelli, J. M. García-Lastra, K. S. Thygesen, K. W. Jacobsen, APL Mater. (2014) https://doi.org/10.1063/1.4893495

37. M. D. Sampson, J. S. Park, R. D. Schaller, M. K. Y. Chan, A. B. F. Martinson, J. Mater. Chem. A (2017) https://doi.org/10.1039/C6TA09745F

38. P. Fedeli, F. Gazza, D. Calestani, P. Ferro, T. Besagni, A. Zappettini, G. Calestani, E. Marchi, P. Ceroni, R. Mosca, J. Phys. Chem. C (2015) https://doi.org/10.1021/acs.jpcc.5b03923

39. T.-C. Wei, H.-P. Wang, T.-Y. Li, C.-H. Lin, Y.-H. Hsieh, Y.-H. Chu, J.-H. He, Adv. Mater. (2017) https://doi.org/10.1002/adma.201701789

40. C.-C. Chen, S. H. Chang, L.-C. Chen, C.-L. Tsai, H.-M. Cheng, W.-C. Huang, W.-N. Chen, Y.-C. Lu, Z.-L. Tseng, K. Y. Chiu, S.-H. Chen, C.-G. Wu, Sol. Energy Mater. Sol. Cells (2017) https://doi.org/10.1016/j.solmat.2016.10.011

Chapter 6 Comparison between Oleylamine-Oleic Acid Ligands and 3,3-Diphenylpropylamine and Trans-cinnamic Acid Ligands for Methylammonium Lead Bromide Quantum Dots

Methylammonium lead bromide ($MAPbBr_3$) quantum dots were synthesized using a ligand assisted reprecipitation method. Two ligand sets were compared: oleic acid (OA) and oleylamine (OLA), and 3,3-diphenylpropylamine (DPPA) and trans-cinnamic acid (TCA). Quantum dots synthesized with DPPA-TCA showed an increased PLQY of 74.6% when compared to the 19.6% of OLA-OA quantum dot films. The surface morphology of the quantum dot films also exhibited an improvement when DPPA-TCA was used, resulting in films with a surface roughness of 37.4 nm. Light emitting diodes fabricated with DPPA-TCA quantum dot films also saw an increase in operation currents and lowered turn-on voltages.

6.1 Introduction

Perovskite quantum dots (PeQDs) have shown tremendous growth in optoelectronics in recent years. PeQDs can be synthesized using a method called ligand assisted reprecipitation (LARP) [1-5]. This method can be completed in ambient conditions and at low temperatures, while still maintaining the desirable high PLQY and high color purity of the quantum dot. This method involves using ligands to encapsulate the quantum dot during synthesis, and the ligand can have a dramatic effect on the properties of the PeQDs [6-8]. Much work for PeQDs using the LARP method have focused on long carbon chain organic molecules which tend to be

insulating in nature [1,4,5,9]. This can pose issues when using the quantum dot films in electrical devices, since transport is limited by the ligands. This work compares two sets of ligands used in the LARP method: oleylamine (OLA) and oleic acid (OA), and 3,3-diphenylpropylamine (DPPA) and trans-cinnamic acid (TCA).

6.2 Experimental Methods

6.2.1 Quantum dot synthesis

Two types of quantum dots were synthesized for comparison. The DPPA-TCA quantum dots were fabricated using a previously established method [8]. Perovskite precursors, methylammonium bromide (MABr) (9 mg) and lead bromid ($PbBr_2$) (73 mg), and TCA (59 mg) were dissolved in 400 µL of dimethylformamide (DMF). Next, DPPA (35 µL) was added to the solution and sonicated for 5 minutes or until the solution was clear. 100 µL of the precursor solution was injected into 5 mL of toluene stirring vigorously. The bright yellow PeQD solution was centrifuged at 6000 rpm for 5 minutes. The supernatant was discarded, and the solids were dispersed into 2 mL toluene. Then the PeQDs were centrifuged again. This process was repeated until the solids had been washed 3 times. After the final wash, the solids were dried overnight under vacuum. The dried PeQDs were re-dissolved in toluene with a concentration of 100 mg/mL.

The OLA-OA quantum dots were fabricated following a procedure outlined by Levchuk et al [5]. Perovskite precursors, MABr (11.2 mg) and $PbBr_2$ (36.7 mg) were dissolved in 1 mL DMF. Next, OA (200 µL) and OLA (16 µL) were added to the solution and sonicated for 5 minutes. 100 µL of precursor solution was injected

into 3 mL of toluene stirring vigorously. To precipitate the quantum dots, 3 mL of acetonitrile was added to the quantum dot solution and then centrifuged at 6000 rpm for 10 minutes. The supernatant was discarded, and the solids were dried overnight under vacuum. The dried PeQDs were re-dissolved in toluene with a concentration of 100 mg/mL.

6.2.2 Device and Film Fabrication

Neat films were spun on clean glass films for optical testing and film characterization. The films were spun using 30 µL quantum dot solution at speeds ranging from 2000 to 5000 rpm for 60 seconds at ambient conditions.

Light emitting diodes (LEDs) were fabricated using patterned indium tin oxide (ITO) on glass. Next, a layer of poly(3,4-ethylenedioxythiophene)-poly(styrenesufonate)(PEDOT:PSS) was deposited on the aluminum. 100 µL PEDOT:PSS was left on the substrate for 60 seconds prior to spinning at 3000 rpm for 60 seconds. The PEDOT:PSS layer was dried at 125ºC under vacuum for 1 hour minimum. A layer of poly(9-vinylcarbazaole) (PVK) in DMF (3 mg/mL) was spun at 3000 rpm for 60 seconds and then dried at 145ºC for 15 minutes. Quantum dot layers were spun at 5000 rpm for 60 seconds. Finally, 5 nm of calcium and 100 nm of aluminum were thermally evaporated as top contacts.

6.2.3 Characterization Methods

Fourier transform infrared (FTIR) was measured using a Perkin-Elmer Spectrum 1. Quantum dot films and ligands were spun on KBr pellets at speeds

ranging from 1000 rpm to 3000 rpm. The absolute photoluminescence quantum yield (PLQY) was measured on neat films spun on glass. The PLQY was measured with an Ocean Optics Jaz spectrometer, UV LED, and integrating sphere in absolute irradiance mode. The absolute PLQY was calculated by taking the photons emitted from the film divided by the total photons from the UV LED. PL measurements were taken using a Perkin-Elmer LS 45 Luminescence Spectrometer with excitation wavelength 387 nm and using an OD 110 filter to limit saturation. Absorbance measurements were completed using a Jasco V-65. Bandgaps for the quantum dot films were calculated using a Tauc fit of the absorbance data. Atomic force microscopy (AFM) was performed using an Oxford Cypher AFM in tapping mode on neat films spun on glass slides to measure the morphology of the films. LEDs were tested using a Kiethly 2400 sourcemeter and an Ocean Optics Jaz spectrometer in absolute irradiance mode with a 400 μm diameter fiber optic cable.

6.3 Results and Discussion

Previous work by Huang et al showed that when making OLA-OA quantum dots, if only OLA was used, the resulting quantum dot solution still had PL while when only OA was used, the solution precipitated out large particles and no longer had similar PL. This led to the belief that OLA dictates the kinetic reaction in the ligand assisted reprecipitation method and is the primary factor in creating the dot size. The OA ligands are used to stabilize the quantum dot solution [10, 11]. When this experiment was done on DPPA-TCA ligands, a similar result was discovered where DPPA ligands created a quantum dot solution that still have PL, and TCA

ligands created large particles that no longer had PL. This means that DPPA has a similar function as OLA in the quantum dot solution, and TCA acts as a stabilizer similar to OA.

As shown in Figure 6.1, the OLA-OA ligands and the DPPA-TCA ligands have dramatically different molecular structures. OLA and OA are both long chain carbon molecules with 18 carbons in the backbone of the molecule. These are considerably longer than DPPA and TCA which have rings rather than a long carbon chain. This reduction in ligand length, combined with the conjugation of the rings in DPPA and TCA, has been hypothesized to increase the transport of charge carriers in the quantum dot films. An additional benefit of DPPA and TCA is the increased

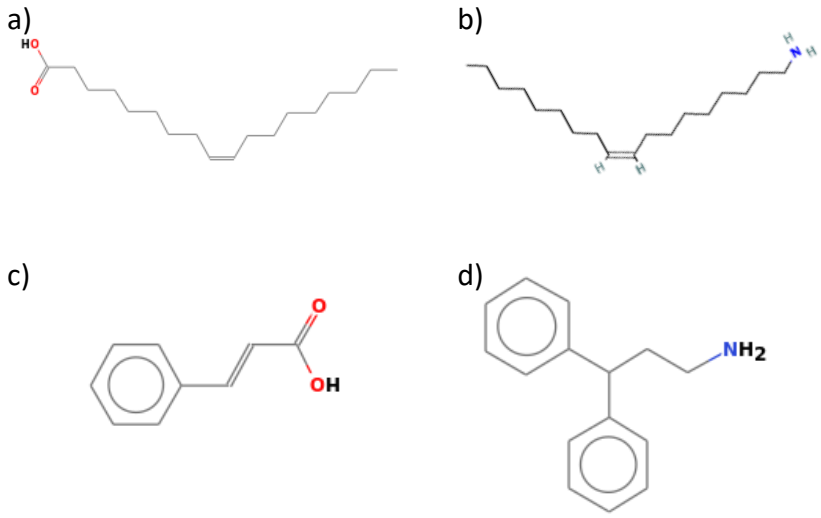

Figure 6.1: Ligand molecular structures. a) OA, b) OLA, c) TCA, d) DPPA [12,13]

branching may also increase the stability of the quantum dot. To ensure the ligands were present on the quantum dots, FTIR analysis was completed on films with both types of ligands.

Figure 6.2**Error! Reference source not found.** shows spectra for OLA-OA quantum dots, OLA, and OA. Both OLA and OA have very similar molecular structures seen in Figure 6.1, which explains the similarities between the two spectra. There are a few features unique to each molecule that can be used to verify if the ligand is present in the quantum dot film. Both OLA and OA show symmetric and asymmetric CH_2 stretching from the 2830 and 2902 cm^{-1} peaks respectively. The peak at 2988 cm^{-1} relates to a C-H bond [14]. These three peaks are all present in OLA-OA quantum dot film, so there is some confirmation that either or both OLA and OA are present in the film. OA has a peak at 1667 cm^{-1} which is related to the C=O bond in the carboxylic acid. This peak is present in the OLA-OA quantum dot spectrum, so OA is present in the quantum dot film. OLA has a distinct peak around 3300 cm^{-1} which corresponds to the N-H bond in the OLA molecule. This peak is not present in the OLA-OA quantum dot spectrum, but other peaks located around 1500 cm^{-1} are present in both OLA and OLA-OA quantum dot spectrum. These peaks are related to NH_2, so the OLA molecule is present in the OLA-OA quantum dot film. This confirms both ligands are present on the quantum dot. The broad peak on the OLA-OA quantum dot spectrum that is not present in ligand spectra is related to Br-H and O-H bonds [15].

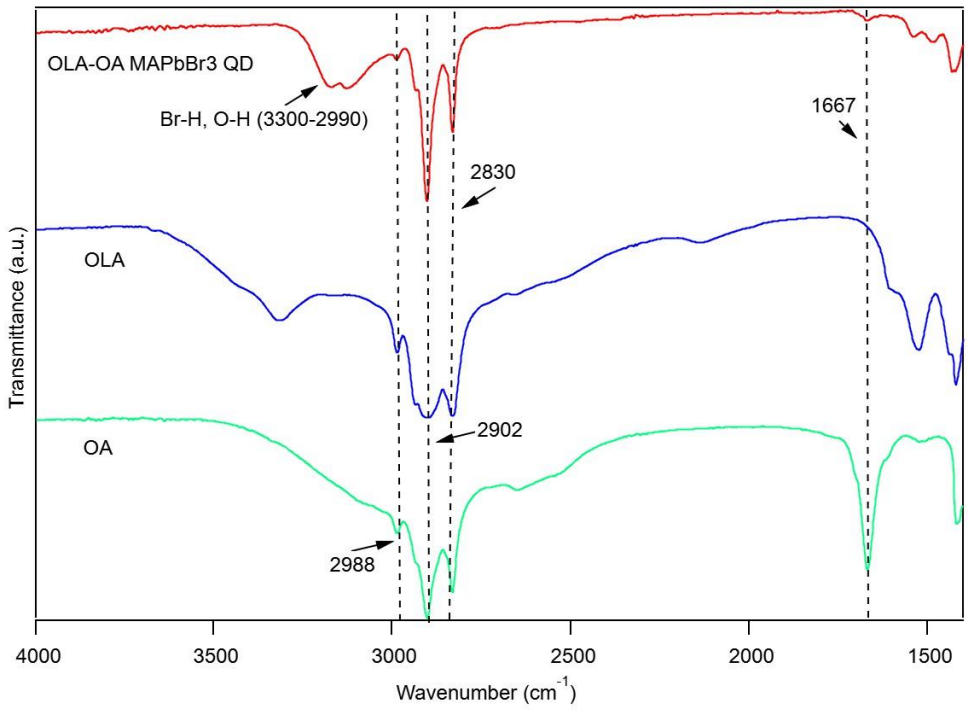

Figure 6.2: FTIR analysis of OLA, OA, and OLA-OA quantum dot films. OLA and OA spectra are from NIST [12].

Figure 6.3 shows the spectra for DPPA, TCA, and DPPA-TCA quantum dot films. The molecules for DPPA and TCA have more differences between them when compared to the OLA and OA molecules. Both have monosubstituted aromatic rings made up of C-H bonds. These bonds are represented by peaks in the 600 to 900 cm^{-1} which are present in all three spectra, confirming either or both DPPA and TCA are present in the DPPA-TCA quantum dot film. The peak at 1646 cm^{-1} corresponds to C=O bonds in the TCA. Since this peak is present also present in the DPPA-TCA quantum dot film, the presence of TCA is assumed. The presence of DPPA can be assumed due to the matching peaks at 1493 and 2878 cm^{-1} [8]. Again, the broad peak

as seen in the OLA-OA quantum dot film from 2900 to 3300 cm^{-1} is present which shows the Br-H and O-H bonds [15].

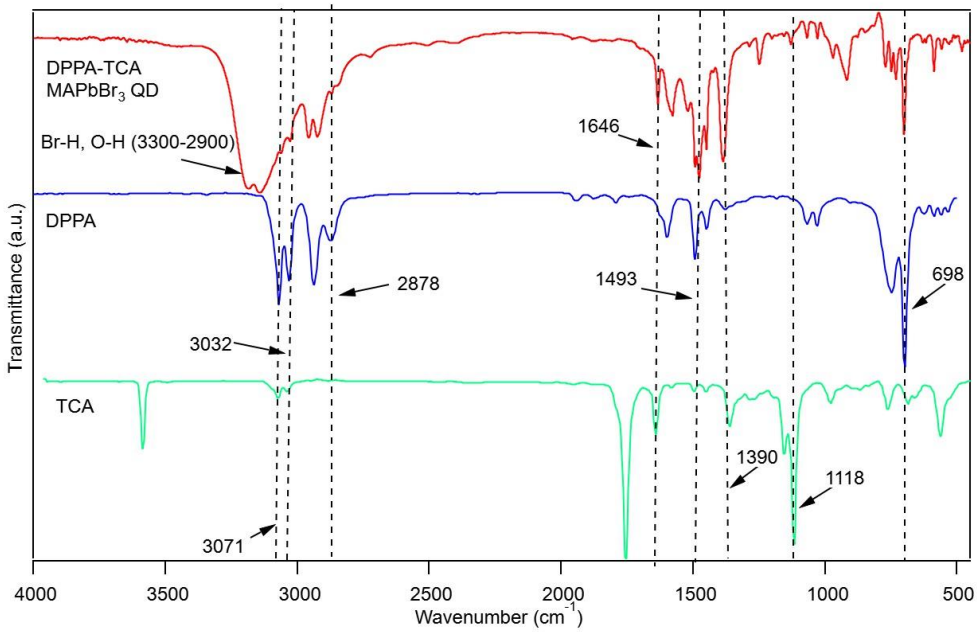

Figure 6.3: FTIR analysis of DPPA, TCA, and DPPA-TCA quantum dots. DPPA and TCA were from NIST [12].

The absolute PLQY for both DPPA-TCA and OLA-OA films is shown in Table 6.1. The DPPA-TCA quantum dots exhibit a much higher PLQY when compared to the OLA-OA quantum dots. Higher PLQYs in quantum dots generally signify more complete surface passivation, which will lead to fewer trap states on the surface of the quantum dot [1]. The increase in PLQY for the DPPA-TCA ligands shows that surface is more completed passivated when compared to the OLA-OA ligands.

Table 6.1: PLQY for DPPA-TCA and OLA-OA quantum dots

Sample	PLQY (%)
DPPA-TCA	74.7
OLA-OA	19.6

PL and absorbance were measured on glass slides. The results are shown in Figure 6.4. The absorbance for both types of quantum dots does not show a strong absorption edge, which is common for quantum dot films due to different dot sizes in the film. Since the LARP method depends the supersaturation of the precursor solution being injected to a vigorously stirring vial of toluene, the control on quantum dot size is not perfect, and differences in quantum dot size are expected [16]. The OLA-OA quantum dots seem to have a slightly larger spread in dot size as the absorbance has a small bump around 2.35 eV and then the final band edge around 2.6 eV. Table 6.2 show the summary of the optical properties derived from Figure 6.4. The PL peaks were 522 nm and 519 nm for the DPPA-TCA and OLA-OA quantum dots, respectively. This is a shift from the expected $MAPbBr_3$ bulk PL peak around 545 nm [17]. This shows the quantum confinement of the films since the PL peak has become blue shifted, meaning the bandgap has become larger. The bandgap energies of both films were calculated by Tauc plot using the absorbance spectrum. Again, the bandgap energy for the quantum dot films confirms the quantum confinement by showing an increase in bandgap energy when compared to bulk $MAPbBr_3$. The quantum dot films have bandgap energies of 2.43 eV and 2.40 eV for DPPA-TCA

and OLA-OA quantum dot films, respectively. The bandgap energy of bulk $MAPbBr_3$ is 2.30 eV [18].

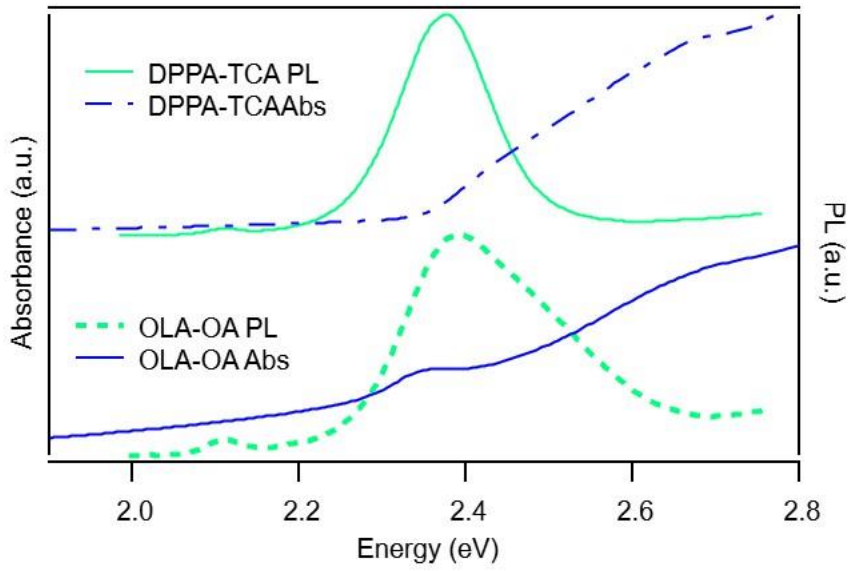

Figure 6.4: PL and absorbance for both DPPA-TCA and OLA-OA quantum dot films.

Perovskites are known for their high color purity, which can be characterized by the full width half maximum (FWHM) of the PL peak. The FWHM of DPPA-TCA quantum dots was 17.9 nm, which shows very high color purity. The OLA-OA quantum dots had a slightly larger FWHM of 28.9 nm, this is caused by the spread in sizes of the quantum dots.

Table 6.2: Optical properties of DPPA-TCA and OLA-OA quantum dot films

Sample	Peak PL (nm)	FWHM (nm)	Bandgap (eV)
DPPA-TCA	522	17.9 +/- 0.1	2.43 +/- 0.01
OLA-OA	519	28.9 +/- 0.4	2.40 +/- 0.01

The surface roughness and AFM scans are shown in Table 6.3 and Figure 6.5. The DPPA-TCA films have small particles present on the film which may be clumps of quantum dots not well dispersed in the toluene. This contributes to the root mean square (RMS) roughness of 37.4 nm. Additional filtration steps could possibly improve this surface roughness. The OLA-OA quantum dot films had a much higher RMS roughness at 101.6 nm. This surface has more of an appearance of grains similar to the polycrystalline films of bulk $MAPbBr_3$.

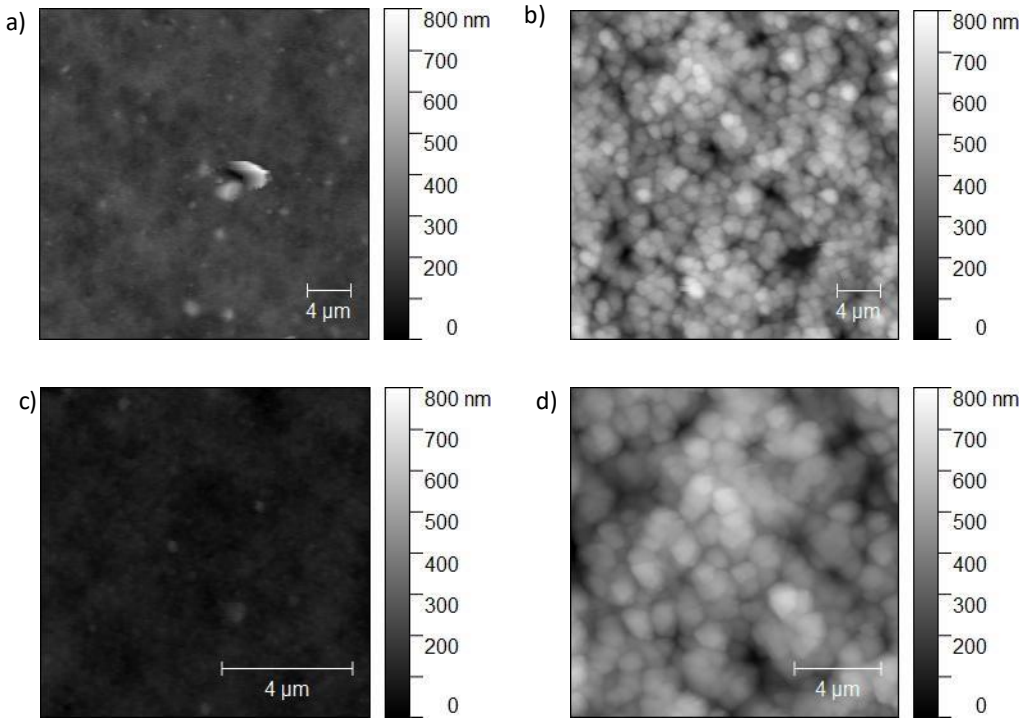

Figure 6.5: AFM scans of quantum dot films. a) DPPA-TCA 30 µm x 30 µm, b) OLA-OA 30 µm x 30 µm, c) DPPA-TCA 10 µm x 10 µm, d) OLA-OA 15 µm x 15 µm. Scale bar 4 µm.

Table 6.3: Surface Roughness for quantum dot films

Sample	Surface Roughness (nm)
DPPA-TCA	37.4 +/- 23.1
OLA-OA	101.6 +/- 12.2

LEDs were fabricated with both quantum dot films using the structure shown in Figure 6.6. The current density and radiance for both quantum dot films are shown in Figure 6.7 and Figure 6.8. These plots are averages of four devices.

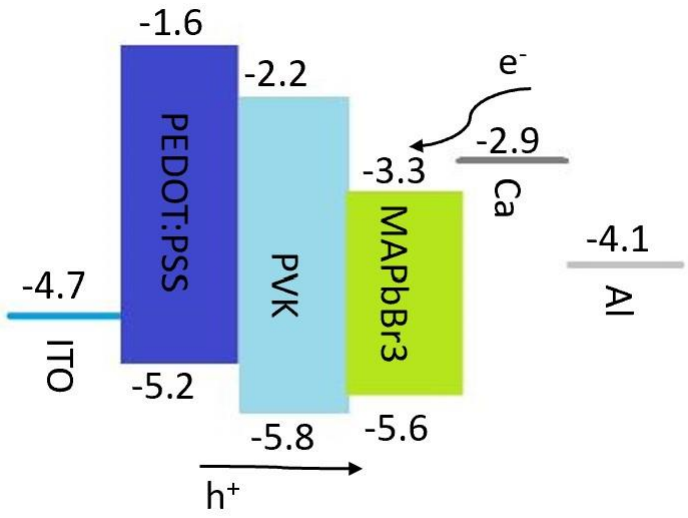

Figure 6.6: LED energy structure

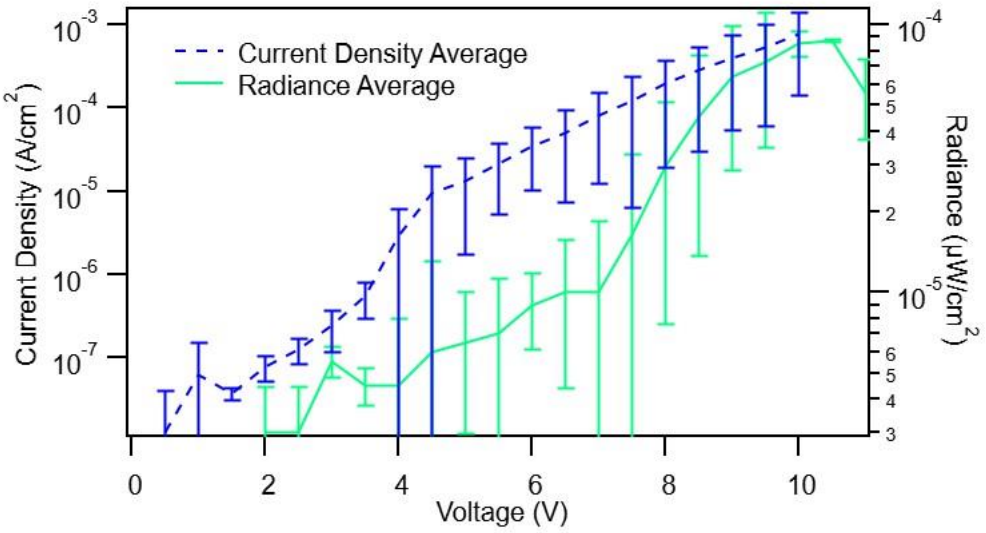

Figure 6.7: OLA-OA Current density and Radiance as a function of voltage.

The OLA-OA LEDs had a higher turn-on voltage at 6V, while the DPPA-TCA LEDs had a turn-on voltage of 3V. The DPPA-TCA LED had a maximum radiance that was 1.1x larger than the OLA-OA LEDs, but the DPPA-TCA LED required less voltage for the same radiance at 6V compared to 10.5V, respectively. The insulating nature of the OLA-OA ligands is also apparent when comparing the current densities. The DPPA-TCA current was much higher than the OLA-OA current over the operation. At 6V, the DPPA-TCA LED had a current density of 0.529 A/cm^2 and the OLA-OA LED had a current density of 47.9 μA/cm^2.

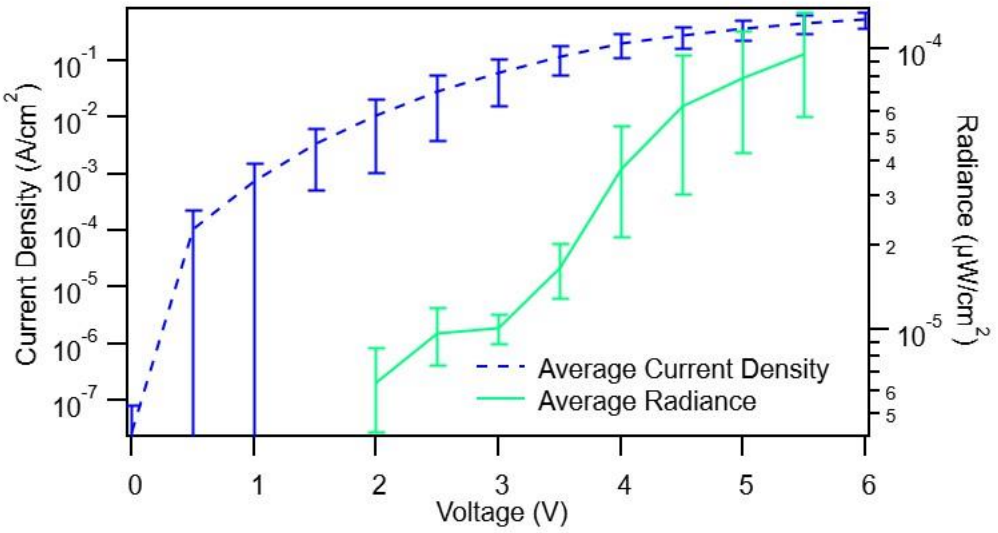

Figure 6.8: DPPA-TCA LED Current density and Radiance as a function of voltage.

6.4 Conclusions

The DPPA-TCA ligands offer an improvement to $MAPbBr_3$ quantum dots over the more common OLA-OA quantum dots. The DPPA-TCA ligands have a better surface passivation which increases the PLQY from 19.6% for OLA-OA quantum dots to 74.7% for DPPA-TCA quantum dots. The quantum confinement of both quantum dot films had similar levels of quantum confinement leading to energy bandgaps of 2.43 eV (DPPA-TCA) and 2.40 eV (OLA-OA). The surface morphology of the DPPA-TCA quantum dot films was considerably improved compared to the OLA-OA, from 37.4 nm and 101.6 nm. This film roughness could be improved upon by adding a filtration step prior to spinning the quantum dot film. The conductivity of the ligands had a direct correlation to the current flow in the LED, and the DPPA-

TCA quantum dots exhibited a lower turn-on voltage of 3V when compared to the OLA-OA quantum dots.

6.5 References

[1] Zhang F, Zhong H, Chen C, Wu X, Hu X, Huang H, et al. Brightly Luminescent and Color-Tunable Colloidal CH3NH3PbX3 (X = Br, I, Cl) Quantum Dots: Potential Alternatives for Display Technology. ACS Nano 2015;9:4533–42. https://doi.org/10.1021/acsnano.5b01154.

[2] Costa WC, Salla CAM, Ely F, Bechtold IH. Highly emissive $MAPbBr_3$ perovskite QDs by ligand-assisted reprecipitation: the antisolvent effect. Nanotechnology 2022;33:095702. https://doi.org/10.1088/1361-6528/ac3bf1.

[3] Sun S, Yuan D, Xu Y, Wang A, Deng Z. Ligand-Mediated Synthesis of Shape-Controlled Cesium Lead Halide Perovskite Nanocrystals *via* Reprecipitation Process at Room Temperature. ACS Nano 2016;10:3648–57. https://doi.org/10.1021/acsnano.5b08193.

[4] Zhang F, Zhong H, Chen C, Wu X, Hu X, Huang H, et al. Brightly Luminescent and Color-Tunable Colloidal $CH_3NH_3PbX_3$ (X = Br, I, Cl) Quantum Dots: Potential Alternatives for Display Technology. ACS Nano 2015;9:4533–42. https://doi.org/10.1021/acsnano.5b01154.

[5] Levchuk I, Herre P, Brandl M, Osvet A, Hock R, Peukert W, et al. Ligand-assisted thickness tailoring of highly luminescent colloidal CH3NH3PbX3 (X=Br, I) perovskite nanoplatelets. Chemical Communications 2016;53:244–7. https://doi.org/10.1039/C6CC09266G.

[6] Vickers ET, Graham TA, Chowdhury AH, Bahrami B, Dreskin BW, Lindley S, et al. Improving Charge Carrier Delocalization in Perovskite Quantum Dots by Surface Passivation with Conductive Aromatic Ligands. ACS Energy Lett 2018;3:2931–9. https://doi.org/10.1021/acsenergylett.8b01754.

[7] Dai J, Xi J, Li L, Zhao J, Shi Y, Zhang W, et al. Charge Transport between Coupling Colloidal Perovskite Quantum Dots Assisted by Functional Conjugated Ligands. Angewandte Chemie International Edition 2018;57:5754–8. https://doi.org/10.1002/anie.201801780.

[8] Vickers ET, Enlow EE, Delmas WG, DiBenedetto AC, Chowdhury AH, Bahrami B, et al. Enhancing Charge Carrier Delocalization in Perovskite Quantum Dot Solids with Energetically Aligned Conjugated Capping Ligands. ACS Energy Lett 2020;5:817–25

[9] Levchuk I, Osvet A, Tang X, Brandl M, Perea JD, Hoegl F, et al. Brightly Luminescent and Color-Tunable Formamidinium Lead Halide Perovskite FAPbX $_3$ (X = Cl, Br, I) Colloidal Nanocrystals. Nano Lett 2017;17:2765–70. https://doi.org/10.1021/acs.nanolett.6b04781.

[10] Huang H, Bodnarchuk MI, Kershaw SV, Kovalenko MV, Rogach AL. Lead Halide Perovskite Nanocrystals in the Research Spotlight: Stability and Defect Tolerance. ACS Energy Lett 2017;2:2071–83. https://doi.org/10.1021/acsenergylett.7b00547.

[11] Huang H, Susha AS, Kershaw SV, Hung TF, Rogach AL. Control of Emission Color of High Quantum Yield CH3NH3PbBr3 Perovskite Quantum Dots by Precipitation Temperature. Advanced Science 2015;2:1500194. https://doi.org/10.1002/advs.201500194.

[12] Informatics NO of D and. NIST Chemistry WebBook n.d. https://doi.org/10.18434/T4D303.

[13] PubChem. Oleylamine n.d. https://pubchem.ncbi.nlm.nih.gov/compound/5356789 (accessed May 2, 2022).

[14] Perez De Berti IO, Cagnoli MV, Pecchi G, Alessandrini JL, Stewart SJ, Bengoa JF, et al. Alternative low-cost approach to the synthesis of magnetic iron oxide nanoparticles by thermal decomposition of organic precursors. Nanotechnology 2013;24:175601. https://doi.org/10.1088/0957-4484/24/17/175601.

[15] Jancik Prochazkova A, Scharber MC, Yumusak C, Jančík J, Másilko J, Brüggemann O, et al. Synthesis conditions influencing formation of MAPbBr3 perovskite nanoparticles prepared by the ligand-assisted precipitation method. Sci Rep 2020;10:15720. https://doi.org/10.1038/s41598-020-72826-6.

[16] Han D, Imran M, Zhang M, Chang S, Wu X, Zhang X, et al. Efficient Light-Emitting Diodes Based on *in Situ* Fabricated FAPbBr 3 Nanocrystals: The Enhancing Role of the Ligand-Assisted Reprecipitation Process. ACS Nano 2018;12:8808–16. https://doi.org/10.1021/acsnano.8b05172.

[17] Comin R, Walters G, Sol Thibau E, Voznyy O, Lu Z-H, H. Sargent E. Structural, optical, and electronic studies of wide-bandgap lead halide perovskites. Journal of Materials Chemistry C 2015;3:8839–43. https://doi.org/10.1039/C5TC01718A.

[18] Mannino G, Deretzis I, Smecca E, La Magna A, Alberti A, Ceratti D, et al. Temperature-Dependent Optical Band Gap in CsPbBr3, MAPbBr3, and FAPbBr3 Single Crystals. J Phys Chem Lett 2020;11:2490–6. https://doi.org/10.1021/acs.jpclett.0c00295.

Chapter 7 A Study of the Addition of Oxide and Polymer Additives to Perovskite Quantum Dot Solution and the Effects on Film Formation and Device Performance

Perovskite quantum dots (PeQD) have shown promise in creating light-emitting diodes (LED) due to their high luminescence and tunable bandgaps. Challenges are still present in creating consistent films for devices. This study is focused on adding oxides and polymers to the quantum dot solution to investigate if the surface morphology and uniformity can be improved. Methylammonium lead bromide ($MAPbBr_3$) perovskite quantum dots will be created using a ligand-assisted reprecipitation (LARP) method with 3,3-Diphenylpropylamine (DPPA) and trans-cinnamic acid (TCA) ligands. Photoluminescence (PL), and atomic force microscopy (AFM) will be used to characterize the films. Devices, such as LEDs and single-carrier devices, will be fabricated and compared to investigate the effects of each additive.

7.1 Introduction

Perovskite quantum dots are an exciting field in optoelectronics due to their high photoluminescence, high color purity, and easy synthesis. An issue with quantum dot films in electrical devices is the limited charge transport. To overcome this issue, conductive ligands 3,3-diphenylpropylamine (DPPA) and trans-cinnamic acid (TCA) have been used as ligands to increase the mobilities of the charge carriers

of the quantum dot solution [1]. An issue with these quantum dots for use in devices is the film surface roughness and inconsistency.

To attempt to improve the film quality, oxide and polymer additives have been added to the quantum dot solution to create a composite film with improved features. Previous work has shown that adding oxides to semiconductor polymers enhances current densities, radiance, and power efficiencies [2]. Other work with perovskites has shown promise with adding different polymers to the perovskite layers. Experimentation with insulating polymers has been shown to increase stability of the quantum dot films in ambient conditions while maintaining the high PLQY of the quantum dots[3]. Other groups have focused on incorporating polymers with the PeQD film layer to assist in charge transport or charge blocking using a wide variety of polymers, but there is no direct comparison between insulating, electron injection, and hole injection polymer additives [4-7].

7.2 Experimental Methods

Quantum dot solutions were made via a ligand assisted method in ambient conditions[1]. Perovskite precursors, methylammonium bromide (MABr) (9 mg) and lead bromide ($PbBr_2$) (73 mg), and TCA (59 mg) were dissolved in 400 µL of dimethylformamide (DMF). Next, DPPA (35 µL) was added to the solution and sonicated for 5 minutes or until the solution was clear. 100 µL of the precursor solution was injected into 5 mL of toluene stirring vigorously. The bright yellow PeQD solution was centrifuged at 6000 rpm for 5 minutes. The supernatant was discarded, and the solids were dispersed into 2 mL toluene. Then the PeQDs were centrifuged again. This

process was repeated until the solids had been washed 3 times. After the final wash, the solids were dried overnight under vacuum. The dried PeQDs were re-dissolved in toluene with a concentration of 100mg/mL.

Oxides were added to the PeQD colloidal solution with a 2% by weight ratio. Polymers were added to the PeQD colloidal solution with a 10% by weight ratio. The PeQD solutions were then sonicated for 30 minutes to ensure dispersion of the additives in the colloidal solution prior to deposition. Two batches of PeQDs were synthesized, with one batch used for the oxide additives and the other batch used for polymer additives to ensure comparison between the different types of additives.

Neat films were fabricated by spin coating the PeQD solutions on cleaned glass slides at 3000-5000 rpm for 60 seconds at ambient conditions. Electron only devices were created using 100 nm of aluminum thermally evaporated on glass slides. A PeQD layer was deposited via spin coating at 3000 rpm for 60 seconds. A second 100 nm layer of aluminum was then thermally evaporated on top to make an energetically symmetrical device.

Hole only devices were created using a thin layer of poly(3.4-ethylenedioxythiophene)-poly(styrene sulfonate) (PEDOT:PSS). The PEDOT:PSS was left on the surface of the glass for 60 seconds prior to spinning at 3000 rpm for 60 seconds. This layer was then dried in a vacuum oven at 125^{o}C for 1 hour. A PeQD layer was deposit via spin coating at 3000 rpm for 60 seconds. A layer of Spiro-OMeTAD was deposited via spin coating at 3000 rpm for 30 seconds, and then left in

a dry box overnight. A 100 nm layer of gold was then thermally evaporated on the surface to complete the hole only device.

LEDs were fabricated on glass slides with patterned ITO. A layer of PEDOT:PSS was deposited in the same method as the hole only device. A layer of PVK dissolved in DMF (3mg/mL) was spun at 3000 rpm for 60 seconds. A layer of PeQD was deposited at 5000 rpm for 60 seconds. A 5 nm layer of calcium and a 100 nm layer of aluminum were thermally evaporated to complete the LED.

7.3 Results and Discussion

7.3.1 Additive Selection

Four polymers were selected for this study: poly(methyl methacrylate) (PMMA), 2-(4-biphenylyl)-5-phenyl-1,3,4-oxadiazole (PBD), poly(9-vinylcarbazole) (PVK), and bathocuproine (BCP). Additionally, 4 oxides were also used: silicon dioxide (SiO_2), molybdenum trioxide (MoO_3), zinc oxide (ZnO), and titanium dioxide (TiO_2). In Table 5.1 the additives are classified as insulators, hole transport, and electron transport based on the bandgap energy of the additive and the alignment with MAPbBr3 shown in Figure 7.1

Table 7.1: Classification of additives

Insulators	Hole transport	Electron Transport
SiO_2	PVK	BCP
PMMA	MoO_3	TiO_2
PBD		ZnO

.

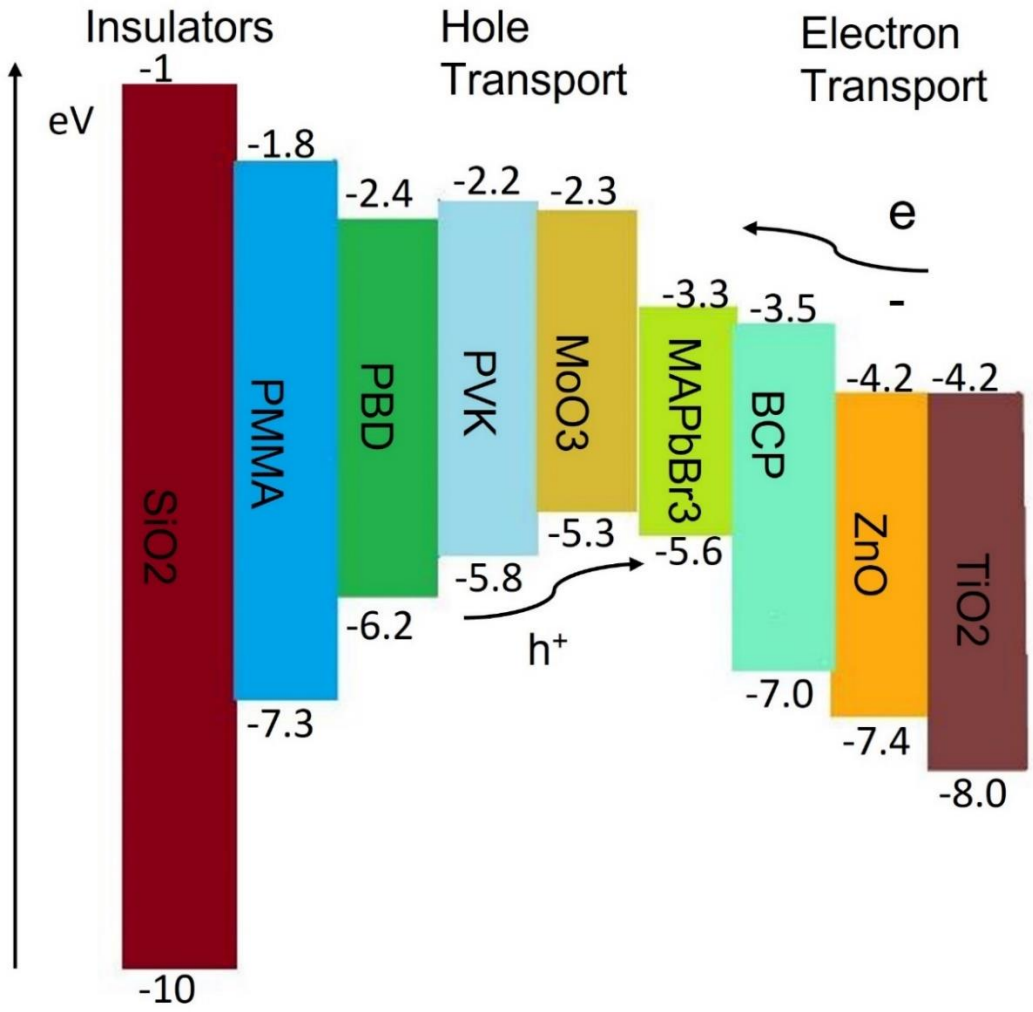

Figure 7.1: Bandgap energies of the additives compared to $MAPbBr_3$ QDs

7.3.2 Optical Characterization

UV-Vis absorption spectroscopy was performed on films spun on neat glass, and the results are shown in Figure 7.2 and Figure 7.3. The absorbance does not show a typical sharp absorption edge characteristic of perovskite bulk films which is likely

caused by a spread in sizes of the quantum dots. There is some reflectance scattering present, specifically on TiO_2 and PBD samples. Tauc plots were used to calculate the

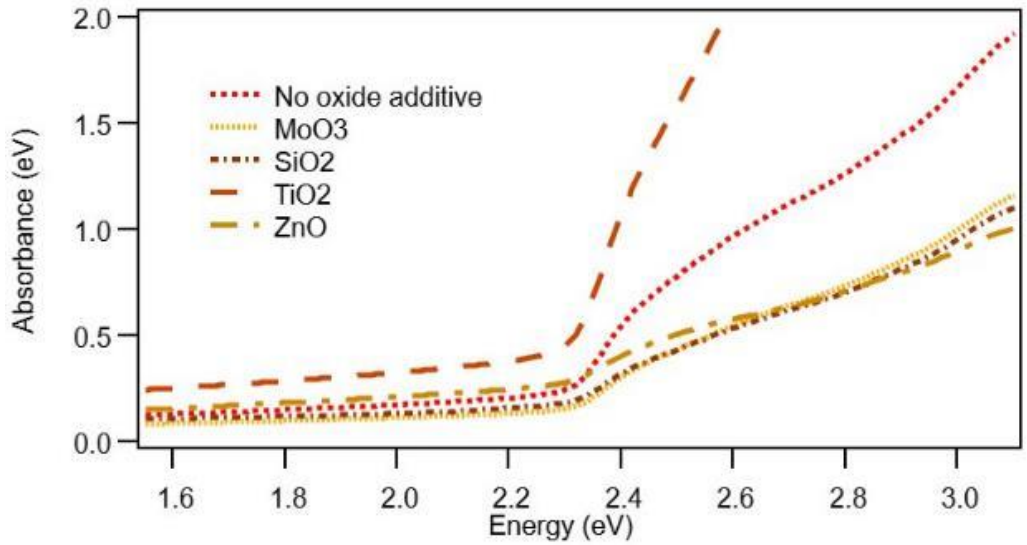

Figure 7.2: Absorbance of Oxide additives

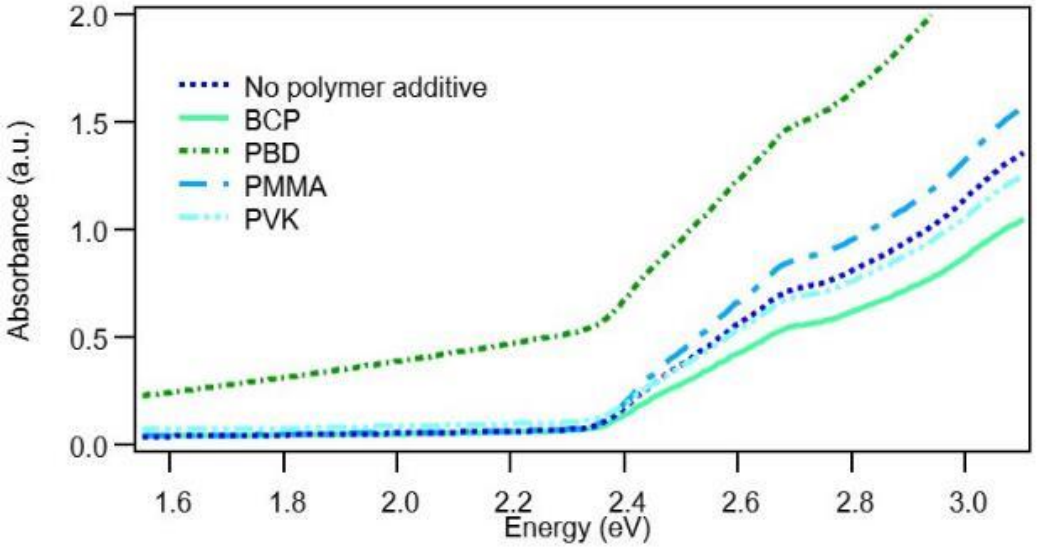

Figure 7.3: Absorbance of Polymer additives

bandgap energy of the films. These results are shown in Table 7.2. The bandgap energies for the oxide additives ranges from 2.25 eV to 2.34 eV, and the bandgap energies for the polymer additives ranges from 2.38 eV to 2.42 eV. Since the oxides and polymers were added to separate batches of the quantum dots, the shift in bandgap between the oxides and polymers is caused by inconsistencies with the LARP method. The bandgaps between no oxide additive and the oxide additives were consistent with an outlier for ZnO at 2.25eV. This outlier could be caused by scattering reflectance, which can introduce errors into the Tauc fit, or a difference in film thickness compared to the other films. The no polymer additive and the polymer additives were consistent for all films. In general, the additive did not have a large effect on the bandgap of the material.

PL was also measured on films spun on neat glass. The results are shown in Figure 7.2

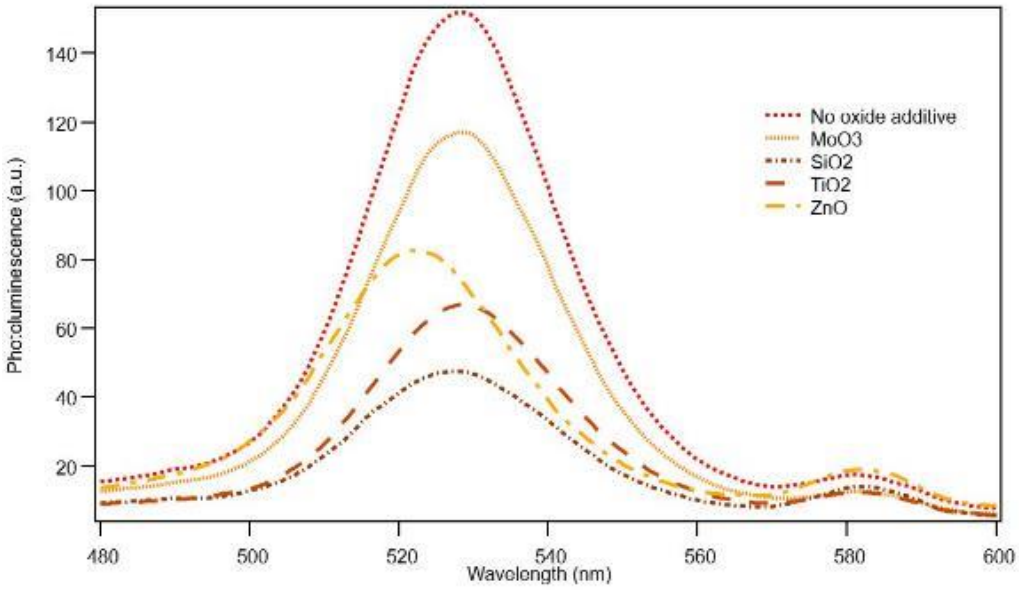

Figure 7.4: PL of oxide additives

Figure 7.4, Figure 7.5, and Table 7.2. The oxide additive did not show an increase in the PL intensities compared to the no oxide additive film. The peak PL for the oxides ranges from 522 nm for ZnO to 529 nm for TiO_2. Apart from ZnO, the peak PL was consistent around 528 nm. The ZnO peak at 522 nm could be caused by film thickness, the ZnO film was measured to be the thinnest of the oxide films and this could account for the shift in PL[8].

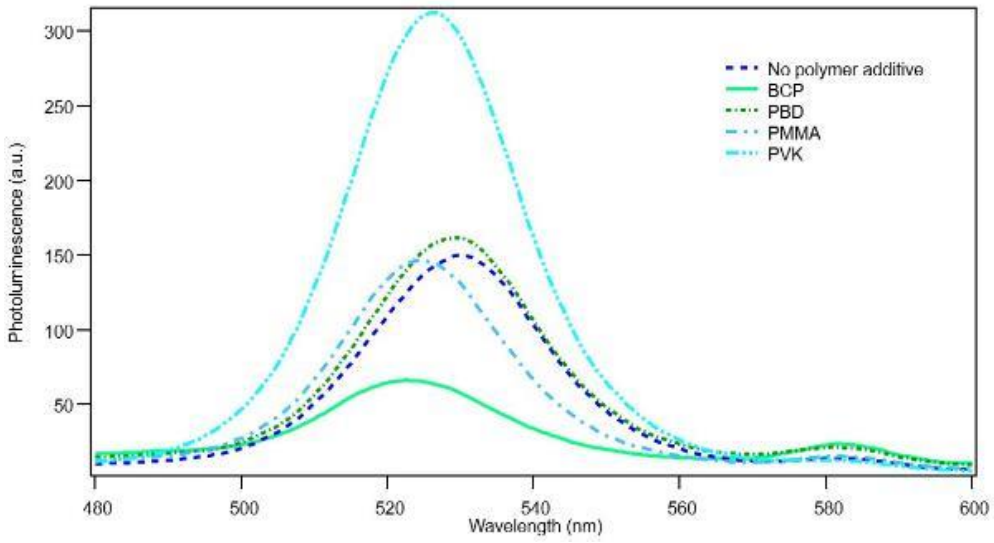

Figure 7.5: PL of polymer additives

The polymer additives did show some effects to the PL when compared to the no polymer additive film. The PVK sample shows increased PL intensity, while BCP shows a decrease in PL intensity. PMMA and PBD have PL intensities similar to the no oxide additive. The PL peak for the polymer additives ranged from 523 nm for BCP to 530 nm for no polymer additive. The full width half maximum (FWHM) for

all films, both oxide additives and polymer additives, were under 20 nm, ranging from 17.1 nm to 19.5 nm. This demonstrates the high color purity of the quantum dots and the additives do not affect the color purity.

Table 7.2: Optical properties of additive films

Sample	FWHM (nm)	PL Peak (nm)	Bandgap (eV)
No Oxide Additive	18.8 +/- 0.1	528	2.33 +/- 0.04
MoO_3	18.7 +/- 1	528	2.34 +/- 0.06
SiO_2	19.5 +/- 0.2	527	2.33 +/- 0/05
TiO_2	18.9 +/- 0.1	529	2.33 +/- 0.03
ZnO	19.1 +/- 0.2	522	2.25 +/- 0.01
No Polymer Additive	18.1 +/- 0.1	530	2.41 +/- 0.12
BCP	18.4 +/- 0.2	523	2.41 +/- 0.12
PBD	17.6 +/- 0.1	529	2.38 +/- 0.08
PMMA	17.1 +/- 0.1	524	2.40 +/- 0.12
PVK	17.7 +/- 0.1	526	2.42 +/- 0.12

7.3.3 Film Characterization

Atomic force microscopy was used on films spun on neat glass. Figure 7.6, Figure 7.7, and Table 7.3 show the results of 30 µm by 30 µm scans. Oxides do not disperse readily in toluene, but instead make a colloidal dispersion much more easily in polar solvents such as DMF. Unfortunately, polar solvents will dissolve the perovskite quantum dots, so the oxides did not readily mix with the quantum dot solutions. This was expected to increase the surface roughness of the films due to particles dispersed on the surface. While these particles were present, the quantum dot film with no additives also had particle present, which could be caused by clumping of the quantum dots. The root mean squared (RMS) surface roughness of the films for the oxide additives ranged from 52 nm for MoO_3 to 86.2 nm to for ZnO. Interestingly,

the film with no oxide additives had an RMS surface roughness of 62 nm, and this shows that roughness was less affected by the addition of oxides to the quantum dot solution.

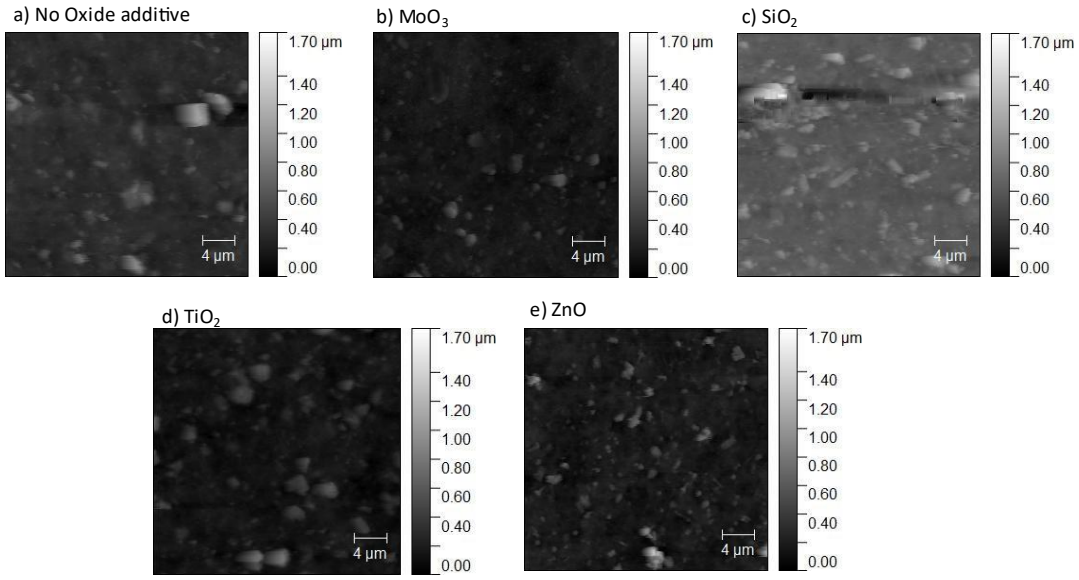

Figure 7.6: AFM of oxide additives. a) No oxide additive, b) MoO_3, c) SiO_2, d) TiO_2, e) ZnO. Scale bar 4µm

The polymer additives were more easily dissolved in toluene and were expected to decrease the surface roughness by creating a composite film of quantum dots and polymers. Figure 7.7 shows that while the original quantum dot batch used for the polymers had better surface roughness, so the polymers did not improve the surface roughness. PBD and PVK, specifically, have interesting surface features which could be caused by lack of dissolution of the polymers in the quantum dot solution. The films could possibly be improved upon by increasing the amount of

toluene in the solution, but this would reduce the concentration of the quantum dot solution which may lead to issues with pin holes and shorts when used in an electrical device.

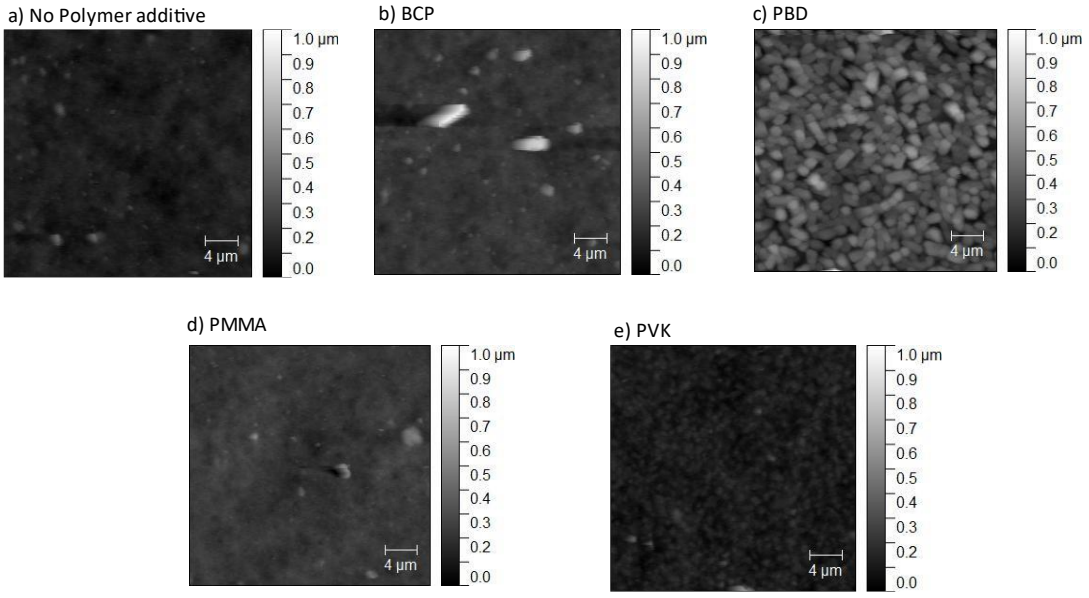

Figure 7.7: AFM of polymer additives. a) No polymer additive, b) BCP, c) PBD, d) PMMA, e) PVK. Scale bar 4µm.

The RMS roughness from Table 7.3 of the polymer additives were lower than the oxide additives, ranging from 29 nm for the no polymer additive film to 91 for PBD. PBD had the largest surface roughness, which is caused by the rod like surface features present. Overall, the additives did not have a positive or negative affect on the surface roughness, and the surface roughness would be improved by filtering the quantum dot solution more effectively prior to mixing in additives or additional changes to the concentration between quantum dots and additives.

Table 7.3: Surface Roughness from AFM for all additives

Sample	Roughness (RMS) (nm)
No oxide additive	62 +/- 30
MoO_3	52 +/- 15
SiO_2	73 +/- 20
TiO_2	75 +/- 28
ZnO	86 +/- 46
No polymer additive	29 +/- 8
BCP	32 +/- 16
PBD	91 +/- 12
PMMA	32 +/- 11
PVK	33 +/- 8

Another method used to verify the consistency of the films was scanning electron microscopy (SEM) on films spun on ITO coated glass slides. Table 7.4 shows the average values of the film thickness. All films were spun using the same conditions, but the oxide additives had a thinning effect on the overall thickness, which the polymer additives had less of an overall effect with PVK showing a large increase, which could be caused by lack of dissolution of the PVK in the quantum dot solution. The standard deviation of the averages shows that the films all had large inconsistencies, but except for PVK, the standard deviation of the film thickness was improved by including the different additives. One of the intended purposes of including the additives into the quantum dot solution was to improve film quality by creating a composite of the additive and the quantum dot solution. This hypothesis was proved incorrect for these films, but it is possible that different weight

percentages of additives and/or changes to the concentration of the solution could enhance the film surface and consistency.

Table 7.4: Film thickness from SEM for all additives

Sample	Thickness (nm)
No oxide additive	1263.7 +/- 403.6
MoO_3	672.8 +/- 309.2
SiO_2	564.7 +/- 202.4
TiO_2	526.2 +/- 133.2
ZnO	407.8 +/- 77.5
No polymer additive	842.2 +/- 416.1
BCP	744.1 +/- 134.9
PBD	676.5 +/- 110.6
PMMA	727.1 +/- 366.4
PVK	1293.7 +/- 669.9

7.3.4 Electrical Characterization

Three types of devices were made to verify the electrical properties of the quantum dot additive films. Single carrier devices were made to compare the hole and electron conduction within the films to explore if the band alignment of the additives would influence the electrical conduction of the films. Figure 7.8 and Figure 7.9 shown the energy band structure for the hole only and electron only devices.

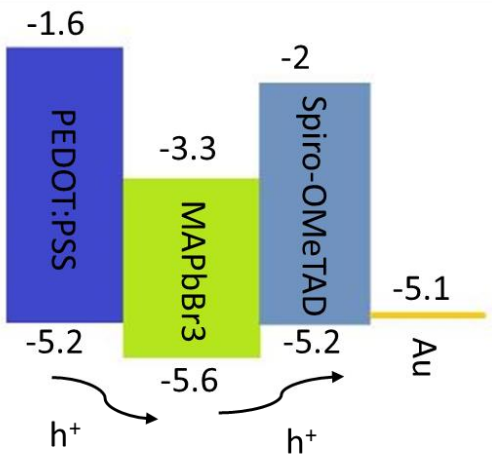

Figure 7.8: Hole only device energy structure

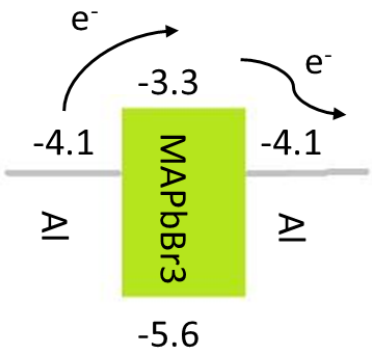

Figure 7.9: Electron only device energy structure

The single carrier devices were measured using a source meter and the current density as a function of voltage was measured. These measurements were taken in the dark, so there would be no carriers generated from photon absorption. Table 7.5 shows the average current density of 6 devices at 8 V. The oxide additive devices showed slight increases in the hole only current density, with the no oxide additive hole only current density at 0.0014 A/cm^2 and the oxides either were the same current

Table 7.5: Current density for single carrier devices for all additives

Sample	Hole only Current Density (A/cm^2)	Electron only Current Density (A/cm^2)
No oxide additive	0.0014	0.0007
MoO_3 (HTL)	0.0056	0.2173
SiO_2 (Insulator)	0.0147	0.0107
TiO_2 (ETL)	0.0013	0.0029
ZnO (ETL)	0.0659	N/A
No polymer additive	0.2754	0.0022
BCP (ETL)	0.0053	0.0013
PBD (Insulator)	0.0272	0.0019
PMMA (Insulator)	0.0910	0.0052
PVK (HTL)	0.0074	0.0006

density as TiO_2 or increased for MoO_3, SiO_2, and ZnO. The comparison between the hole only and electron only current density was inconsistent between the oxide films.

The no oxide additive film showed a decrease in current density from hole only to electron only, but MoO_3 and TiO_2 showed increases in electron only current density compared to hole only. SiO_2 was consistent between the two carriers. ZnO did not have functional electron only devices, so they were not compared. The polymer additives showed higher hole only current density for all films when compared to the electron only current density. The device fabricated with the no polymer additive film had the highest hole only current density, while PMMA had the highest electron only current density. Interestingly, the insulators for both the oxides and polymers showed increased current density for both carrier types when compared to the ETL and HTL additives.

LEDs were fabricated for each additive using the energy structure shown in Figure 7.10. The LEDs were testing using a source meter to test the current density as a function of voltage and the radiance was measured using a spectrometer in absolute irradiance mode and a fiber optic cable. Figure 7.11, Figure 7.12, and Table 7.6 show the results for the champion device out of 6 for each additive. The turn-on voltage for all devices was around 3 V, so the additive does not affect the turn-on voltage for the device. For both oxides and polymers, the devices made without additives had the best external quantum efficiency (EQE). PVK did have a comparable EQE to the no polymer additive LED, but this device had very low current and with lower light output. This could be caused by the increased thickness of the PVK films compared to the other films.

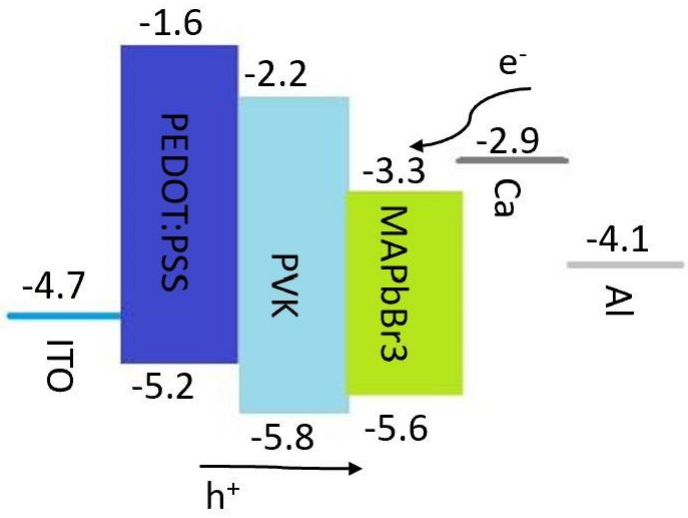

Figure 7.10: LED energy structure

The oxides did not feature any enhancement to the LEDs with EQEs ranging from 0.01% to 0.10% for films with additives. This could be caused by the poor dispersion of oxides in the quantum dot solutions, and increased roughness leading to interface trap states between the layers. The polymers, excluding PVK, also did not feature any enhancement to the LEDs with EQEs ranging from 0.06% to 0.90% for films with additives. These devices were more consistent with the no polymer additive devices when compared to the oxide devices. This could be caused by the reduced surface roughness of the polymer films compared to the oxide films.

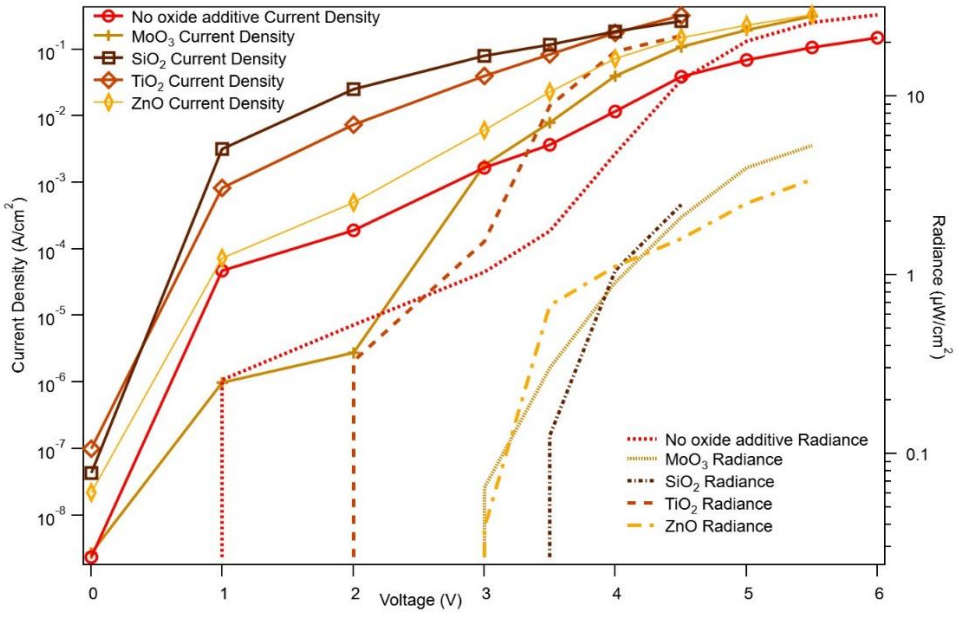

Figure 7.11: LED Current density, radiance as a function of voltage for oxide additives

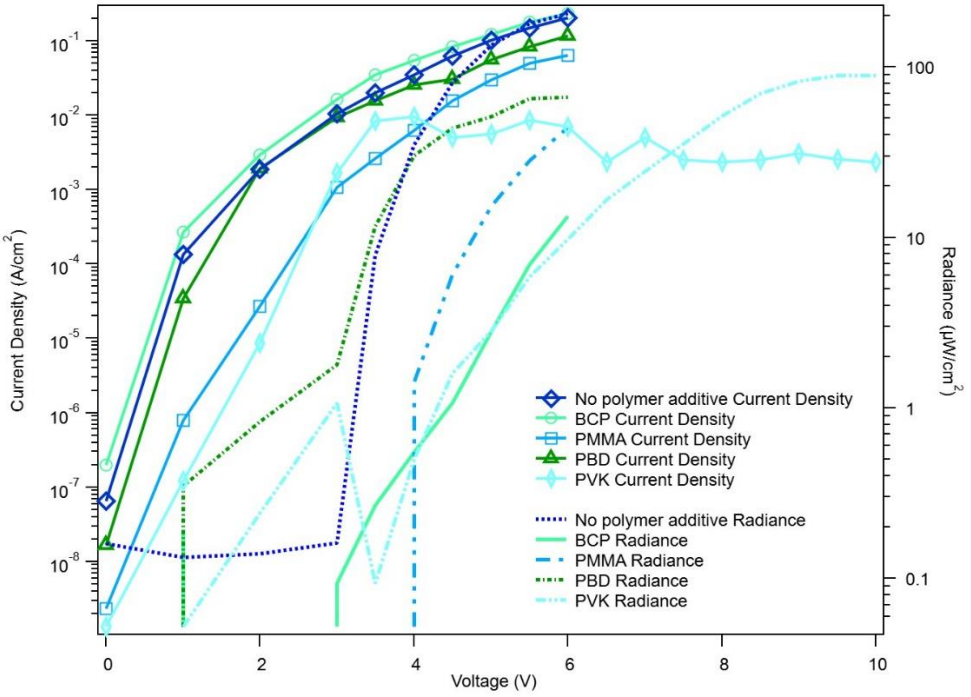

Figure 7.12: LED Current density, radiance as a function of voltage for polymer additives

Table 7.6: External quantum efficiencies and turn on voltages for all additives

Samples	EQE (%)	Turn-on voltage (V)
No oxide additive	0.23%	3
MoO_3	0.02%	3
SiO_2	0.01%	3.5
TiO_2	0.10%	3
ZnO	0.01%	3
No polymer additive	1.31%	3
BCP	0.06%	3
PBD	0.90%	3
PMMA	0.68%	4
PVK	1.39%	3.5

7.4 Conclusions

The original purpose of this work was to improve the film quality of the quantum dots by creating a more consistent film. An additional hope was that the

energy band alignment would help increase carrier conduction through the quantum dot films to enhance device characteristics. The additives did not influence the PL or bandgap of the films. Unfortunately, the oxide additives are not suitable for dispersion in nonpolar solvents such as toluene and left the surface rough with oxide particles. The polymers did not worsen the surface roughness, but there was not improvement to the surface roughness either. It is possible the polymers may have improved the surface roughness if the amount of solvent was increased, as some of the films appeared to not have fully dissolved polymers. The oxides additives did see an enhancement in current density when using single carriers, but the polymer additive did not enhance the current density in either carrier. LEDs fabricated with the additives did not perform as well as the no additive devices for both polymers and oxides. It is possible that changing the concentration of the additives could influence the performance, but the lack of enhancement of the devices is most likely caused by the poor film consistency. The energy alignment did not seem to influence the electrical properties, but there did seem to be some improvement to current density when an insulator was used. This could be due to reducing the likelihood of shorts in the film.

7.5 References

[1] Vickers ET, Enlow EE, Delmas WG, DiBenedetto AC, Chowdhury AH, Bahrami B, et al. Enhancing Charge Carrier Delocalization in Perovskite Quantum Dot Solids with Energetically Aligned Conjugated Capping Ligands. ACS Energy Lett 2020;5:817–25.

[2] Carter S, Scott C, Brock P. Enhanced luminance in polymer composite light-emitting diodes. Applied Physics Letters 1997;71:1145–7. https://doi.org/10.1063/1.119848.

[3] Xin Y, Zhao H, Zhang J. Highly Stable and Luminescent Perovskite–Polymer Composites from a Convenient and Universal Strategy. ACS Appl Mater Interfaces 2018;10:4971–80. https://doi.org/10.1021/acsami.7b16442.

[4] Li G, Tan Z-K, Di D, Lai ML, Jiang L, Lim JH-W, et al. Efficient Light-Emitting Diodes Based on Nanocrystalline Perovskite in a Dielectric Polymer Matrix. Nano Lett 2015;15:2640–4. https://doi.org/10.1021/acs.nanolett.5b00235.

[5] Ling Y, Tian Y, Wang X, Wang JC, Knox JM, Perez-Orive F, et al. Enhanced Optical and Electrical Properties of Polymer-Assisted All-Inorganic Perovskites for Light-Emitting Diodes. Advanced Materials 2016;28:8983–9. https://doi.org/10.1002/adma.201602513.

[6] Li J, Bade SGR, Shan X, Yu Z. Single-Layer Light-Emitting Diodes Using Organometal Halide Perovskite/Poly(ethylene oxide) Composite Thin Films. Advanced Materials 2015;27:5196–202. https://doi.org/10.1002/adma.201502490.

[7] Chen P, Xiong Z, Wu X, Shao M, Ma X, Xiong Z, et al. Highly Efficient Perovskite Light-Emitting Diodes Incorporating Full Film Coverage and Bipolar Charge Injection. J Phys Chem Lett 2017;8:1810–8. https://doi.org/10.1021/acs.jpclett.7b00368.

[8] Ghasemi B, Ševčík J, Nádaždy V, Végsö K, Šiffalovič P, Urbánek P, et al. Thickness Dependence of Electronic Structure and Optical Properties of F8BT Thin Films. Polymers 2022;14:641. https://doi.org/10.3390/polym14030641.

Chapter 8 Tunable emission color of methylammonium lead bromide perovskite quantum dots by varying ligand quantity

Perovskite quantum dots (PQD) can be created using a ligand assisted reprecipitation method at room temperature with affordable equipment. These PQDs can exhibit much higher photoluminescence (PL) than bulk perovskite films of the same material. In this study, methylammonium lead bromide (MAPbBr3) quantum dots were created using energetically aligned capping ligands of trans-cinnamic acid (TCA) and 3,3-Diphenylpropylamine (DPPA). The bandgap of the PQDs was adjusted by varying the quantity of ligands added to the solution during the ligand assisted reprecipitation process. Prototype light emitting diodes (LEDs) were created using the PQD thin films.

8.1 Introduction

Perovskite materials have been proven to be effective active layers of various optoelectronic devices, such as solar cells and light emitting diodes (LED)[1-7]. Perovskites exhibit high charge carrier mobilities, low trap densities, and narrow band emissions[4-7]. Perovskite quantum dot (PQD) materials have shown enhanced photoluminescence (PL) and tunable bandgaps[8-11], but an issue with current quantum dot solutions are the insulating capping ligands used in the formation process. Many quantum dot systems use long chain ligands to control the crystallization; these capping ligands limit charge transport of the quantum dot[12-14]. To overcome this issue, ligands that are energetically aligned with the PQD can be selected[15-18]. In this work, $MAPbBr_3$ PQDs were created using ligands previously developed[18]. The

energy levels for the PQDs are assumed to be similar to the energy levels of the bulk (E_{HOMO}=-3.3 eV, E_{LUMO}=-5.6 eV)[19]. The surface of the PQD core was passivated using trans-cinnamic acid (TCA) (E_{HOMO}=-3.0 eV, E_{LUMO}=-6.1 eV)[20] with energy level alignment shown in Figure 8.1.

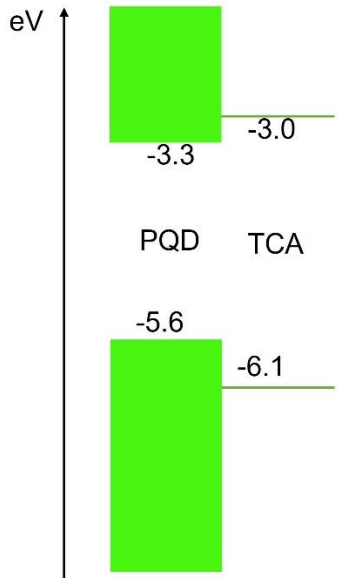

Figure 8.1: Energy band diagram for the PQD core and TCA ligands[19-20].

It has been shown that functionalizing the TCA molecule with electron withdrawing or electron donating groups can change the energy levels and bandgap[21]. For this work, DPPA was used to stabilize the conjugated ions and improve the binding geometry on the PQD surface[18]. $MAPbBr_3$ quantum dots were fabricated with TCA-DPPA ligands using a ligand assisted reprecipitation method. This method involves dissolving the $MAPbBr_3$ precursors in a polar solvent along with the TCA-DPPA ligands. The precursor solution is then injected into an antisolvent. The size, and thus emission, of the PQDs is determined by the quantity of ligands added to the precursor solution. For

this work, the quantity of ligands will be varied to demonstrate the emission tunability of the PQD films.

8.2 Experimental Methods

8.2.1 Quantum Dot Synthesis

Quantum dot solutions were made via a ligand assisted method in ambient conditions. Perovskite precursors, MABr (9 mg) and $PbBr_2$ (73 mg), and TCA (59 mg, 118 mg, or 177 mg for 1x, 2x, and 3x, respectively) were dissolved in 400 µL of DMF. Next, DPPA (35 µL, 70 µL, or 105 µL for 1x, 2x, 3x, respectively) was added to the solution and sonicated for 5 minutes or until the solution was clear. 100 µL of the precursor solution was injected into 5 mL of toluene stirring vigorously. The bright yellow PQD solution was centrifuged at 6000 rpm for 5 minutes. The supernatant was discarded, and the solids were dispersed into 2 mL toluene. Then the PQDs were centrifuged again. This process was repeated until the solids had been washed 3 times. After the final wash, the solids were weighed, and a colloidal dispersion was created using toluene.

8.2.2 Device and Film Fabrication

Films were prepared on clean glass slides by spin coating 30 µL PQD solution at 3000 rpm for 60 seconds. A thin film $MAPbBr_3$ sample was made for comparison to the PQD films. This film was made by dissolving $PbBr_2$ (73mg) and MABr (22mg) in 231 µL DMF and 92 µL DMSO in a nitrogen filled glovebox. Films were prepared on clean glass slides by spin coating 30 µL perovskite solution at 5000 rpm for 30 seconds.

After 6 seconds, an anti-solvent wash of n-butanol was dripped on the spinning slide. Films were annealed for 10 minutes at 80^{o}C.

LEDs were fabricated using indium tin oxide (ITO) patterned glass slides. Titanium oxide (TiO_2) blocking layer was deposited via a doctor blade technique using tape and a squeegee. The TiO_2 films were heated for 5 minutes at 125^{o}C before sintering at 500^{o}C for 30 minutes. PQD films were spun at 3000 rpm for 60 seconds using the same method as the film preparation. Spiro-OMeTAD was spun using 30 µL solution at 3000 rpm for 30 seconds in a nitrogen filled glovebox. Device slides were place in a dry box overnight. 100 nm of gold was deposited using a thermal evaporator.

8.2.3 Measurement and Characterization

The photoluminescence (PL) of neat films on glass slides was measured using Perkin-Elmer LS 45 Luminescence Spectrometer. The excitation wavelength was 393 nm. OD 100 filters were used on the PQD films to ensure the PL peaks were not saturated on the instrument; an OD 30 filter was used on the thin film perovskite sample. Absorbance was measured using Jasco V-670 spectrophotometer from 400 nm to 700 nm wavelength. Electroluminescence (EL) was measured using an Ocean Optics Jaz spectrometer combined with an integrating sphere. Luminance data was taken using a Thor Labs FDS 100-CAL calibrated photodetector, a Keithley 485 pico-ammeter, and an integrating sphere, with the LED mounted on an external port. Current density-voltage measurements were taken simultaneously with the luminance measurements on a Keithley 2400 sourcemeter.

8.3 Results and Discussion

The optical properties of thin film and PQD films on glass were investigated. Figure 8.2a shows the effect of additional ligand on the film PL (green solid line) and absorbance (blue dotted line). Quantum confinement is confirmed when comparing the bulk sample to the PQD samples; there is a distinct blue shift in the absorption band and PL emission peak in the PQD films with increasing ligand quantity. The absorbance for the 1x and 2x ligand PQD films have a broad absorption edge, which is likely caused by diameter differences between the quantum dots in these films. Each film exhibits a small Stokes shift between the absorption band edge and the peak PL. The small Stokes shift implies that the PL emission is due to direct excitonic recombination[22]. **Error! Reference source not found.** shows the bandgap energies found from the absorbance spectra and the Stokes shift for each film. As expected, the bandgap energy increases with increasing ligand quantity.

Table 8.1: Bandgaps and Stokes Shift for each sample.

Sample	Bandgap (eV)	Stokes Shift (nm)
Thin Film	2.3	11
1x	2.3	12
2x	2.4	22
3x	2.7	28

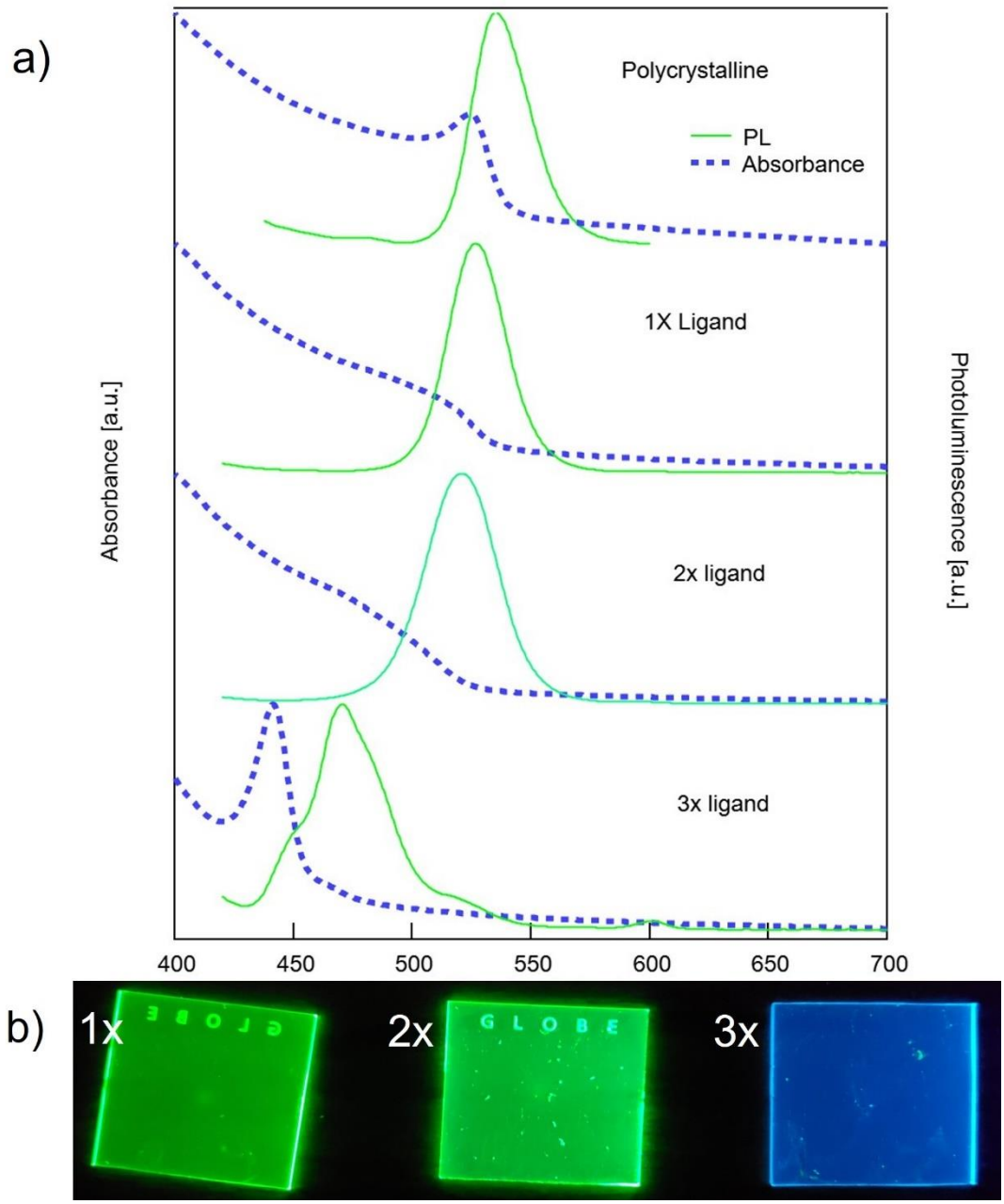

Figure 8.2: a) Normalized PL for thin film perovskite, 1x ligand PQD film, 2x ligand PQD film, and 3x ligand PQD film, b) PQD films under UV illumination, left to right: 3x ligand, 2x ligand, 1x ligand.

Figure 8.2b shows the PQD films under UV illumination, this confirms the additional ligands shift the emission color from green to blue. The films had a trend of decreasing PL peak wavelength with increasing ligand quantity starting from 535 nm for the bulk film, then decreasing to 526 nm for the 1x film, 520 nm for the 2x film, and 470 nm for the 3x film (Figure 8.3). All films had a narrow full width half maximum (FWHM) ranging from 17 nm for the bulk film, 17.6 nm for the 1x film, 21.6 nm for the 2x film, and 25.7 nm for the 3x film.

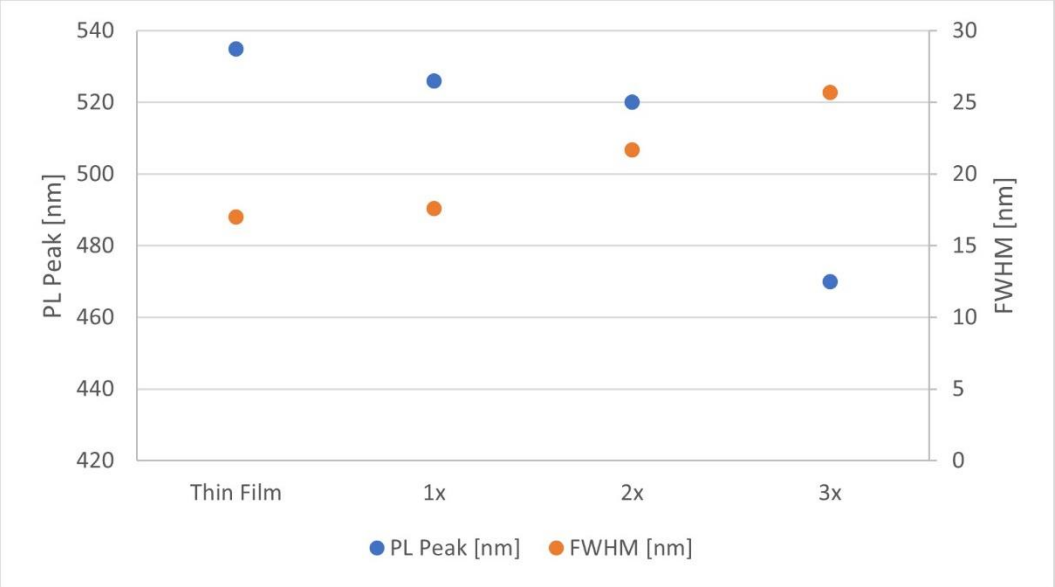

Figure 8.3: PL Peak and FWHM for each film.

LEDs were fabricated with 1x PQD films using the structure shown in Figure 8.4a. Figure 8.4b shows the energy band diagram for the device. A compact TiO2 layer was used as an electron injection and hole blocking layer, and Spiro-OMeTAD was used as a hole injection and electron blocking layer.

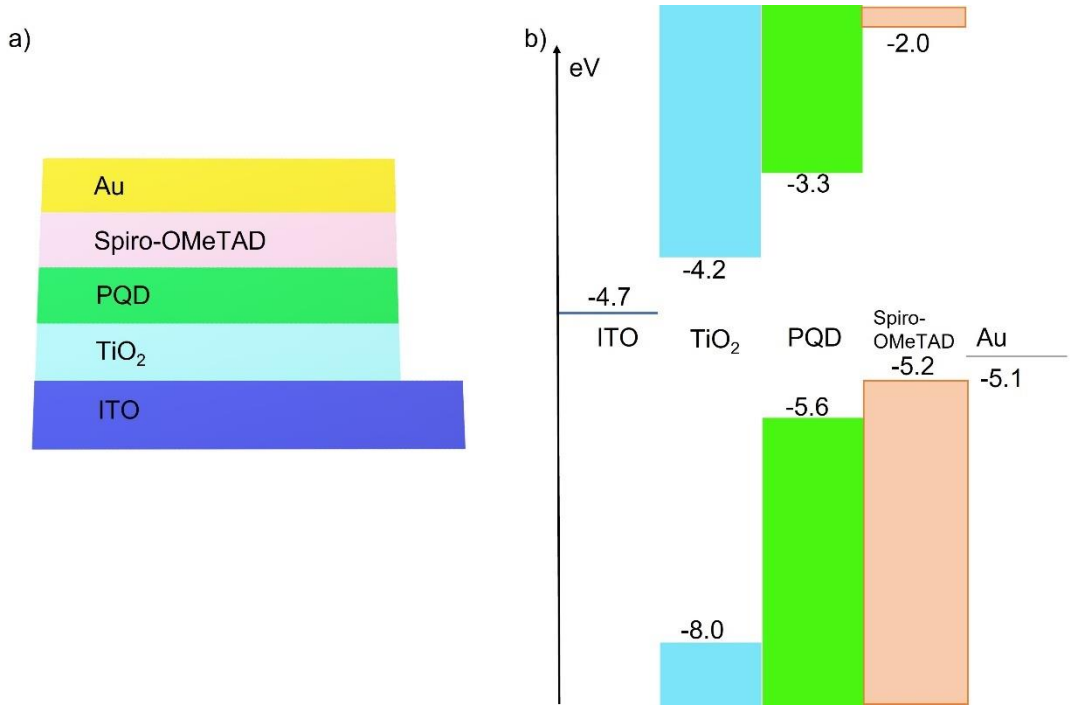

Figure 8.4: a) Device structure, b) Energy diagram of the device[23-24].

The current density (blue dotted line)-luminance (green solid line)-voltage (J-L-V) measurements on a champion device out of 24 tested are shown in Figure 8.5. The device exhibited a low turn on voltage of 2.4V. The inset of Figure 8.5 is the illuminated device. Maximum luminance from the device peaked at 2.6 cd/m^2.

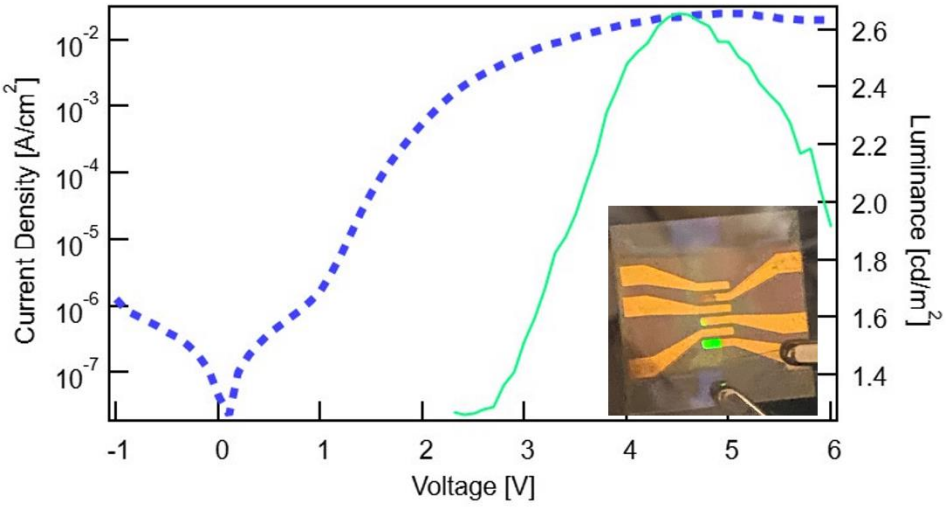

Figure 8.5: Current density (blue dotted line)-Luminance (green solid line)-Voltage of champion device. Inset: Photo of device operating.

The normalized EL of the device with 4.5 V applied is shown in Figure 8.6. The EL peak (green dotted line) is slightly blue shifted from the PL peak (blue solid line) of the film, from 526 nm (PL) to 520 nm (EL). The device exhibited a desirable narrow FWHM of 17 nm.

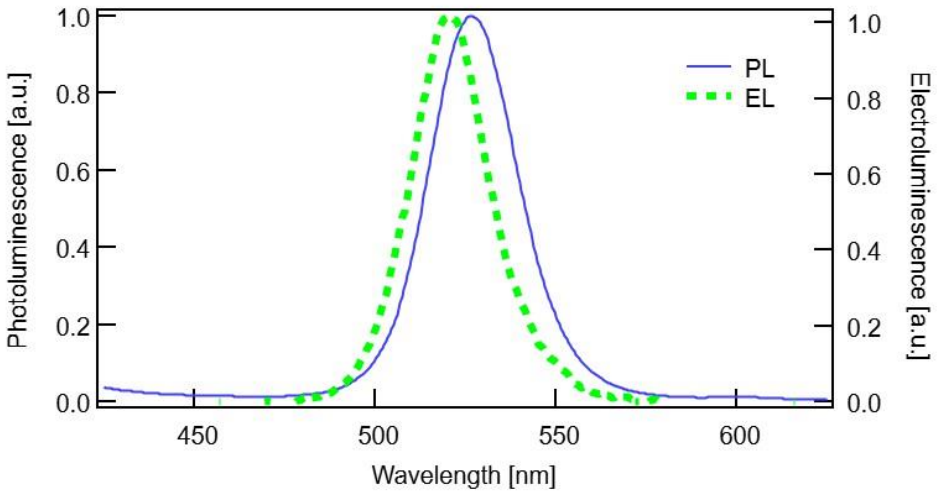

Figure 8.6: Normalized EL of device and normalized PL of 1x ligand PQD film.

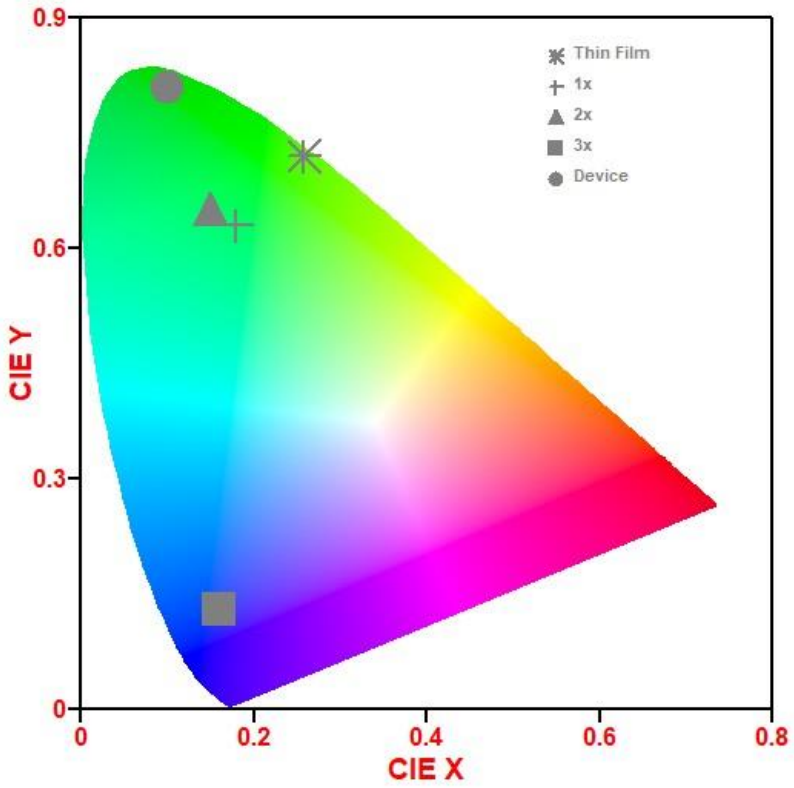

Figure 8.7: CIE plot for thin film and PQD samples and device[25].

The coordinates of the films and device were plotted on the International Commission Internationale de I'Ecairage (CIE) chromaticity diagram in Figure 8.7. All films had color-saturated emission which correlates to the narrow FWHM for each emission. The thin film, 1x, 2x, and 1x device all had emission in the green region while the 3x film had emission in the blue.

8.4 Conclusions

In conclusion, tunable emission was achieved via a ligand assisted reprecipitation method by increasing the ligand quantity in the precursor solution. The

emission wavelength was shifted from 535 nm for the thin film sample to 470 nm for the 3x ligand sample. All samples exhibited a narrow FWHM ranging from 17 nm to 25.7 nm which led to high color purity of each film. Future work on the films will include characterizing the quantum dot films using electron microscopy, to verify the size distribution of the quantum dots. The prototype LEDs required a low turn on voltage of 2.4 V but light emission was limited, peaking at only 2.6 cd/m^2. Improvements to efficiency and light emission could be made by improving the band energy alignment between active layers and electron and hole injection layers. Additionally, work could be done to ensure surface interfaces between the active layer and injection layers have reduced traps and defects. The ligand assisted method for quantum dot fabrication can create quantum dots with a wide range of band gaps while being a low-cost method synthesized in ambient air.

8.5 References

[1] Stranks, S. D., and Snaith, H. J., "Metal-halide perovskites for photovoltaic and light-emitting devices," Nature nanotechnology 10.5, 391-402 (2015).

[2] Tan, Z. K., Moghaddam, R. S., Lai, M .L., Docampo, P., Higler, R., Deschler, F., Price, M., Sadhanala, A., Pazos, L. M., Credgington, D. and Hanusch, F., "Bright light-emitting diodes based on organometal halide perovskite," Nature nanotechnology 9.9, 687-692 (2014).

[3] Chen, H., Wang, H., Wu, J., Wang, F., Zhang, T., Wang, Y., Liu, D., Li, S., Penty, R. V. and White, I. H., "Flexible optoelectronic devices based on metal halide perovskites," Nano Research 13, 1997-2018 (2020).

[4] Fakharuddin, A., Shabbir, U., Qiu, W., Iqbal, T., Sultan, M., Heremans, P. and Schmidt-Mende, L., "Inorganic and layered perovskites for optoelectronic devices," Advanced Materials 31.47, 1807095 (2019).

[5] Quan, L. N., Rand, B. P., Friend, R. H., Mhaisalkar, S. G., Lee, T. W. and Sargent, E. H., "Perovskites for next-generation optical sources," Chemical reviews 119.12, 7444-7477 (2019).

[6] Mitzi, D. B., "Introduction: perovskites," Chemical reviews 119.5, 3033-3035 (2019).

[7] Manser, J. S., Christians, J. A., and Kamat, P. V., "Intriguing optoelectronic properties of metal halide perovskites," Chemical reviews 116.21, 12956-13008 (2016).

[8] Li, Y, Feng, J., and Sun, H., "Perovskite quantum dots for light-emitting devices," Nanoscale 11.41, 19119-19139 (2019).

[9] Yan, D., Shi, T., Zang, Z., Zhou, T., Liu, Z., Zhang, Z., Du, J., Leng, Y. and Tang, X., "Ultrastable CsPbBr3 perovskite quantum dot and their enhanced amplified spontaneous emission by surface ligand modification," Small 15.23, 1901173 (2019).

[10] Wei, Z, and Xing, J., "The rise of perovskite light-emitting diode," The journal of physical chemistry letters 10.11, 3035-3042 (2019).

[11] Song, J., Fang, T., Li, J., Xu, L., Zhang, F., Han, B., Shan, Q. and Zeng, H., "Organic–inorganic hybrid passivation enables perovskite QLEDs with an EQE of 16.48%," Advanced Materials 30.50, 1805409 (2018).

[12] Zhang, F., Zhong, H., Chen, C., Wu, X. G., Hu, X., Huang, H., Han, J., Zou, B. and Dong, Y., "Brightly luminescent and color-tunable colloidal CH3NH3PbX3 (X= Br, I, Cl) quantum dots: potential alternatives for display technology," ACS nano 9.4, 4533-4542 (2015).

[13] Huang, H., Zhao, F., Liu, L., Zhang, F., Wu, X. G., Shi, L., Zou, B., Pei, Q. and Zhong, H., "Emulsion synthesis of size-tunable CH3NH3PbBr3 quantum dots: an alternative route toward efficient light-emitting diodes," ACS applied materials & interfaces 7.51, 28128-28133 (2015).

[14] Huang, H., Susha, A. S., Kershaw, S. V., Hung, T. F. and Rogach, A. L., "Control of emission color of high quantum yield CH3NH3PbBr3 perovskite quantum dots by precipitation temperature," Advanced science 2.9, 1500194 (2015).

[15] Hines, D. A., and Kamat, P. V., "Quantum dot surface chemistry: ligand effects and electron transfer reactions," The Journal of Physical Chemistry C 117.27, 14418-14426 (2013).

[16] Dai, J., Xi, J., Li, L., Zhao, J., Shi, Y., Zhang, W., Ran, C., Jiao, B., Hou, X., Duan, X. and Wu, Z., "Charge transport between coupling colloidal perovskite quantum dots assisted by functional conjugated ligands," Angewandte Chemie International Edition 57.20, 5754-5758 (2018).

[17] Vickers, E. T., Graham, T. A., Chowdhury, A. H., Bahrami, B., Dreskin, B. W., Lindley, S., Naghadeh, S. B., Qiao, Q. and Zhang, J. Z., "Improving charge carrier delocalization in perovskite quantum dots by surface passivation with conductive aromatic ligands," ACS Energy Letters 3.12, 2931-2939 (2018).

[18] Vickers, E. T., Enlow, E. E., Delmas, W. G., DiBenedetto, A. C., Chowdhury, A. H., Bahrami, B., Dreskin, B. W., Graham, T. A., Hernandez, I. N., Carter, S. A. and Ghosh, S., "Enhancing charge carrier delocalization in Perovskite quantum dot solids with energetically aligned conjugated capping ligands," ACS Energy Letters 5.3, 817-825 (2020).

[19] Leyden, M. R., Meng, L., Jiang, Y., Ono, L. K., Qiu, L., Juarez-Perez, E. J., Qin, C., Adachi, C. and Qi, Y., " The journal of physical chemistry letters 8.14, 3193-3198 (2017).

[20] Kroupa, D. M., Voros, M., Brawand, N. P., Bronstein, N., McNichols, B. W., Castaneda, C. V., Nozik, A. J., Sellinger, A., Galli, G. and Beard, M. C., "Optical absorbance enhancement in PbS QD/cinnamate ligand complexes," The journal of physical chemistry letters 9.12, 3425-3433 (2018).

[21] Azzaro, M. S., Babin, M. C., Stauffer, S. K., Henkelman, G. and Roberts, S. T., "Can Exciton-Delocalizing Ligands Facilitate Hot Hole Transfer from Semiconductor Nanocrystals?," The Journal of Physical Chemistry C 120.49, 28224-28234 (2016).

[22] Zheng, K., Zhu, Q., Abdellah, M., Messing, M. E., Zhang, W., Generalov, A., Niu, Y., Ribaud, L., Canton, S. E. and Pullerits, T., "Exciton binding energy and the nature of emissive states in organometal halide perovskites," The journal of physical chemistry letters 6.15, 2969-2975 (2015).

[23] Li, S., Cao, Y.L., Li, W. H. and Bo, Z. S., "A brief review of hole transporting materials commonly used in perovskite solar cells," Rare Metals, 1-18 (2021).

[24] Kour, R., Arya, S., Verma, S., Gupta, J., Bandhoria, P., Bharti, V., Datt, R. and Gupta, V., "Potential substitutes for replacement of lead in perovskite solar cells: A review," Global Challenges 3.11, 1900050 (2019).

[25] Thomas, K. R. J., GoCIE, Department of Chemistry, Indian Institute of Technology, (2009).

Chapter 9 Conclusions

Perovskite materials are an interesting study for optoelectronics due to their unique properties. The crystal structure allows for a large tuning of the bandgap. The low formation energy facilitates inexpensive methods of fabrication, while the perovskite crystal structure is generally defect tolerant. This work explored the one-step deposition method with an antisolvent wash to determine the benefits of using different antisolvent washes. The wash that proved to be most effective was n-butanol due to the enhance surfaces.

The ease of synthesis is extended into quantum dot fabrication as well. The method used in this work focused on using organic ligands to stabilize and control the reactions. These ligands can also have a dramatic effect on the electrical and optical properties of the quantum dot films. Two different types of ligands were studied: oleylamine and oleic acid (OLA-OA) and 3,3-diphenylpropylamine and trans-cinnamic acid (DPPA-TCA). The DPPA-TCA ligands were more conductive and offered better surface passivation and photoluminescence when compared to the OLA-OA ligands. Using the DPPA-TCA ligands, different oxides and polymers were added to the quantum dot solution, but ultimately the additives did not have a positive effect on the quantum dot films. Lastly, the quantity of the DPP-TCA ligands was varied during synthesis to show the tunable photoluminescence emission and bandgap. The quantum dots were successfully shifted from green to blue while maintaining the high color purity expected from perovskites.